INDEPENDENT TECHNICAL ASSESSMENT OF THE ORBITER LH_2 FEEDLINE FLOWLINER CRACKING PROBLEM

FINAL REPORT

JULY 20, 2004

TABLE OF CONTENTS

VOLUME I: ITA REPORT

1.0 AUTHORIZATION AND NOTIFICATION 3
2.0 SIGNATURE PAGE (ASSESSMENT TEAM MEMBERS) 4
3.0 TEAM MEMBERS, EX OFFICIO MEMBERS, AND CONSULTANTS 5
4.0 EXECUTIVE SUMMARY 6
5.0 DESCRIPTION OF THE PROBLEM, PROPOSED SOLUTIONS, AND RISK ASSESSMENT 9
6.0 ITA PLAN 17
7.0 RESULTS OF THE ITA TESTS AND ANALYSES 23
8.0 ROOT CAUSES, OBSERVATIONS AND FINDINGS, PROPOSED FLIGHT RATIONALE 101
9.0 CONCLUSIONS AND RECOMMENDATIONS 121
10.0 LESSONS LEARNED 123
11.0 DEFINITION OF TERMS AND ACRONYMS 126

VOLUME II: APPENDICES

A. ITA/I Request Form (NESC-PR-003-FM-01)

B. Original NESC Flowliner ITA Plan

C. Reference Materials
- C.1 LO_2 Type II Engine 1 Feedline Qualification and Test History
- C.2 MPS Flowliner Replication Team Status Report
- C.3 Investigation of Shuttle MPTA LH_2 Flowliner Crack. Huntington Beach/Seal Beach Site Host Engineering Function Material & Process Engineering Laboratory Report; Lab Report No. M&PE-2-1327
- C.4 Original LO_2 Qualification Test Report Summary: Crack Summary. Document Number MPS-QTR-13542-302. Appelman, H., 1979
- C.5 Compilation of the Crack Inspection Data

D. Engineering Reports of Tests and Analyses
- D.1 The Loading Environment (As described By Flow Physics)
- D.2 Development of the Fatigue Loading Spectrum
- D.3 Damage Tolerance (Fracture Mechanics) Analysis Methods and Results
- D.4 Fatigue Life to Crack Initiation Analysis Methods and Results
- D.5 Examination and Inspection Methods
- D.6 Crack Initiation and Surface Enhancement

E. Tasks and Schedule for Phase II

F. Contractors

G. Core Team Bios

Volume I: ITA Report

1.0 AUTHORIZATION AND NOTIFICATION

David Hamilton, NESC Chief Engineer at Johnson Space Center (JSC), presented the risk assessment of the Orbiter liquid hydrogen (LH_2) feedline flowliner cracking problem to the NESC Review Board on January 29, 2004. The authorization to develop an Independent Technical Assessment (ITA) plan was approved by the NESC Review Board (NRB).

The ITA plan was developed by Dr. Charles E. Harris and approved by the NRB on February 19, 2004.

In-briefings of the ITA plan were provided to Helen McConnaughey and John Muratore, Systems Engineering and Integration, on February 26, 2004, at Marshall Space Flight Center and Steve Poulos, Orbiter Project Office, was briefed on March 4, 2004, at Johnson Space Center.

2.0 SIGNATURE PAGE (ASSESSMENT TEAM MEMBERS)

Charles E. Harris, Lead

Clinton Deputy Lead

Gary R. Halford

Peter J. Bonacuse

Ivatury S. Raju

Richard O. Ballard

Kenny B. Elliott

Daniel S. Kaufman

Fred W. Martin, Jr.

Milind A. Bakhle

Cetin C. Kiris

Daniel L. Sutliff

James H. Rogers

Eric I. Madaras

Robert S. Piascik

3.0 TEAM MEMBERS, EX OFFICIO MEMBERS, AND CONSULTANTS

Team Members

Charles E. Harris, NESC/LaRC	Lead, Structural Integrity
Clinton H. Cragg, NESC/LaRC	Deputy Lead, NESC Principal Engineer
Gary R. Halford, GRC	High Cycle Fatigue
Peter J. Bonacuse, GRC	High Cycle Fatigue and Probabilistic Mechanics
Ivatory S. Raju, NESC/LaRC	Structures (Fracture Mechanics)
Richard O. Ballard, MSFC	Propulsion (SSME)
Kenny B. Elliott, LaRC	Structural Dynamics (Experimentalist)
Daniel S. Kaufman, GSFC	Structural Dynamics (Analysis)
Fred W. Martin, Jr., JSC	Computational and Experimental Fluid Dynamics
Cetin C. Kiris, ARC	Unsteady Turbopump Flow Physics
Daniel L. Sutliff, GRC	Duct Acoustics Specialist
Milind A. Bakhle, GRC	Fluid/Structure Interaction Specialist
Eric I. Madaras, LaRC	Nondestructive Evaluation (NDE)
James H. Rogers, MSFC	S&MA and Probabilistic Risk Assessment
Robert S. Piascik, NESC/LaRC	Materials Discipline Expert

Ex-Officio Member

William F. Lane, JSC	Liaison to Orbiter Program Office

Consultants

George D. Hopson, NESC/MSFC	Propulsion
Julie Kramer-White, NESC/JSC	Mechanical analysis
Steven Labbe, NESC/JSC	Flight Sciences
Dochan Kwak, ARC	Computational Fluid Dynamics

4.0 EXECUTIVE SUMMARY

In May of 2002, three cracks were found in the downstream flowliner at the gimbal joint in the LH_2 feedline at the interface with the Low Pressure Fuel Turbopump (LPFP) of Space Shuttle Main Engine (SSME) #1 of orbiter OV-104. Subsequent inspections of the feedline flowliners in the other orbiters revealed the existence of 8 additional cracks. No cracks were found in the LO_2 feedline flowliners. A solution to the cracking problem was developed and implemented on all orbiters. The solution included weld repair of all detectable cracks and the polishing of all slot edges to remove manufacturing discrepancies that could initiate new cracks. Using the results of a fracture mechanics analysis with a scatter factor of 4 on the predicted fatigue life, the orbiters were cleared for return to flight with a one-flight rationale requiring inspections after each flight. OV-104 flew mission STS-112 and OV-105 flew mission STS-113. The post-flight inspections did not find any cracks in the repaired flowliners.

Even though the flowliner repair solution appeared to be successful, the NASA and contractor engineering team continued to investigate the problem. This continuing investigation was motivated by the fact that the actual cause of the original cracks had not been conclusively established. As part of the continuing investigation, two engine hot fire test series were conducted at Stennis Space Center to characterize the LH_2 feedline flow physics and to measure the flowliner vibratory response. The test results were somewhat alarming because the vibratory strains recorded by strain gages mounted directly to the upstream and downstream flowliners were considerably higher than anticipated. The strain gage data were used conservatively to develop a loading spectrum to represent the "worst-case" nominal flight. An updated damage tolerance analysis of the flowliner was then conducted by the Boeing Company based on the inspection crack detection limit of 0.075 inches adopted in 2002. The predicted values of residual fatigue life were only 0.8 missions for a circumferential crack in the upstream flowliner and 1.4 flights for the downstream flowliner. These new results cast doubt on the validity of the flight rationale developed in 2002. Subsequently, the Orbiter Program Office sponsored an extensive effort to resolve this problem.

At the request of the Orbiter Program, the NESC conducted an assessment of the Orbiter LH_2 Feedline Flowliner cracking problem with a team of subject matter experts from throughout NASA. The first objective of the assessment was to characterize the flowliner cracking problem, identify constraints, establish the problem resolution space, and develop a problem resolution strategy. After this objective was achieved, the NESC independently conducted a number of computational analyses and laboratory tests. The NESC developed fatigue loading spectra for nominal flight conditions, refined fracture mechanics analysis methods, and a high fidelity inspection method for in-situ examination of the flowliner slots. The NESC also assessed available materials data to characterize the fatigue life and crack propagation behavior of Inconel 718 in liquid hydrogen. Using these data and methods, the NESC conducted fatigue life and damage tolerance analyses to estimate the residual fatigue lives of the upstream and downstream

flowliners for nominal flight conditions. The results of these analyses were used to establish a strategy for developing a flight rationale for the certification conditions specified by the Program.

Five General Findings have been concluded from the independent tests and analyses conducted by the NESC. It is essential to note that these Findings are only applicable to the nominal flight condition. The development of the flight rationale must be based on a complete assessment of the program-sanctioned loading spectra for all nominal and off-nominal flight conditions for which the orbiter must be certified before returning to flight. The General Findings are:

1. Based on the past flight history and the root causes investigation, the actions taken in 2002 to repair the LH_2 gimbal joint flowliners render the Orbiter safe to fly. This is provided the flowliners are inspected before the next flight to ensure that all surface flaws were removed by polishing and all fatigue cracks were repaired. In addition, an assessment of the certification loading spectra for the nominal and off-nominal flight conditions will be necessary to determine the post-flight inspection requirements.

2. Based on a probabilistic risk assessment, the risk of SSME damage due to cracks in the flowliner is an insignificant contributor to the overall SSME catastrophic risk, assuming inspection after every flight.

3. The similitude between the BTA/GTA ground tests environment and the Orbiter flight environment could not be established. Therefore, there are uncertainties in the fatigue loading spectra developed from the BTA/GTA test data. Unverified scale factors have been applied to the loads in the fatigue loading spectra in an attempt to account for these uncertainties. Because of these uncertainties, there will be risks associated with any loading spectrum used to develop the flight rationale derived from the BTA/GTA experiment. These concerns notwithstanding, we have concluded that the ground test data can be a suitable database to establish the certification spectra provided conservative scale factors based on appropriate engineering judgment are used to account for the uncertainties.

4. Based on the NESC loading spectra for nominal flight conditions generated from the BTA/GTA test data, the conservative NESC ITA damage tolerance analysis for the circumferential crack locations requires inspection after every flight to detect a critical crack size of 0.020 inches and repair of any cracks found during the inspection. Since these results were not generated for the official certification spectra, post-flight inspection requirements must be determined from an assessment of the certification loading spectra for the nominal and off-nominal flight conditions.

5. Based on the NESC loading spectra for nominal flight conditions generated from the BTA/GTA test data, the conservative NESC ITA fatigue life analysis shows a positive margin of safety for one flight, but is not sufficient to cover the remaining anticipated operational life of each orbiter.

Based on the five General Findings stated above, the NESC ITA has concluded that the Orbiters are safe to return to flight provided the specific recommendations listed below are implemented:

1. Establish the surface quality of the slots by using a high fidelity inspection method such as edge replication. Assess the effectiveness of the original polishing done in 2002 to determine if all manufacturing defects have been removed. Re-polish the slots as required to remove all significant surface defects. Also, repair any fatigue cracks found during this inspection.

2. Perform a damage tolerance analysis for all certification conditions to establish the critical crack size, the required inspection method to detect the critical crack size, and the required inspection interval.

3. Conduct a POD study and develop the inspection procedure that must be used to meet the requirements of the damage tolerance analysis.

4. Change the orbiter operational procedures to implement the inspection requirements established by Recommendation 2.

5. Perform a fatigue analysis for all certification conditions to estimate the fatigue life to crack initiation. This establishes the safe life limit on the flowliners. These results may be used in lieu of the damage tolerance approach (Recommendation 2) provided the results satisfy the requirements of NASA Standard 5001 and the NASA Fracture Control Board grants a waiver of the NASA Standard 5007.

Finally, the ITA Team would like to commend the Program Team and their supporting contractors on their outstanding efforts to resolve this complex problem. In addition, many of these individuals spent a significant amount of their time assisting the ITA Team in understanding this multifaceted issue.

5.0 DESCRIPTION OF THE PROBLEM, PROPOSED SOLUTIONS, AND RISK ASSESSMENT

In May of 2002, three cracks were found in the downstream flowliner at the gimbal joint in the LH_2 feedline in OV-104. The gimbal joint was at the interface with the LPFP to the SSME #1 (see Figure 5.0-1). Subsequent inspections of the feedline flowliners in the other orbiters revealed a total of 11 cracks in the fleet. The cracks extended from the drainage slots and were oriented in the axial or circumferential direction with respect to the flowliner shell (See Figure 5.0-2). Each orbiter had at least two cracks. Cracks were located in either the upstream or downstream flowliner of the LH_2 feedlines to engine #1 or engine #2. No cracks were found in the LH_2 feedline to engine #3. Also, no cracks were found in the LO_2 feedline flowliners. In addition, one circumferential crack was found in the Main Propulsion Test Article (MPTA).

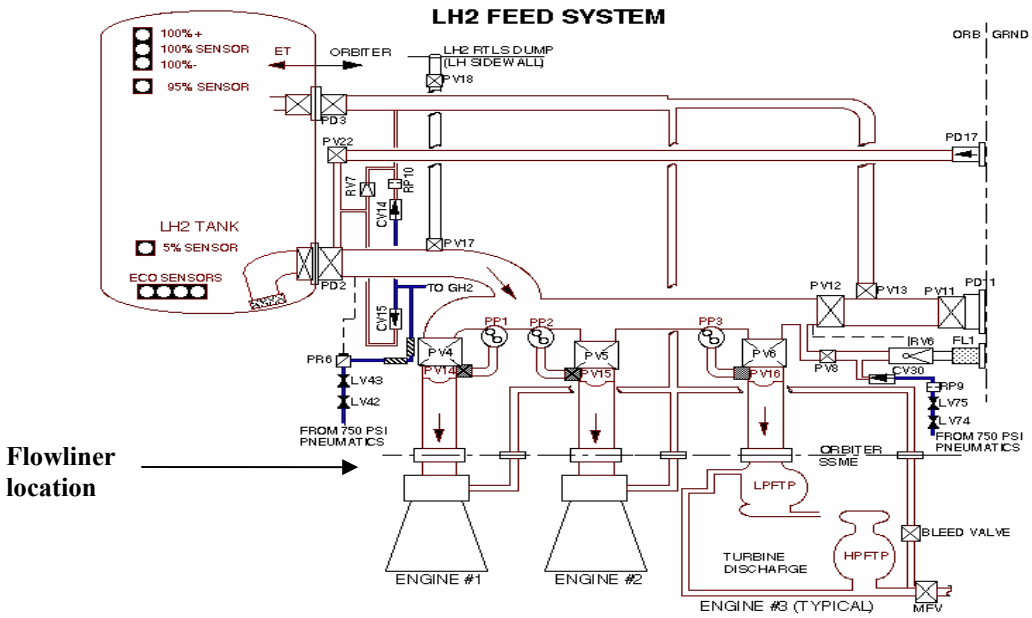

Figure 5.0-1. Schematic of the LH_2 Feed System portion of the Main Propulsion System (MPS)

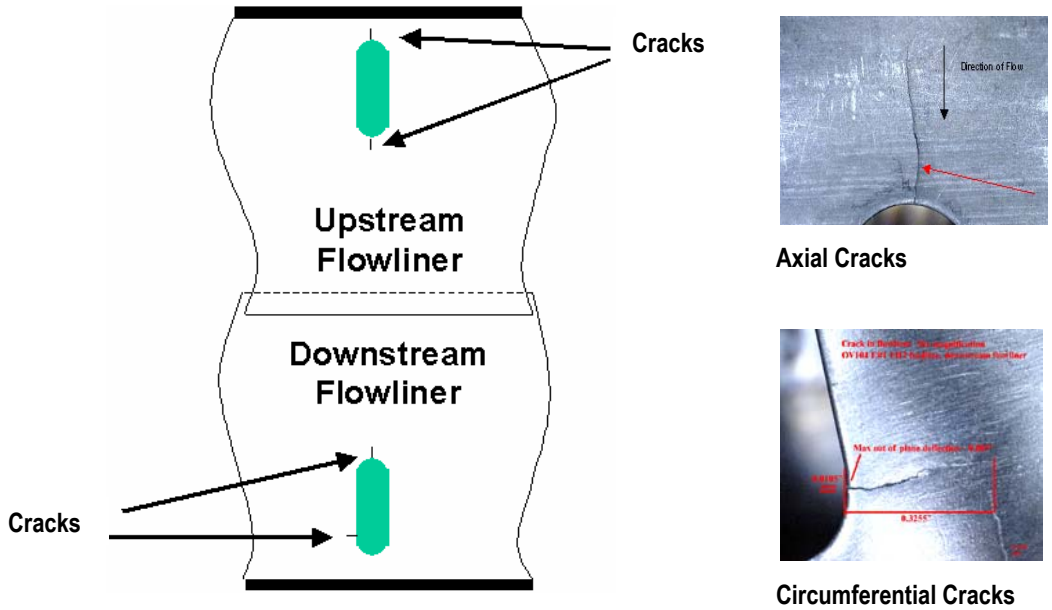

Figure 5.0-2. Crack Locations and Orientation

Over the course of the summer of 2002, a variety of methods were used to examine the Orbiter cracks. These methods included visual, mold impressions, eddy current, ultrasonic, photographic, x-ray, and acetate tape (though not all cracks were examined with all techniques). While most of these examinations included a measurement of crack length, no consolidation of results was ever published. This led to inconsistencies between the results. For example, OV-102's three cracks have variously been reported as only partially across the ligament between slots and also as slot-to-slot 'through cracks'. In another example, the crack at slot 17 on OV-105 had a range of reported crack lengths between 0.186 and 0.6 inches. As all of the cracks have subsequently been repaired, further analysis of the cracks was impossible.

Table 5.0-1 provides a summary of all the Orbiter cracks. Circumferential cracks emanated from the straight side of the slot and grew towards an adjacent slot. Axial cracks initiated from the rounded portions of the slots and grew, at least initially, towards either the free end or the assembly weld of the flowliner. OV-102's flowliners, made of CRES 312, had 76 slots with a 0.25 inch ligament length between slots. All other Orbiters' flowliners were made of Inconel 718 and had 38 slots with a 0.75 inch ligament length between slots. Reported crack lengths varied from 0.1 to 0.6 inches.

Table 5.0-1

Orbiter Crack Summary

Vehicle	Material	No. Of Flights	Total Cracks	Circumferential Cracks	Axial Cracks
OV-102	CRES 321	28	3	3	0
OV-103	INCONEL 718	30	3	0	3
OV-104	INCONEL 718	26	3	2	1
OV-105	INCONEL 718	19	2	0	2

After reviewing all available fleet crack data, some observations can be made:

a. All circumferential cracks were located in the downstream flowliner on the assembly weld side of the slot (OV-102, OV-104).

b. Only one axial crack grew towards an assembly weld (upstream flowliner, OV-103).

c. All other axial cracks (5) grew towards the free edge of the flowliner (OV-103, OV-104, and OV-105).

d. Some axial cracks exhibited a significant kink in their growth. The most pronounced was OV-105's axial crack at slot 17 on the downstream flowliner (see Figures 5.0-3 and 5.04). This crack was also the longest reported, 0.6 inches (as measured along its entire length).

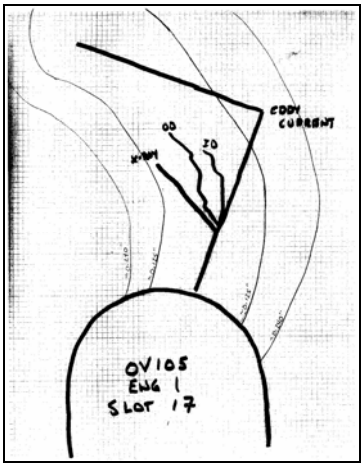

Figure 5.0-3
Sketch of Axial Crack in OV-105

Figure 5.0-4
Photograph of Axial Crack in OV-105

e. Some cracks exhibited bifurcation (see Figure 5.0-5).

Figure 5.0-5. Crack Bifuricaton

f. Some cracks exhibited branching (see Figure 5.0-6).

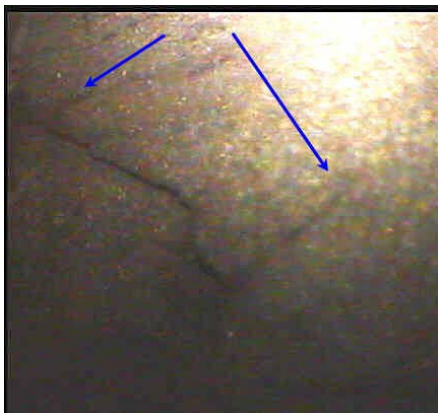

Figure 5.0-6. Crack Branching

g. No axial crack reached the free edge or the assembly weld of the flowliners.

h. No circumferential crack in the Inconel flowliners reached an adjacent slot. The longest reported circumferential crack in Inconel flowliners was 0.47" (ligament length 0.75 in.).

i. While it is expected that the crack lengths on the inside and outside diameter of the flowliner would be different, reported results do not differentiate between the two.

A compilation of the crack inspection data, provided by the Orbiter Program Office, is located in Appendix C-5.

The functions of the gimbal joint flowliner are to 1) maintain smooth LH_2 flow through the bellows area and into the LPFP and 2) to protect the bellows against flow induced vibration. The flowliner is welded to the flange of the feedline gimbal (Figures 5.0-7 and 5.0-8) and BSTRA joints. The flowliner is a thin shell structure about 12" in diameter and 0.050" in thickness. The

upstream flowliner is about 3.50” long and the downstream flowliner is 2.88” long. The shell is perforated with numerous elongated slots about 1.0” by 0.25” (Figure 5.0-9). The purpose of the slots is to allow access during manufacturing for clean-up and to release the propellant trapped between the flowliner and the bellows. The flight critical issues related to the flowliner are disruption of the flow field leading to the LPFP cavitation, loss of flowliner structural integrity, and metallic foreign object debris (FOD) ingestion by the SSME.

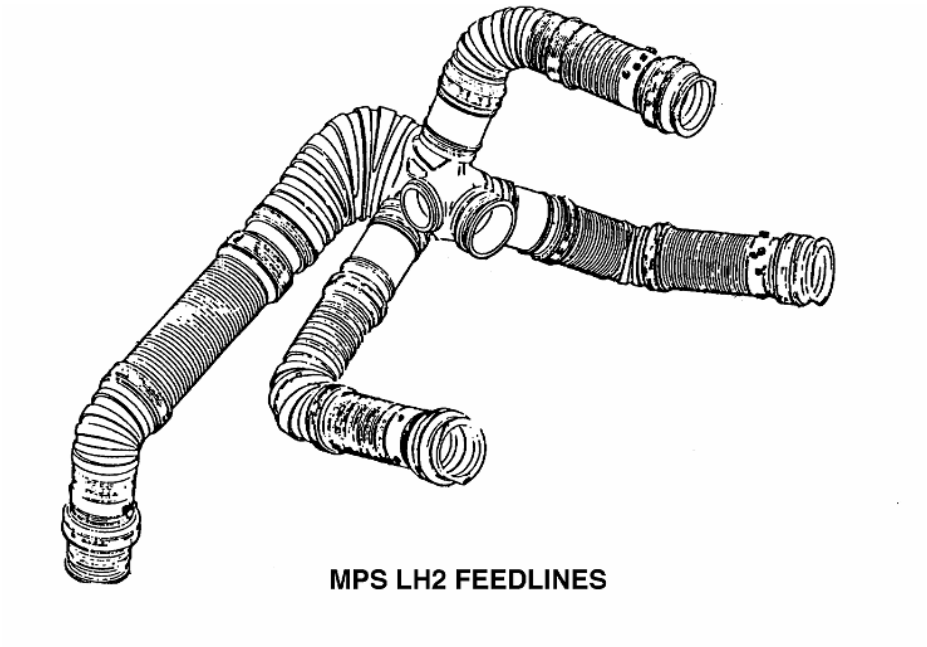

Figure 5.0-7. MPS LH_2 Feedlines Configuration

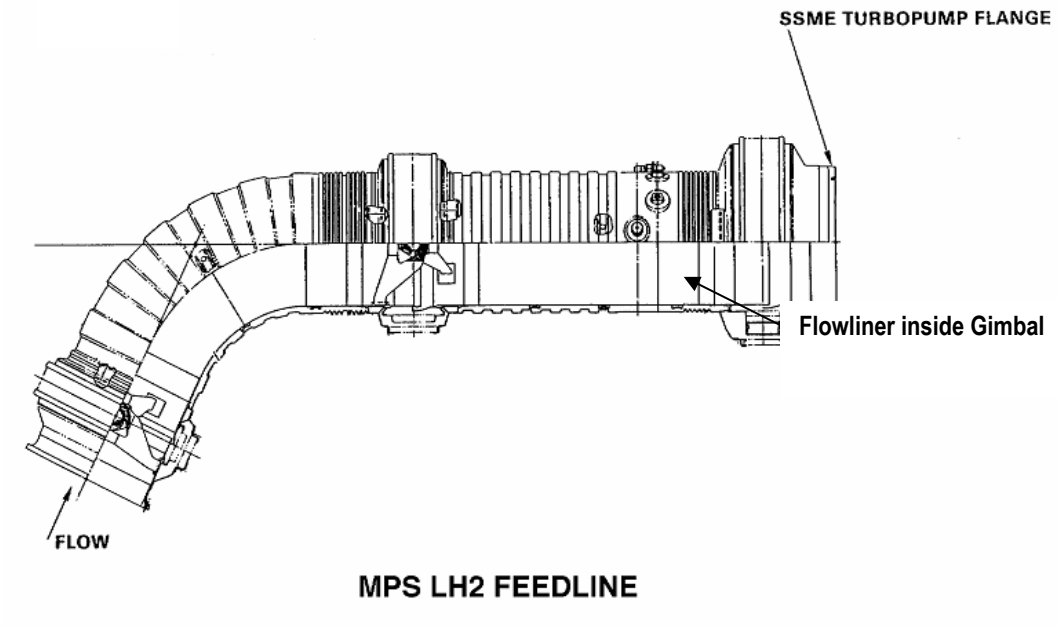

Figure 5.0-8. Typical MPS LH_2 Feedline

Working throughout the Summer and Fall of 2002, a NASA/Contractor problem resolution team developed a solution to the crack problem and cleared the flowliners for one mission. The solution included weld repair of all detectable cracks and the polishing of all slot edges (to remove manufacturing discrepancies that could initiate a new crack). The flight rationale was based on a damage tolerance analysis of the flowliner for both the 'with' and 'without' weld repaired configurations. The damage tolerance analysis used fracture mechanics to predict the service life of the flowliner assuming a detectable crack of 0.075" and a fatigue scatter factor of 4 on the predicted life. A so called "reverse" analysis was performed wherein the assumptions and approximations in the fracture mechanics analysis were established by fitting the analysis to the actual orbiter flight data for the known cracks. The analysis predicted a service life of 8-12 flights. Therefore, this result supported a one-flight rationale with a scatter factor of 4 on the predicted fatigue life. The repair solution was implemented and all orbiters were cleared for return to flight. OV-104 flew mission STS-112 and OV-105 flew mission STS-113. Post flight inspections did not find any cracks.

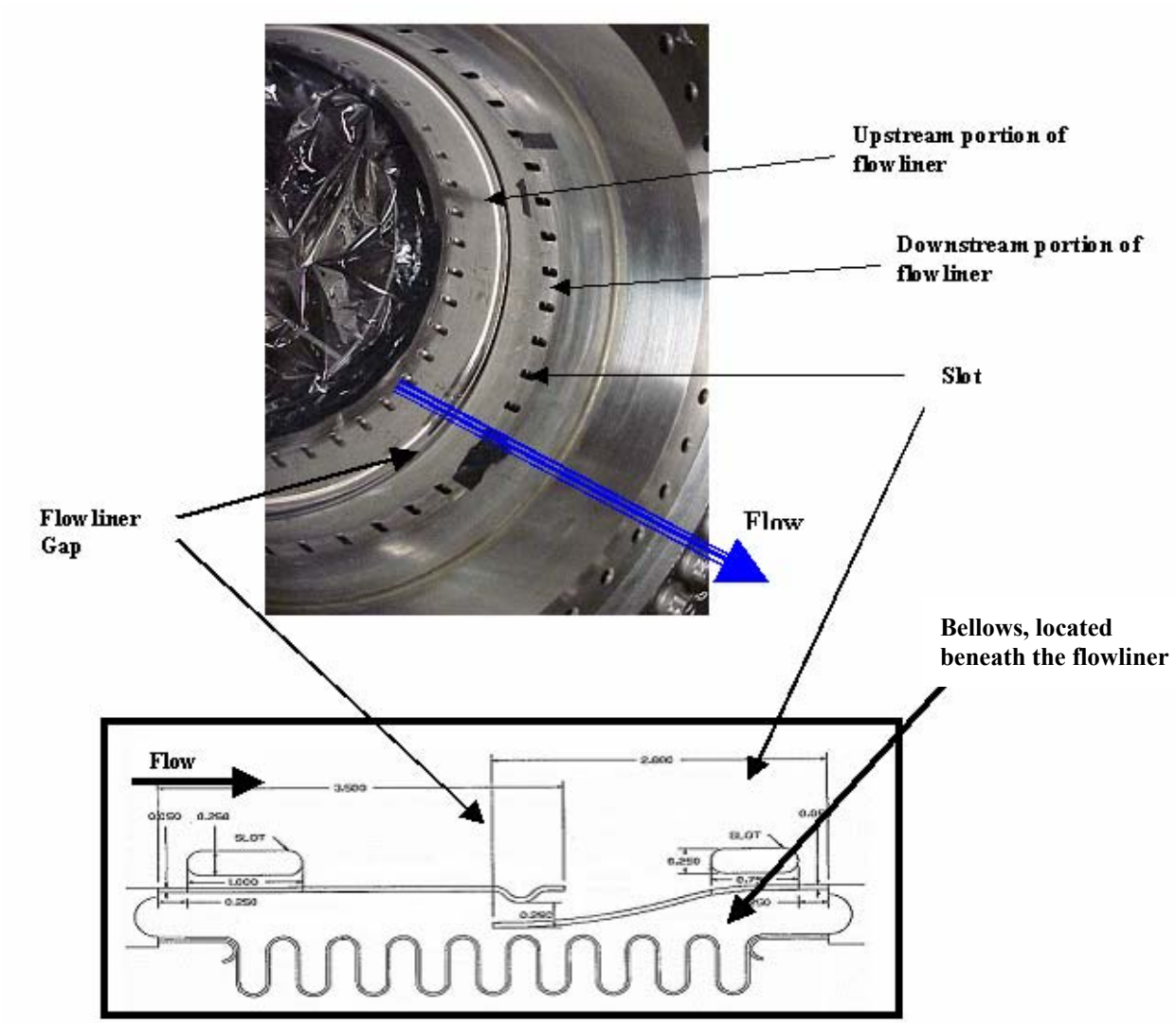

Figure 5.0-9. Photograph and Schematic of Slots in Flowliners

Even though the flowliner repair solution appeared to be successful, the NASA and contractor engineering community continued to investigate the problem. This continuing investigation was motivated by the fact that the actual cause of the original cracks had not been conclusively established. As part of the investigation, two engine hot fire test series were conducted. The purpose of these tests was to better understand the feedline flow physics and the associated forcing functions, which define the spectrum loadings on the flowliner. One test series used a simplified test article with a fixed joint and without a flexible bellow, hereinafter referred to as the battleship test article (BTA) and BTA test. The second test article had a gimbal joint with a

flexible bellows, hereinafter referred to as the gimbal test article (GTA) and GTA test. While the GTA was more like the flight hardware than was the BTA, neither test article exactly matched the orbiter feedline geometry. Also, the test conditions did not fully simulate the actual orbiter flight environment. The vibratory responses of both the upstream and downstream flowliners were measured during each test from strain gages mounted directly to the flowliners. The test results were somewhat alarming because the vibratory strains (peak rms strains of over 300 μstrain) measured on the heavily instrumented flowliners were considerably higher than anticipated. In addition, there were some significant discrepancies between the results of the two tests.

Using the results of the BTA and GTA tests, a new damage tolerance analysis, called a "forward" fracture analysis, was performed by the Boeing Company to predict the residual fatigue life of the flowliners. The strain gage data recorded during the BTA and GTA tests were used conservatively to develop a loading spectrum to represent the "worst-case" nominal flight. Following the standard damage tolerance analysis procedure, the fracture mechanics analysis assumed that a crack of 0.075", defined by the inspection crack detection limit, existed at the critical locations in the flowliner. The predicted values of residual fatigue life were only 0.8 missions for a circumferential crack in the upstream flowliner and 1.4 flights for a circumferential crack in the downstream flowliner. These new results cast doubt on the validity of the flight rationale developed in 2002.

Subsequently, the Orbiter Program Office sponsored an extensive effort to resolve this problem. Proposed solutions being pursued by the Program include developing a new flight rationale for the existing hardware and/or redesigning the flowliners and requalifying the LH_2 feedlines. In addition, there is considerable effort underway to refine the description of the flight environment and develop new loading spectra by conducting additional ground tests and analyses. While the program-sponsored work to resolve the problem is incomplete, the NESC was requested to conduct an independent assessment of the problem and provide recommendations to the Program.

David Hamilton, NESC Chief Engineer at JSC, presented the risk assessment of the flowliner cracking problem to the NESC Review Board on January 29, 2004. The likelihood of occurrence and the consequences were assessed to be a 5x5 risk on the qualitative risk scale ranging from 1 to 5, with 5 being the highest likelihood and most severe consequences. A PRA will be conducted as part of the ITA to quantify the risk of flowliner failure resulting in a SSME failure (see Section 7.8).

6.0 ITA PLAN

The scope of the NESC flowliner ITA is to identify the primary contributors to the cracking in the flowliner and develop a strategy to resolve the problem and/or mitigate risks to acceptable flight levels. The assessment is being conducted in two distinct phases. Phase I assessed the problem and proposed a flight rationale. Tests and analyses will then be conducted in Phase II to establish the validity of the flight rationale. A two-phased approach to the assessment was pursued because the Orbiter Program Office requested that the NESC review their proposed problem resolution plan. It was felt that a timely review by the NESC will validate the plan and/or identify alternate problem resolution paths.

The objectives of Phase I were to fully characterize the flowliner cracking problem, identify constraints and establish the problem resolution space, and independently develop a problem resolution strategy. The Phase I assessment was guided by the flow chart in Figure 6.0-1. This flowchart documents the engineering actions required to determine the residual fatigue life of the flowliner. After a review of the history of the problem, which included an independent analysis of the data from previously conducted tests, the ITA Team developed a problem resolution strategy including a logic framework for a flight rationale. Tests and analyses were also conducted by the ITA Team in Phase I to facilitate the assessment. Several of these tests and analyses will be continued in Phase II. The ITA problem resolution strategy was compared to the problem resolution plans of the Program-sponsored team. The Phase I findings and recommendations will be given to the Orbiter Program Office.

Phase II will focus on independent tests and analyses conducted by the ITA Team to establish the efficacy of alternate problem resolution paths identified in Phase I. The results of these tests and analyses will establish the validity of the flight rationale proposed in Phase I. A PRA will establish the relative risk of the flight rationale for all operational conditions for which the flowliner must be certified. Specific requirements to be implemented by the Orbiter Program to fulfill the flight rationale will be identified at the end of Phase II. To ensure efficiencies where appropriate, the tests and analyses conducted during the NESC ITA will be coordinated with the activities of the team sponsored by the Orbiter Program Office.

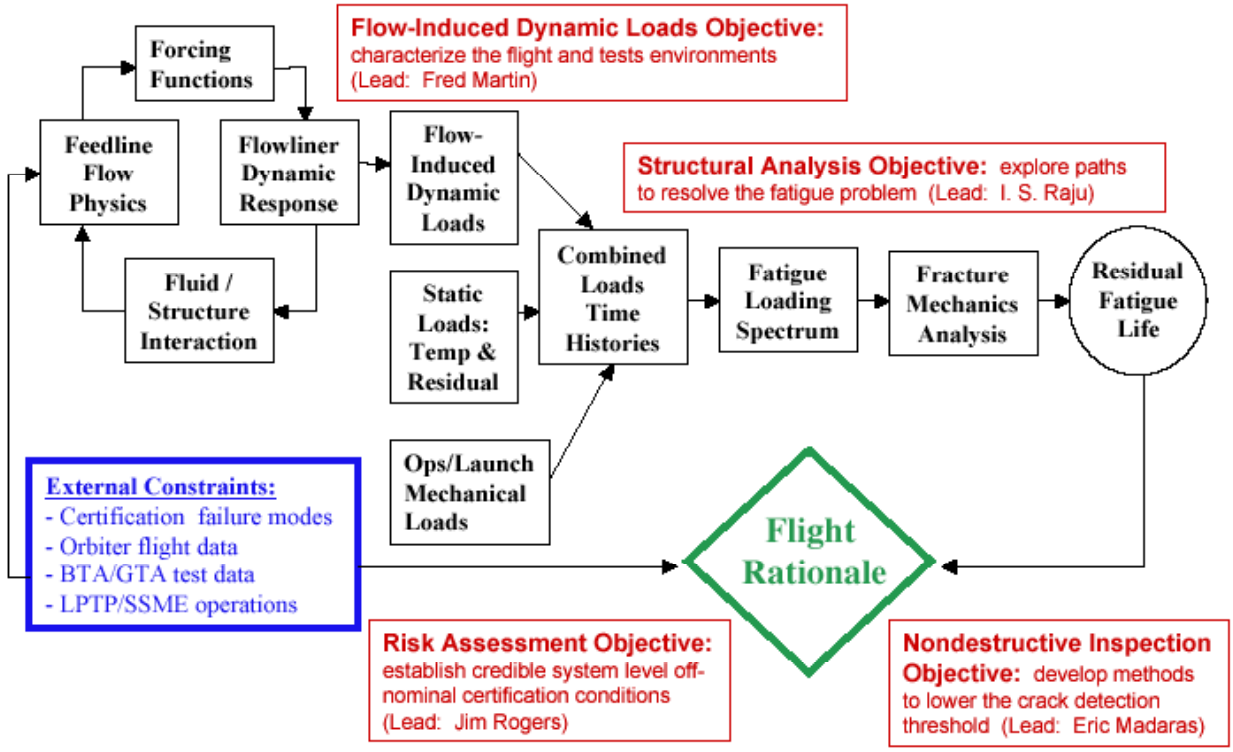

Figure 6.0-1. Phase I Assessment Flowchart

Phase I Plan

Phase I Objective: Fully characterize the flowliner cracking problem, identify constraints and establish the problem resolution space, and independently develop a problem resolution strategy.

Phase I Schedule: February 23, 2004 – July 20, 2004

Key Milestones (date accomplished):

February 19th:	Brief NRB on ITA Plan
Week of March 1st:	In-Briefings to Orbiter and Shuttle Integration Offices
May 28th:	Complete Phase I findings and recommendations
Week of July 12th:	Brief NRB on Phase I findings
Week of July 19th:	Brief Orbiter Program Office (PRCB) on Phase I findings

Phase I Assessment Strategy:

1. Establish a comprehensive characterization of the flowliner cracking problem and understand the actions underway or completed to resolve the problem.

2. Develop a logic flow diagram of the test/analysis method/procedure to determine residual life of the in-situ flowliner, showing the interfaces (input/output) between the disciplines.
3. Compile the list of potential root causes (primary contributors). Evaluate existing data and identify additional tests and analyses required to establish the controlling mechanisms and first order effects.
4. Develop a fracture mechanics analysis tool (model) for both high cycle fatigue and low cycle fatigue to assess the effects of residual stress, loading spectrum, and the crack detection threshold. Initiate deterministic and probabilistic sensitivity analyses to identify the first order effects on fatigue life.
5. Develop a system level risk assessment tool, using the probabilistic risk analysis method as appropriate, and a risk mitigation/management plan.
6. Assess the efficacy of nondestructive methods to measure the as-assembled residual stress field in the test articles and the Orbiter flowliners.
7. Assess the efficacy of improved/refined nondestructive examination methods to reduce the inspection threshold for crack detection below the current threshold of 0.075 inch.
8. Define the data required (tests and analyses requirements) to meet an acceptable flight rationale (e.g. inspect and fly).
9. Using the above results, develop an integrated, comprehensive problem resolution strategy and propose a flight rationale.
10. Compare the ITA strategy (1.9) to the "Orbiter Project Team" plan and identify similar findings, gaps, and alternate resolution paths.
11. Compile the findings and recommendations for the Orbiter Project Office.

Phase I Assessment Tasks:

Structural Analysis

1. Perform a finite element analysis to estimate the residual stresses in the flowliner due to manufacturing and develop a Phase II test plan to measure the residual stresses.
2. Develop deterministic and probabilistic fracture mechanics models and predict the residual fatigue life.
3. Develop a probabilistic fatigue life model and estimate the life to crack initiation.
4. Perform finite element analyses of the flowliner to predict mode shapes and frequencies and to develop loading spectra for the fatigue and fracture analyses.
5. Develop a Phase II test plan to conduct a laboratory test to verify fracture mechanics crack growth models/methods.

6. Evaluate surface enhancement treatments by conducting coupon tests under axial and bending fatigue loadings.

Flow-Induced Dynamic Loads

Using available ground test and flight data and CFD analyses, assess the following questions:

1. How well do the various ground tests (air, water, and hot fire) simulate the flight environment?
2. Do the CFD simulation results provide a realistic measure of the forcing functions for a particular flowliner resonance/excitation?
3. Can the BTA/GTA instrumentation be improved?
4. How significant are the acoustical effects of the feedline manifold and ducts?

Risk Assessment

1. Develop a system level risk assessment tool, using the probabilistic risk analysis method as appropriate and a risk mitigation/management plan.

Nondestructive Inspection

1. Establish the relative accuracy of portable, nondestructive methods to quantitatively measure the residual stresses in the flowliner due to the assembly weld and the crack repair welds.
2. Identify and start to refine a method to inspect the flowliner for cracks that could reduce the threshold for detectable cracks to below the current threshold of 0.075 inch.
3. Develop a method for inspecting the surfaces of the slots in the flowliner to characterize the in-situ surface (hole) quality.

Phase II Plan

Phase II Objectives:

1. Conduct tests and analyses to establish the validity/efficacy of alternate problem resolution paths identified in Phase I and estimate the relative risks levels of the proposed flight rationale.

2. Develop and verify improved nondestructive examination methods (NDE) to measure the in-situ state of the flowliners.

Phase II Schedule: June 1, 2004 – September 30, 2004

See Appendix E for detailed listings of tasks and schedules for Phase II.

Phase II Tasks:

1. Conduct a laboratory test to verify the fracture mechanics methodology for predicting crack growth due to resonant frequencies excited in the flowliner. Residual stresses will also be measured in the test articles.
2. Conduct laboratory tests to independently validate the crack growth rate data for Inconel 718 at -423° F.
3. Complete fatigue tests to verify efficacy of the edge replication method to detect insipient cracks in the flowliner.
4. Participate in a study to establish the POD data to support the implementation of a high fidelity inspection method. POD data must be generated for the edge replication method and the best conventional, automated nondestructive evaluation (NDE) method.
5. Complete the study to establish the efficacy of the low plasticity burnishing (LPB) method as a viable surface enhancement treatment to significantly extend the fatigue life of the flowliners.
6. Using the models and methods developed in Phase I, complete the deterministic and probabilistic fracture mechanics and fatigue life analyses of the flowliner and update the PRA of the flowliner/SSME failure modes of the Orbiter propulsion system for all certification cases necessary to support the flight rationale.
7. The NESC will use the certification loading spectra developed by the Program. However, alternate approaches to the transfer ratio approximation will be developed and used in the analyses described in number 6 above.
8. Several CFD analyses will be conducted to better understand the effects of various feedline components on the LH_2 flow at 104.5 percent RPL. These components include the feedline's 64 degree elbow, the BSTRA joint, the flowliner's bellows cavity, and the LPFP inducer.
9. Steady State CFD analysis will be conducted to compare flight vehicle feedline flow with that of the E1 test stand arrangement.
10. Wind tunnel testing will be conducted on two-dimensional models of the flowliner to establish slot edge tone excitation character (i.e., frequency and amplitude characteristics).

11. Acoustic tests on a three-dimensional model of the flowliner assembly will be conducted to document bellows cavity resonance frequencies and mode shapes. Acoustic testing will also be conducted on the three dimensional feedline models to ascertain the characteristics of the feedline.
12. Scaled water flow tests on three-dimensional feedline models will be accomplished to measure the feedline velocity profile with a laser velocimeter. (These data will provide essential input to the CFD analysis described in numbers 9 and 10).
13. Complete probabilistic risk assessment of the flowliner failure using updated input data from other Phase II tasks.

7.0 RESULTS OF THE ITA TESTS AND ANALYSES

In this chapter, the results from the tests and analyses conducted by the NESC Flowliner ITA Team during the assessment will be presented and discussed. The specific tests and analyses conducted by the team were previously listed in Chapter 6. Chapter 7 contains only a brief description of each test or analysis along with the key results that lead directly to the observations and findings documented in Chapter 8. A thorough description of the test and/or analysis methods and the complete results, including sensitivity studies, are located in the Engineering Reports provided in Appendix D of Volume II of this report.

The loading environment is discussed in the first section of this chapter and is followed by the development of the fatigue loading spectra. The next two sections present the cumulative damage results predicted by the fracture mechanics analysis and the fatigue life analysis using the fatigue loading spectra described in Section 2. Section 5 describes the edge replication method, a high fidelity nontraditional inspection method, and section 6 discusses conventional, automated inspection methods. The concluding section describes the system level PRA conducted to determine the impact of a flowliner failure on the risk of a SSME failure. Provided below is the cross-reference between the sections of Chapter 7 and the appendices containing the detailed engineering reports:

7.1 The Loading Environment (as described by flow physics) **(Appendix D.1)**

7.2 Development of the Fatigue Loading Spectrum **(Appendix D.2)**

7.3 Damage Tolerance (Fracture Mechanics) Analysis Methods and Results, Part I, **(Appendix D.3)**

7.4 Damage Tolerance (Fracture Mechanics) Analysis Methods and Results, Part II, **(Appendix D.3)**

7.5 Fatigue Life To Crack Initiation Analysis Methods and Results **(Appendix D.4)**

7.6 Edge Replication Examination Method **(Appendix D.5)**

7.7 Nondestructive Evaluation Methods for In-service Inspection **(Appendix D.6)**

7.8 Probabilistic Risk Assessment (completely documented in **Section 7.8**)

7.1 The Loading Environment (As Described By Flow Physics)

The transfer of LH_2, from the External Tank (ET) to the SSMEs is accomplished through a vacuum jacket insulated duct system that includes numerous internal components and three small radius turns before reaching the inlet to the SSME's low pressure fuel pump (LPFP). Also, the fuel lines must be able to contract and rotate as the temperature changes when the fuel is loaded. The flexibility is provided at several ball strut tie rod assembly (BSTRA) joints and at the gimbal joint which is located at the down stream end of the feedline and is attached to the inlet of the LPFP.

Typical conditions of the fuel for a 104.5 percent power level are a mass flow rate of 154.7 lbm/s at a temperature of 37°R. The temperature increases slightly, during ascent, as the heat load to the ET warms the LH_2, which rises to the top of the hydrogen tank. Figure 7.1-1. shows a typical temperature profile.

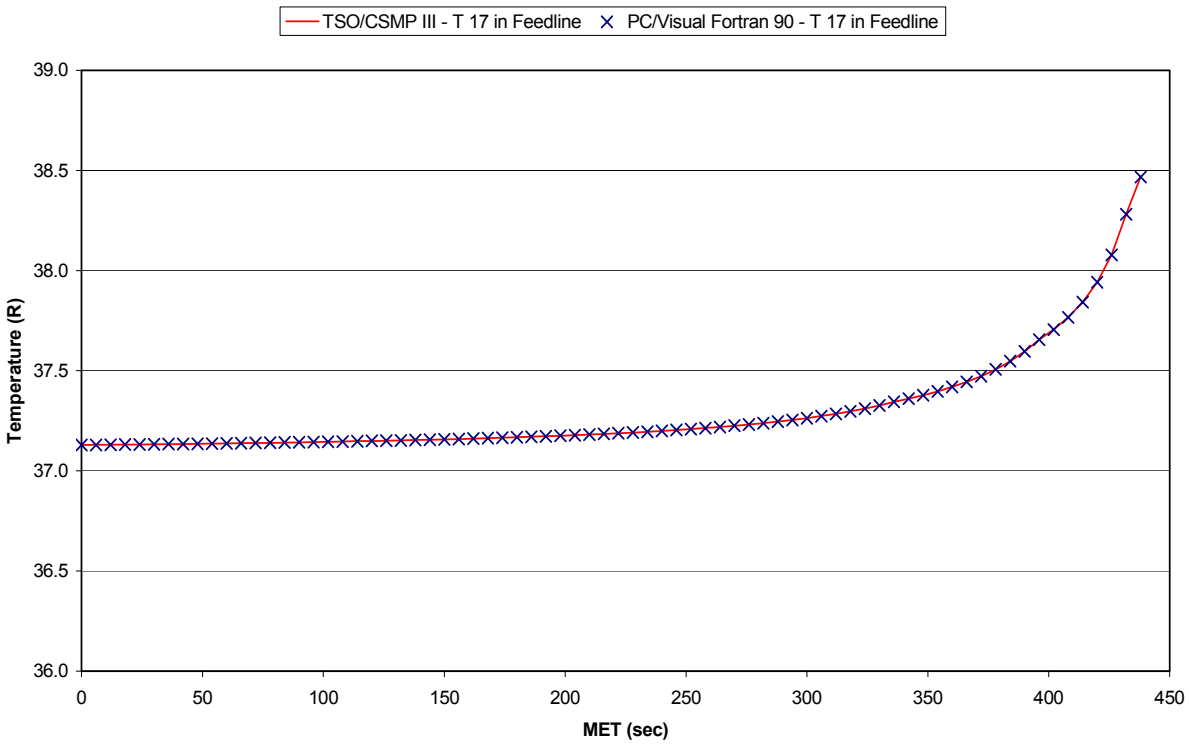

Figure 7.1-1. Typical Prediction of the LH_2 Temperature Profile

The total pressure (Po) at the LPFP inlet varies during ascent as it is a function of the hydrogen tank ullage pressure, the height of hydrogen in the tank, the acceleration along the flight path, and the losses in the fuel line system between the ET and the SSME. Figure 7.1-2 shows typical total pressure values which range from 35 to 22 psi for a nominal ascent.

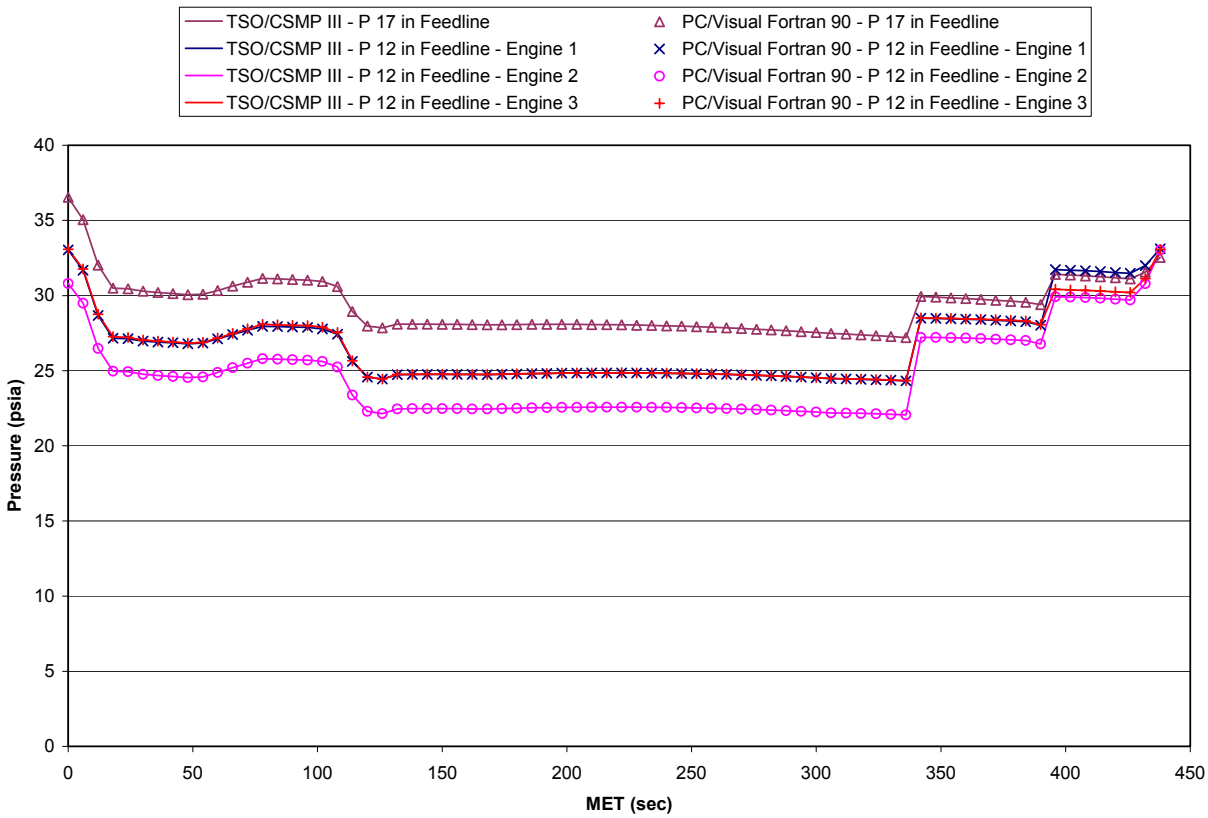

Figure 7.1-2. Typical Predictions of Feedline Total Pressure

The density of the mean flow is 4.4 lbm/ft^3, which yields an average velocity of 45ft/s and a dynamic pressure of 1 psi. Reynolds Number, based on the 12-inch diameter of the feedline, is around 21 million.

Significant perturbations to the static pressure are caused by cavitation of the LPFP inducer blades and reverse flow from the blade tips. The tip speed is 825 ft/s which produces a very high dynamic pressure at the tip (relative to the mean flow) of around 330 psi. Additionally, strong acoustic modes could occur due to resonances caused by the internal feedline geometry and the geometry of the cavity between the flowliners and the surrounding pressure bellows.

The cavity acoustic response will be sensitive to the speed-of-sound in the cavity, which can change significantly if two phase flow occurs in the cavity. Figure 7.1-3. shows how dramatically the speed-of-sound is reduced as a function of mixture ratio, alpha. Vapor can enter the cavity either from cavitation of the inducer which is convected in by the reverse flow, or direct boiling of the hydrogen at the wall due to heat transfer into the cavity.

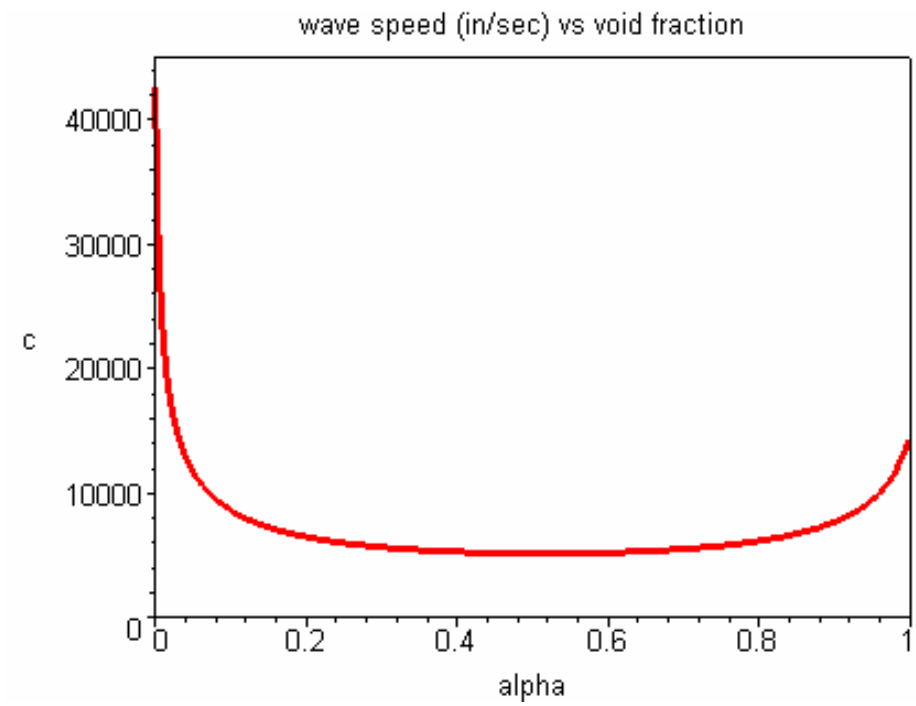

Figure 7.1-3. Speed-of-sound for Two Phase Hydrogen vs. Void Fraction, Alpha

7.1.1 Complex Environment

The gimbal joint flowliners are embedded in a complex environment that is not completely understood. The first example is cavitation which still must be investigated empirically. Rigorous theoretical based modeling techniques which can be used to produce consistent results for cavitating inducers do not exist. Thus, the cavitation aspect of this problem, which is significant, must be measured in a test. The second example is heat transfer into the flowliner bellows cavity. The flight environment, from this standpoint, is not known. Figure 7.1.1-1 shows the downstream end of the LH_2 feedline gimbal joint. Structural support for the feedline and the LPFP is provided by the large titanium 'horseshoe' structure that is bolted to slightly over half of the circumference of the gimbal joint flange. A heat transfer analysis that could

estimate the temperatures in the bellows cavity during ascent (including conduction through this component) is not readily available. This analysis is needed before it will be possible to design a ground-based test, which provides the proper heat transfer into the gimbal joint. And finally, knowing the correct geometry is essential for several reasons. The upstream duct elbows and internal components add large scale unsteady motions to the mean flow while the length (and geometry) change the acoustic modes and wall boundary layer profile. The reverse flow from the inducer tip is very sensitive to the tip clearance and wall velocity profile. Apparently, the tip clearance is not completely understood either, as the LPFP inducer rubs the pump housing during some portion of the flight. Also, the weld beads that were left in the flight gimbal joints and that were in the GTA, but not in the BTA, further complicate the situation. Their effect on the boundary layer and thus the inducer tip flow interaction has not been investigated yet.

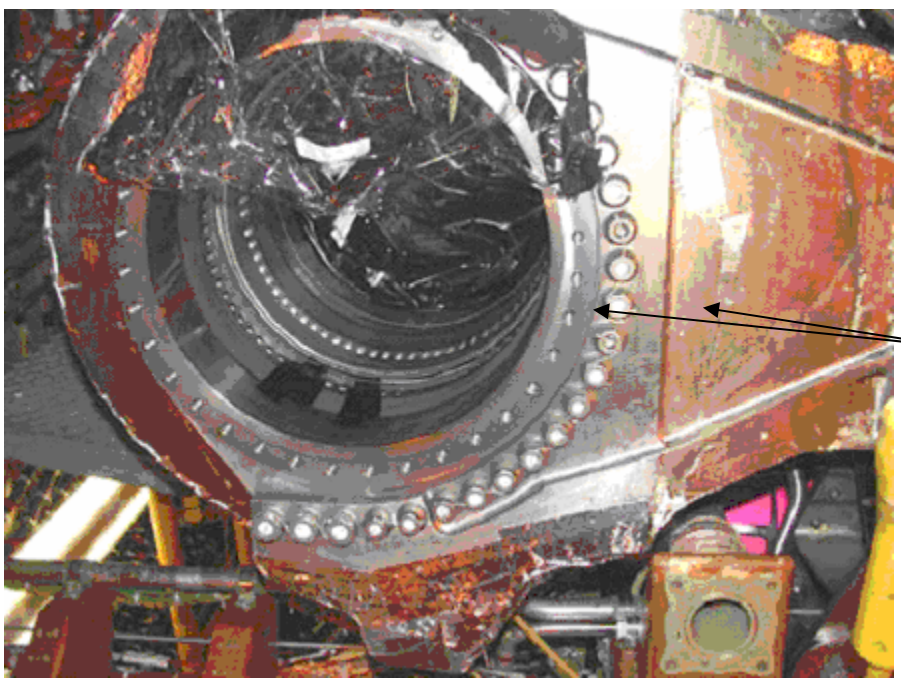

Figure 7.1.1-1. Gimbal Joint Downstream End and Orbiter 'Horseshoe' Structural Attachment

Another possible complication is the observation that the flowliner cracks appear to line up with the centerline of the horseshoe attach structure. Figure 7.1.1-2 shows the crack locations added to a drawing of the gimbal joint for Engine #1. The numbers correspond to the Orbiter, while blue represents a crack in the downstream flowliner, near the inducer, and green shows the crack location in the upstream flowliner.

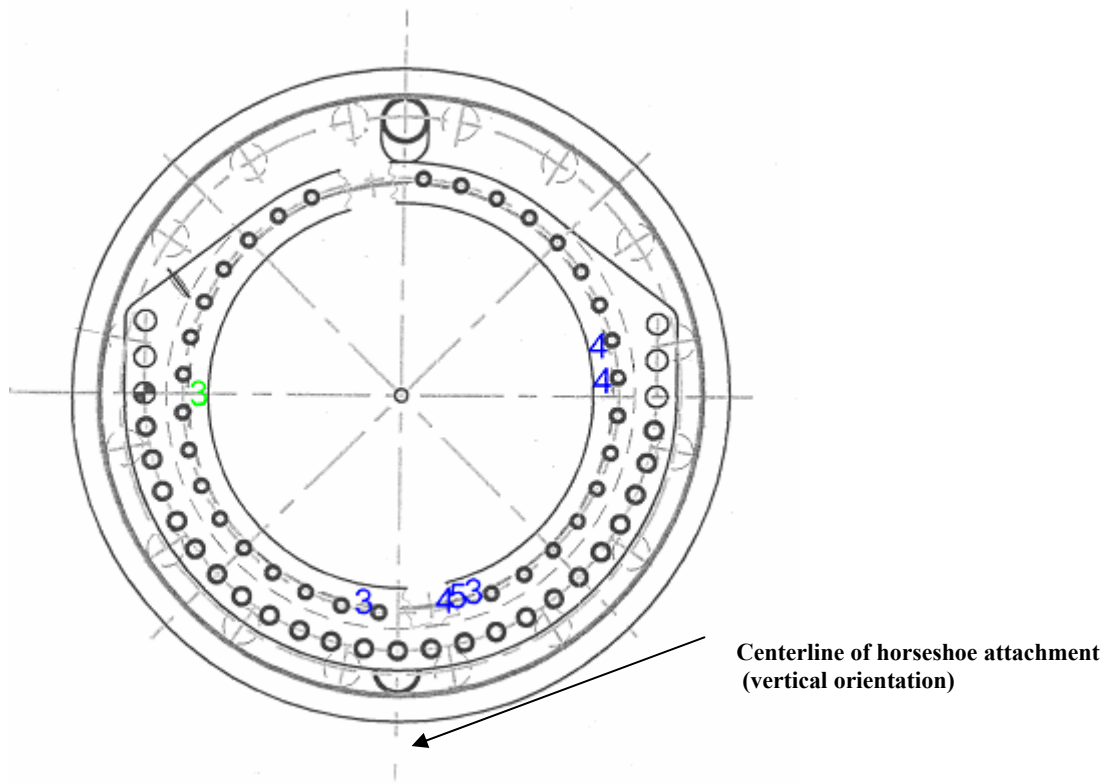

Figure 7.1.1-2. Engine #1 Crack Locations for OV-103, OV-104, and OV-105. Blue is the downstream flowliner, while green is the upstream flowliner.

Engine #2 only has one crack, which is on the upstream flowliner, for the Orbiters that have Inconel flowliners as shown in Figure 7.1.1-3. Columbia had three cracks, all on the downstream flowliner of Engine #2, as shown in Figure 7.1.1-4. Recall that the flowliners on Columbia were the original 76 slot design and were made from CRES, not Inconel.

While these patterns might not be significant, they indicate that there could be a correlation between the gimbal joint thermal and structural environment that has not been fully evaluated. As an example, the inducer tip clearance might not be uniform which would result in an amplitude variation for both the reverse flow and cavitation effects.

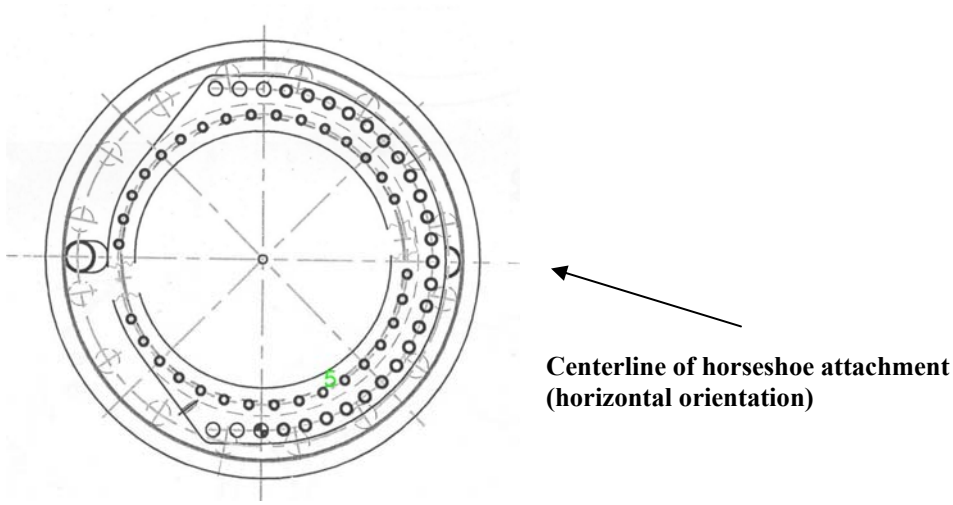

Figure 7.1.1-3. Engine #2 Crack Location on the Upstream Flowliner for OV-105

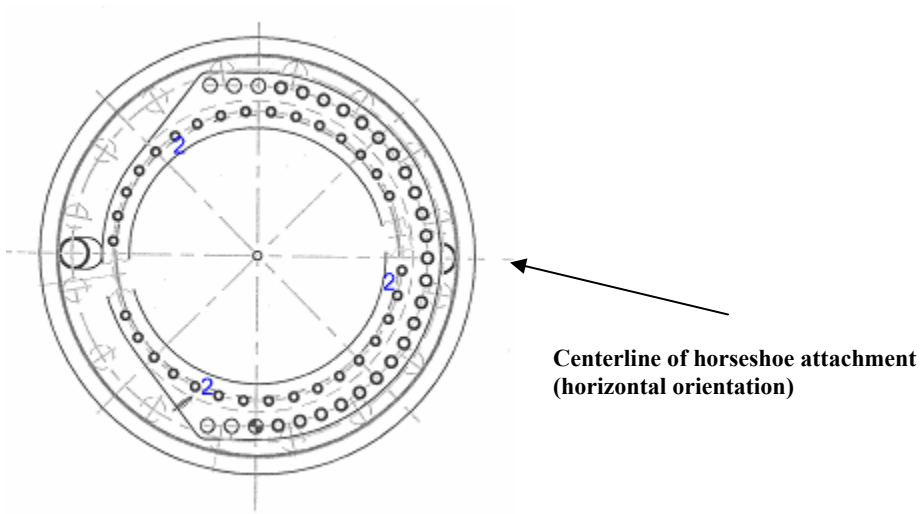

Figure 7.1.1-4. Crack locations on Engine #2 on the Downstream Flowliner of OV-102

7.1.2 A-1 Test Stand

Figure 7.1.2-1 shows the A1 test stand duct which was fabricated in the early 1970s to test the SSME. The internal components, elbows, and duct length are quite different from the Orbiter feedline system. Thus, the approach flow wall boundary layer, velocity profile, acoustics, and unsteady component to the mean flow will be different from the Orbiter. These differences need to be assessed to understand the differences between the test results and flight.

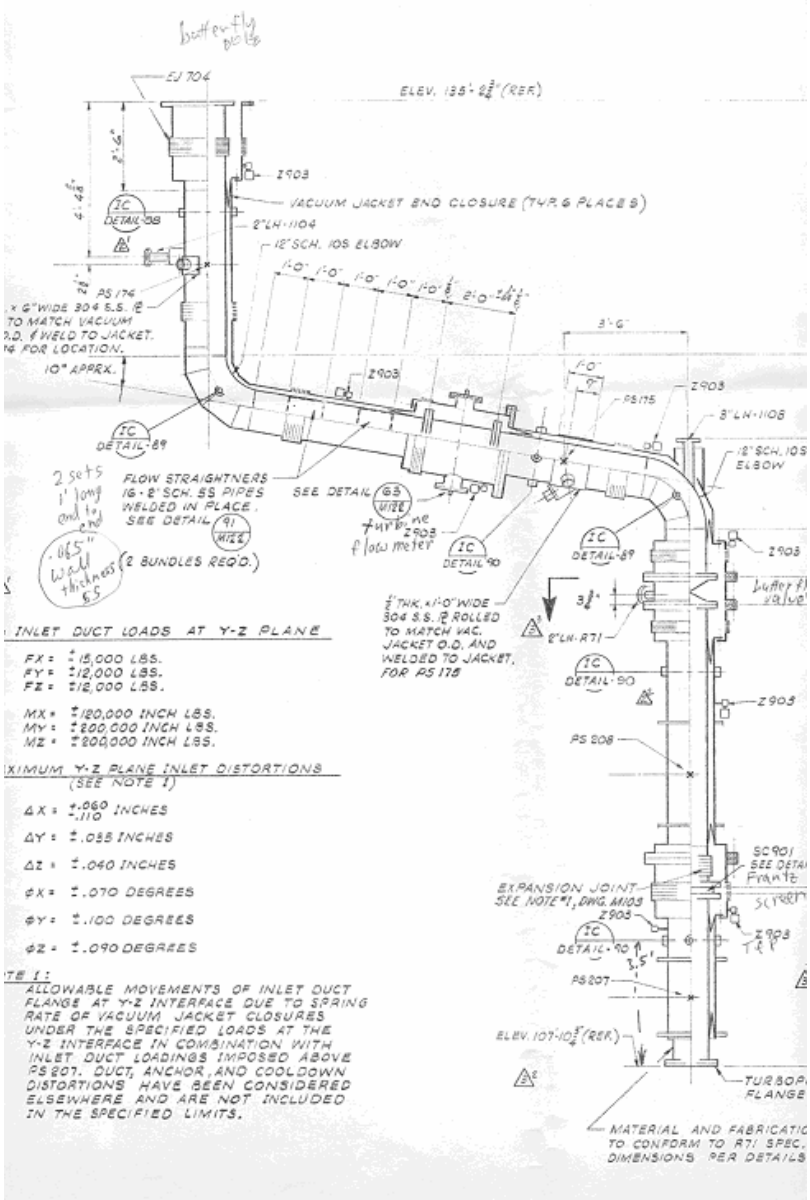

Figure 7.1.2-1. Stennis Space Center, A-1 Test Stand LH_2 Feedline Drawing

7.1.3 Correlating Test Stand Data to Flight

It should go without saying that accurate measurements of temperature and pressure, along with fuel flow rate, pump speed, etc., are essential to correlating the test stand results with flight. The accuracy of the measurements needs to be reviewed, as the pressure measurements on the Orbiter, upstream of the gimbal joint and at the flow rate meter between the two fuel pumps are known to have accuracy issues. The test stand measurement may also be of concern.

The gimbal joint outer shell is an Inconel assembly that is composed of two flanges at each end, which are welded to an inner cylindrical shell. The two flowliners are also welded to the inner shell. Thus, there are four circumferential welds whose weld bead is visible on the inner face of the gimbal joint. Figure 7.1.3-1 shows the downstream weld bead which joins the F1 flange to the inner shell. There is also a smaller weld bead where the flowliner is welded to the shell. Part of the smaller bead can be seen in the light from the flashlight.

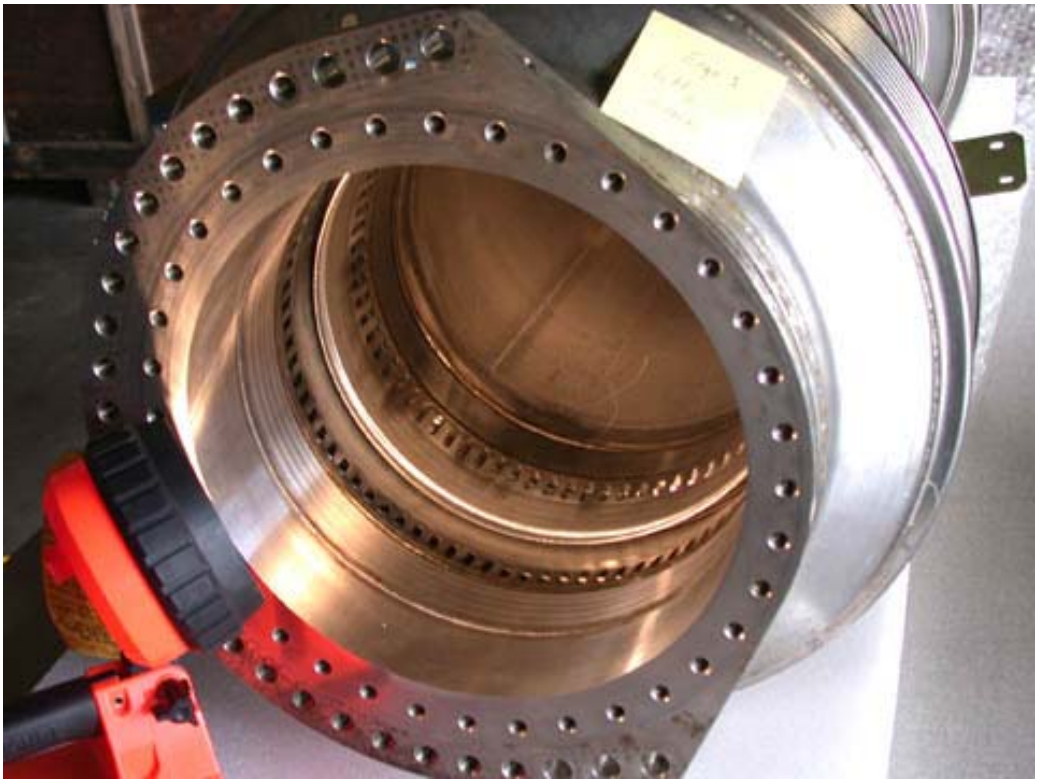

Figure 7.1.3-1. Downstream Weld Bead is clearly visible in this photograph of an LH_2 Gimbal Joint for Engine #1

A flowliner on OV-102 is shown in the figure and is thought to be typical of the fleet. However, considerable variation among the fleet flowliners has been reported. The downstream weld bead is close to the inducer and will cause local separation of the approaching flow and the reverse flow from the inducer blade tips. The upstream weld bead will also cause local separation of the approaching flow, and the reverse flow, if it reaches that far upstream. The smaller weld beads at the attachment of the flowliners might affect the acoustical tones caused by the slots, when the flow crosses the weld bead before crossing the slot.

Arrowhead Products fabricated the original gimbal joints and the GTA. The weld beads were left as welded. Based on a verbal description, the GTA had larger weld beads than the flight gimbal joints.

In contrast to the GTA, the BTA was fabricated at Stennis Space Center, where the interior dimension is routinely machined to an inner diameter of 12.07 inches. Thus, this machining removed the weld beads that joined the end flanges to the test article. The upstream half of the test article can be seen in Figure 7.1.3-2 which shows a smooth surface from the upstream end of the test article to the small weld bead at the flowliner attachment.

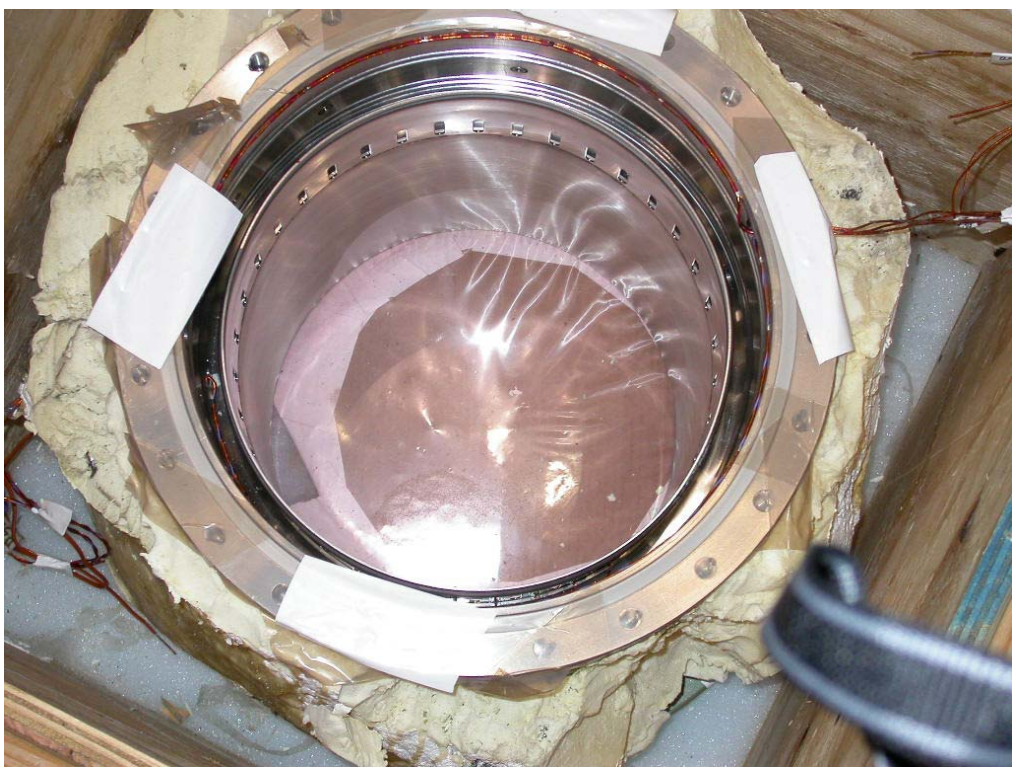

Figure 7.1.3-2. Upstream Half of the BTA

Recent CFD results by Dan Dorney show a significant effect due to the downstream weld bead at the LPFP's 4N frequency. The weld bead results show a much larger pressure oscillation than the smooth wall calculations. This difference will be further investigated during Phase II.

7.1.4 CFD Analysis

Three high resolution CFD grid systems have been created to provide insight into the complex flow field which results from the interaction of the gimbal joint flowliners and the inducer back flow. The INS3D code is used to compute the unsteady flow field as described in Appendix D.1. The liquid hydrogen is treated as an incompressible viscous fluid. In spite of the progress made in multi-phase simulations in recent years, cavitation modeling remains to be extremely challenging and is not mature enough to be used for predicting flow physics in a consistent manner, thus the simulation does not include any cavitation effects.

Model I

Model I simulates the "straight duct" test run on the A1 test stand, which did not include the gimbal joint. A 48-inch long straight duct grid system is joined to the inducer grid system which includes the correct bull nose hub geometry and all eight blades of the inducer (4 long, 4 short blades). The inducer tip clearance of 0.006 inches is included in the model. The resulting pressure variations, due to the reverse flow, are in good agreement with the measurements obtained on the A1 test stand during Test 901-940, as shown in Figure 7.1.4-1.

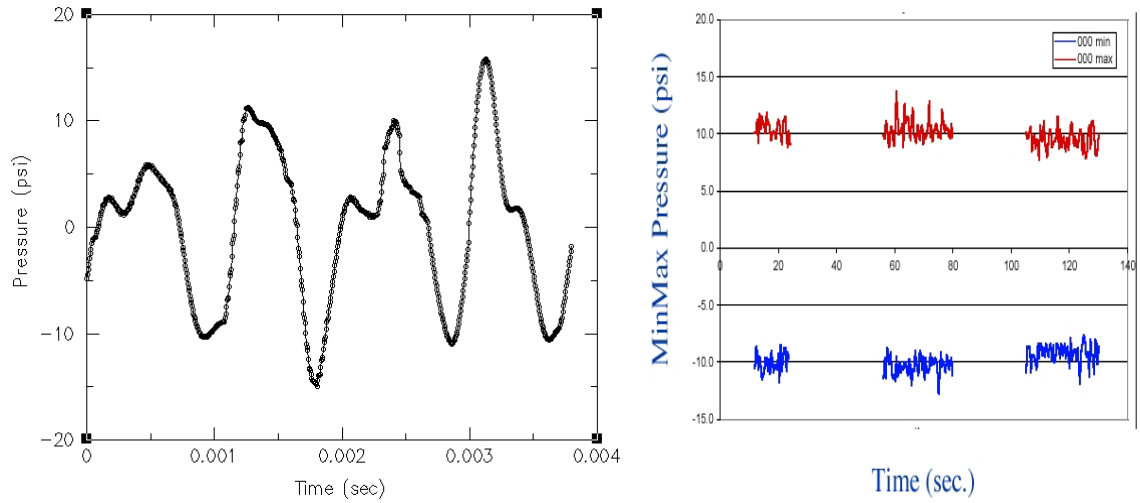

7.1.4-1. Time History of Static Pressure During One Inducer Rotation (Model I, 9th inducer rotation), and Min/Max values of pressure in Hot Fire Test

The CFD results show peak-to-peak pressure variations of between 10 to 15 psi for the 9th rotation of the inducer while the test data for the same power setting of 104.5 percent and high NPSP show similar magnitudes over about 50 seconds worth of test data.

Model II

The grid system for Model II includes the gimbal joint geometry built from the CAD representation of the flowliner and bellows cavity. Figure 7.1.4-2 shows the surface grids of the inducer, the flowliner slots, along with a cross section through the bellows cavity.

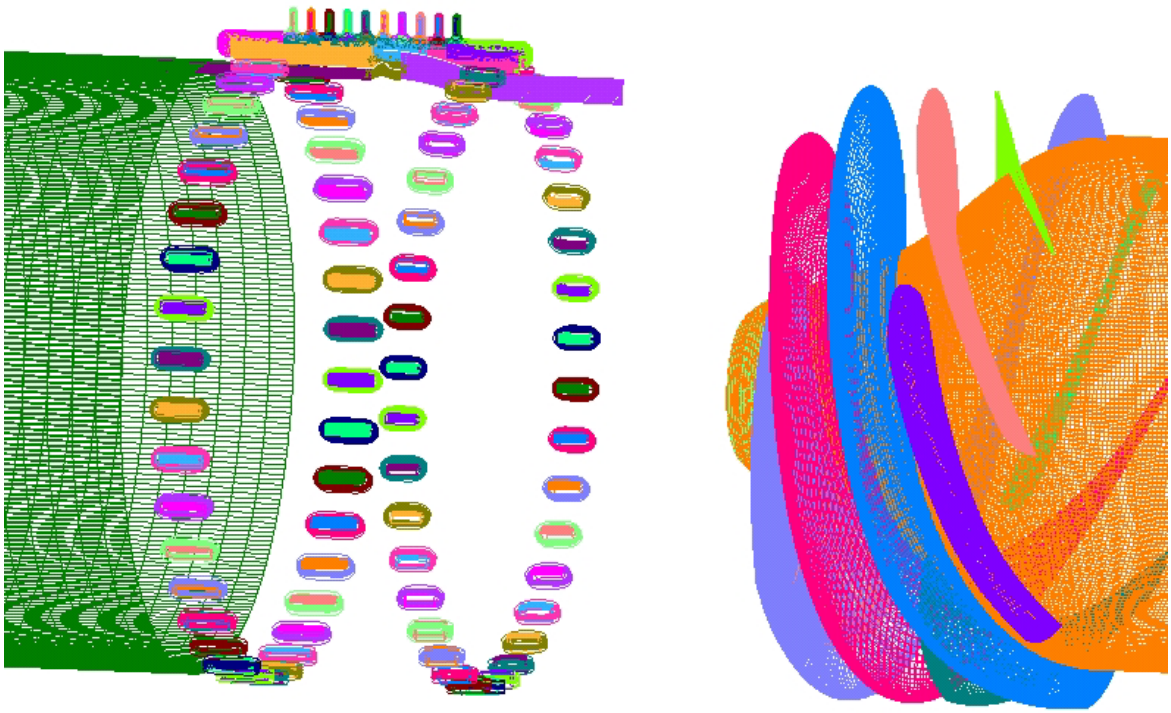

Figure 7.1.4-2. Surface Grids for LPFP Inducer and the Liquid LH_2 Flowliner

A close up of the bellows cavity is shown in Figure 7.1.4-3. The flowliner slots are resolved with 5 grid points across the thickness of the flowliner.

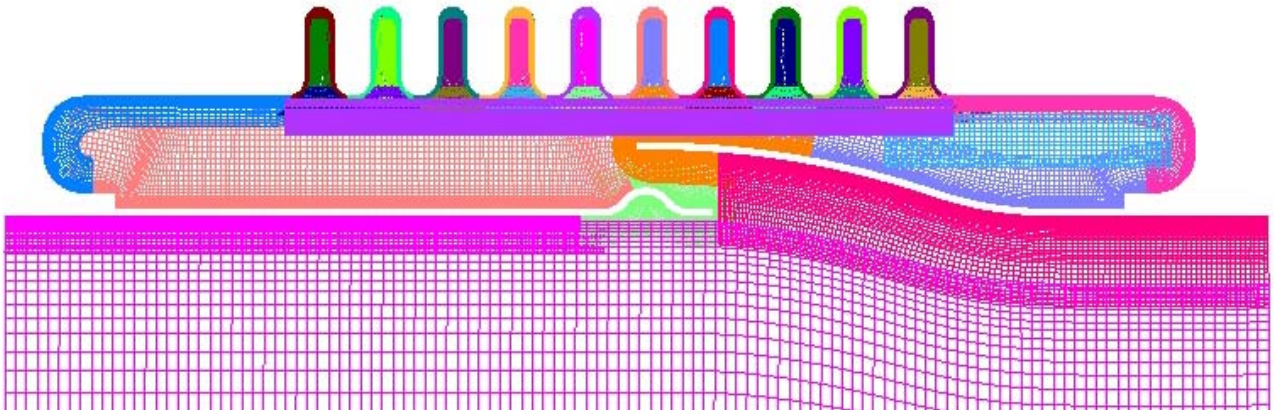

Figure 7.1.4-3. Details of the Flowliner Bellows Cavity Showing the Overset Grid System

The pressure distribution on the inducer blades, for the 5th rotation, at a power level of 104.5 percent is shown in Figure 7.1.4-4. The low pressures are shown in blue, while the red and magenta show high pressures. The suction side of the blade faces upstream, toward the reader.

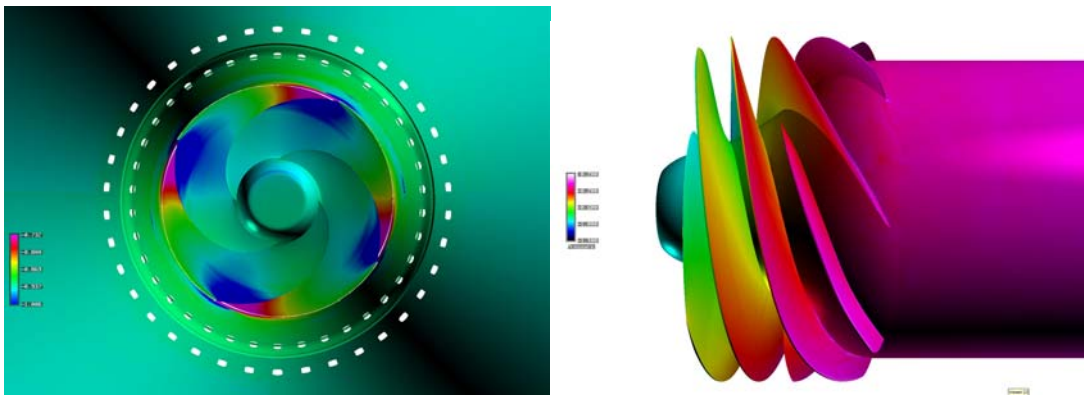

Figure 7.1.4-4. Inducer Pressure Distribution for the 5th Rotation

Figure 7.1.4-5 shows the reverse flow (in blue) entering the bellows cavity through the overlap between the two flowliners. The flow entering the cavity has a velocity of about 10 to 15 percent of the inducer tip speed.

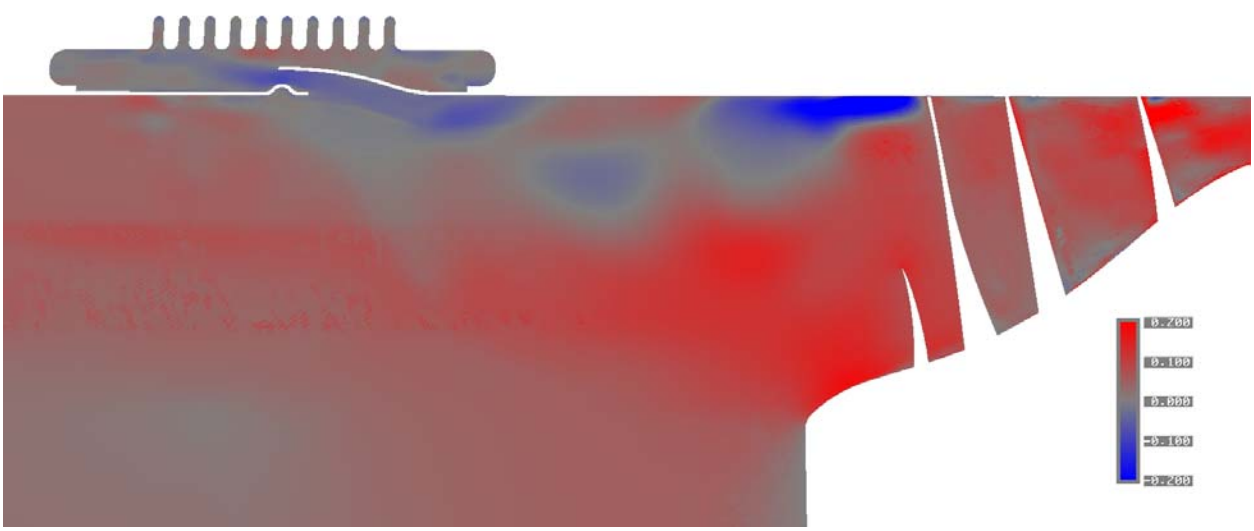

Figure 7.1.4-5. Axial Velocity Contours at an Instantaneous Time In Cut Planes Showing Reverse Flow In Blue

The CFD results appear to be modeling the fluid mechanics in a very acceptable manner and illustrate how complex the interaction is between the inducer reverse flow and the flowliner geometry. Please refer to the full report in the appendix for further details of the flow through the flowliner slots. A comparison of the unsteady pressures will be made to the BTA and GTA pressure measurements, once a time periodic solution has been obtained.

Model III

The third grid system is an extension of Model II, and includes the 64 degree elbow of the type II feedline for Engine #1 and the BSTRA that is downstream of the elbow. The grid system has been created, but the solution has not been started at the time of this report.

7.2 Development of the Fatigue Loading Spectra

Review of the Load Spectra Development

The development of the Shuttle MPS LH_2 feedline flowliner's load spectra was reviewed. The liners under investigation are the two flowliners immediately upstream of the SSME's LPFP. The load spectra are used to describe the load-time history of the liners during flight operations, and these spectra are used in durability analyses of the liners to determine the liners expected lives. The objective of the review was to understand the methodology and assumptions that were used to generate the load spectra. This review encompasses the development of the 'first-generation' or 'Boeing' load spectra presented in Figure 7.2-1 and Table 7.2-1 for the upstream flowliner and Figure 7.2-2 and Table 7.2-2 for the downstream flowliner. These load spectra are not certification load spectra. Certification spectra will be generated by the Program-sponsored team for the certification conditions specified by the Orbiter Program Office. The 'Boeing' load spectra represent a reasonable effort to generate a conservative loading that envelops the 'worst-case' flight loads of a typical flight.

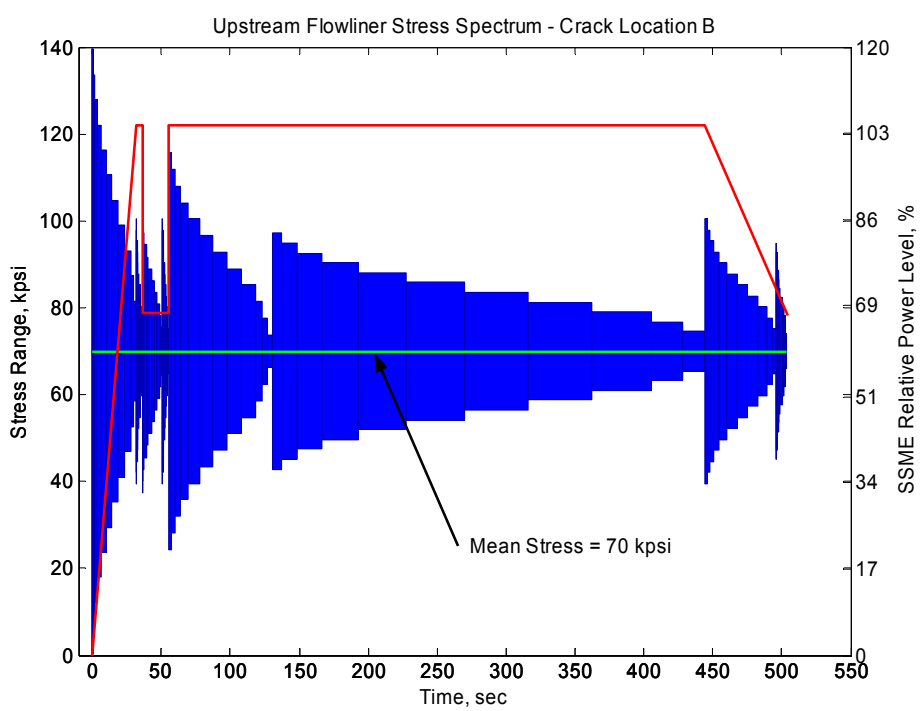

Figure 7.2-1. 'Boeing' Upstream Load Spectrum For Crack-Site B

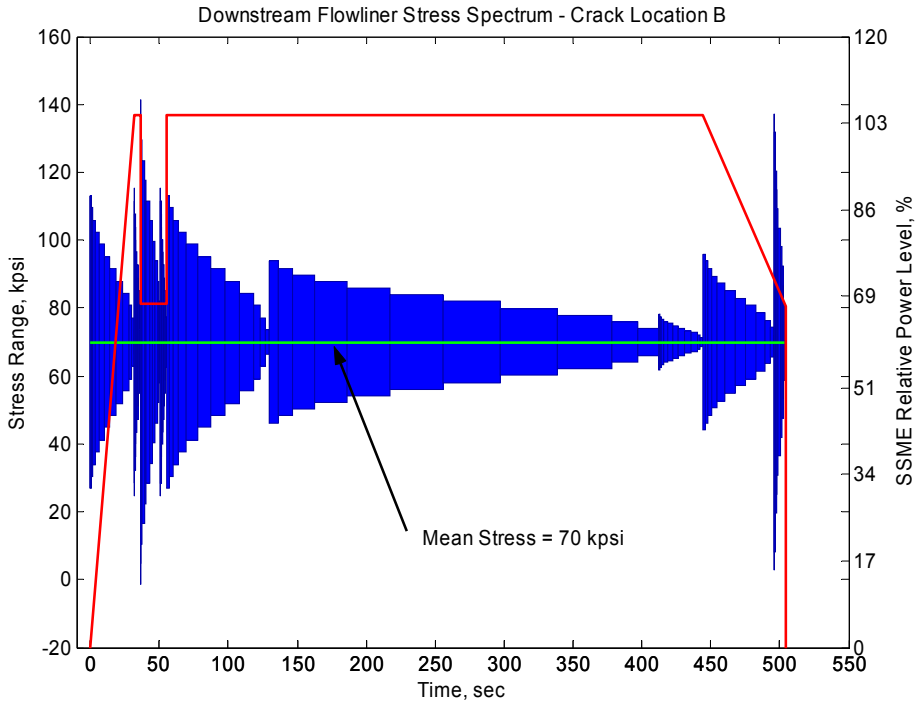

Figure 7.2-2. 'Boeing' Downstream Load Spectrum For Crack-Site B

Table 7.2-1. Upstream Flowliner Load Spectrum Parameters

Designation	'Boeing' Load Spectrum [Warren]
Liner	Upstream
Crack Location	'B'
Mean Stress	70 kpsi
Modulus	31.2 Mpsi

Block	Duration (sec)	Frequency (Hz)	Mechanism	Load Factor	Scale Factor	Transfer Ratio	Alternating Stress (kpsi rms)
1	32	3500	Edge tone or cavitation (C9ND)	1	0.8	2.9	23.2
2	4	3500	Edge tone or cavitation (C9ND)	1	0.8	2.9	10.1
3	15	3500	Edge tone or cavitation (C9ND)	1	0.8	2.9	10.9
4	4	3500	Edge tone or cavitation (C9ND)	1	0.8	2.9	10.1
5	72	3500	Edge tone or cavitation (C9ND)	1	0.8	2.9	15.2
6	317	3500	Edge tone or cavitation (C9ND)	1	0.8	2.9	9.0
7	52	3500	Edge tone or cavitation (C9ND)	1	0.8	2.9	10.1
8	7	3500	Edge tone or cavitation (C9ND)	1	0.8	2.9	8.3

Table 7.2-2. Downstream Flowliner Load Spectrum Parameters

Designation	'Boeing' Load Spectrum [Warren]
Liner	Downstream
Crack Location	'B'
Mean Stress	70 kpsi
Modulus	31.2 Mpsi

Block	Duration (sec)	Frequency (Hz)	Mechanism	Load Factor	Scale Factor	Transfer Ratio	Alternating Stress (kpsi rms)
1	32	10600	Pump backflow 4N (5ND)	4	1	0.6	15.0
2	4	3330	Edge tone (C4ND)	1.2	0.8	3	15.7
3	15	3330	Edge tone (C4ND)	1.2	0.8	3	24.7
4	4	3330	Edge tone (C4ND)	1.2	0.8	3	15.7
5	72	1070	Pump backflow 4N (5ND)	4	1	0.6	15.0
6	295	1650	Edge tone or cavitation (3ND)	1	1	1.2	8.24
7	32	1650	Edge tone or cavitation (3ND)	1	1	1.2	2.81
8	52	3330	Edge tone (C4ND)	1.2	0.8	3	9.0
9	7	3330	Edge tone (C4ND)	1.2	0.8	3	23.4

The methodology used by Boeing to develop a load spectrum for each flowliner is semi-empirically based, and it is complicated by the complexity of the loading environment during flight operations. The load spectrum development is further complicated by engine variability, flight profile differences, and the variability of the structural characteristics of the liners themselves. The consensus hypothesis is that the liners are subject to combined static and dynamic loading originating from residual manufacturing loads, static and quasi-static flight loads, and dynamic flow induced loads. Currently, there is no analysis tools or test facilities that can directly replicate the flight loading conditions seen by the flowliners. In addition, there are no in-situ flight load or response measurements to directly provide load spectra or verify analyses and tests. The methodology developed is a direct result of these handicaps and the types of information available at this time. The principal information source is the engine hot fire testing performed using several feedline/flowliner simulators (straight duct, BTA, and GTA). Other sources of information include LPFP acceleration data obtained from the Development Flight Instrumentation flown during the Orbital Flight Test, SSME performance data obtained

from each Shuttle flight, design information, and fluids, structural, thermal, and acoustics modeling of the MPS parts.

The methodology used by Boeing is anchored by performing investigations (analytical and data-mining) into determining and understanding the loading mechanisms observed during the engine hot fire tests and anecdotally observed from Development Flight Instrumentation flown during the Orbital Flight Test. Historical fleet engine performance data are used to determine the sequencing and timing of loading events. These loading events and engine conditions are correlated to the engine hot fire test data, and strain data are extracted and combined with the liner's structural dynamics model to determine the magnitude (stress) associated with the loading event. Load uncertainty factors and scale factors are used to scale up or down the recovered stresses such that the loads are conservative but realistic (within engineering judgment). Finally, the cyclic distribution of the loading event is computed by scaling a normalized Rayleigh distribution to fit the load magnitude and frequency of the loading event. Each loading event is temporally assembled to create the final load spectrum.

Specific summary observations are provided below.

1. The flowliners are subject to a combined static and dynamic loading environment. The static loads originate primarily from residual manufacturing loads. The dynamic loading is driven by the local flow effects of the LPFP. The primary sources of dynamic loading are backflow from the pump, cavitation, and acoustic effects driven by the flow field.
2. Due to engine-to-engine variability, environmental factors, and flight profile differences, a deterministic load history cannot be created for a 'typical' flight. The Program has adopted a methodology to create a maximal or 'worst-case' load history to be used for the certification of the flowliners. The 'Boeing' load spectra represents a first cut attempt to derive the 'worst-case' load spectra for a typical flight. There is no provision for off-nominal events. Conservative factors include, but are not limited to:
    a. All damage accumulates at one location independent of loading condition.
    b. Load factors are used to scale loads up to account for uncertainty or to scale loads down to account for obvious over-conservatism.
    c. During a loading segment or block, if a resonance condition is found to exist, it is assumed to exist throughout the event. There is no relief due to changing conditions, i.e., de-tuning.
3. Since there are no direct flight measurements to provide load spectra or verify analyses and tests, the flowliner load spectra are determined in a semi-empirical fashion from circumstantial analyses and tests. Central to the load spectra development is the BTA and GTA testing performed at the Stennis Space Center. Flow phenomena observed in BTA/GTA tests are assumed representative of the fleet. Strains associated with liner

events are extracted from the BTA/GTA data, and structural dynamics models are used to relate the measured strains to the crack-site strains (transfer ratio). There are three practices that violate the concept of a conservative loading spectrum:

1. The transfer ratio approach mandates several assumptions that may not be conservative. For example, the transfer ratio method requires an a priori knowledge of what liner modes are reacting to the excitation loads. If the mode selection is in error, then the transfer ratio is incorrect. There would be no guarantee of conservatism.
2. Both alternating and bending stresses are assumed to act in bending; there is no accounting for membrane stress. For some structural modes, the membrane stress is the dominant stress. By not incorporating membrane stress there is no guarantee of conservatism.
3. Initial load spectra were developed using an assumption that the cycle counting of the liner response would follow a Rayleigh distribution. This is contradictory to the assumption/observation that the liner's response is characterized as narrow-banded resonant response. The Rayleigh distribution is insufficient in representing the cycle counts from a narrow-band process.

Complete details of this assessment are provided in Appendix D.2.1.

Development of Loading Spectra for a Nominal Flight

As part of the loading spectra assessment, the NESC ITA Team developed loading spectra for a nominal flight using the BTA test data. The nominal flight is the STS-110 Engine #1. The engine data received consists of two sets: (1) time vs. Q/N and power level and (2) cavitation parameter Nss vs. Q/N. Power and Q/N versus time is shown is Figure 7.2-3. The underlying critical assumption in the development of loading spectra is that flow-induced test strain responses are flight-like responses. However, it should be noted that test trajectories map partial flight trajectories in the Nss vs. Q/N plane. The hot fire tests were not meant to simulate a particular flight or portion of it.

The process followed to define the loading spectrum for the nominal flight is as follows:

1. The Nss vs. Q/N nominal flight trajectory is divided into 7 blocks of time or events. The rationale for this division is that hot fire test trajectories will be compared with these flight trajectories and provide the basis to extract test strain responses that would correspond to that segment of the flight. Values of Nss vs. Q/N for flight STS-110 and the selected blocks are shown in Figure 7.2-4 (B1 being 'lift off to 104 percent' and B7 '3G down').

2. Test trajectories that map blocks of flight trajectories in the Nss vs. Q/N plane are identified within the BTA runs 955 to 958 (strain gage instrumented). Figure 7.2-5 shows the nominal flight and the BTA runs 955-958.
3. Test time intervals are obtained for each flight block. Table 7.2-3 summarizes flight and test time start, end, and intervals for each block.
4. Loading spectra are calculated for strain gages that are selected because they showed the highest RMS responses during the test time interval identified. The selected strain gages were D9.5 and D47 for the upstream and B132 and B161 for the downstream flowliner from various BTA runs.

The main differences with the Boeing "worst case nominal loading spectra" approach are as follows:

1. The lift-off event for the ITA spectrum is split into two blocks. This is because there are two different zones in terms of Nss vs. Q/N for the lift-off and the crack growth has been demonstrated to be very sensitive to the initial loading.
2. The flight power level (FPL=104 percent) is kept as one trajectory instead of two trajectories (with and without the solid rocket boosters). This is because there is a single mapping in terms of Nss vs. Q/N for this portion of the flight; and the presence of the solid boosters does not seem to relate directly to the high frequency flow induced loads in the liners.
3. In the NESC ITA approach, the following rationale is used:

   The entire data block is analyzed, not just the 0.4 second interval that contained the highest response. The resulting load spectrum is adjusted to the flight condition by scaling the number of counts in each load level from the test block duration to the flight segment duration. For example, the counts in a 4 second test block are multiplied by 8 to create a 32 second flight block.
4. The bucket, or block 4, is not represented by any BTA trajectory. Boeing's run/strain gages have been used for the bucket block.

Finally, none of the BTA runs fully map a flight trajectory in terms of Nss vs. Q/N, the selection of strain gages and time intervals would have been the same even if the so called "nominal flight" had been chosen from another flight or engine. In other words, any loading spectra developed for a nominal flight would be very similar. In this respect, the loading spectra produced for this "nominal flight" would envelope any variation of flights and engines so long as the trajectories map "within reason" in the Nss vs. Q/N plane. Trajectories such as 109% power level would probably not fall "within reason" and would not be covered by these loading spectra.

Refer to Appendix D.2.2 for complete details on this analysis.

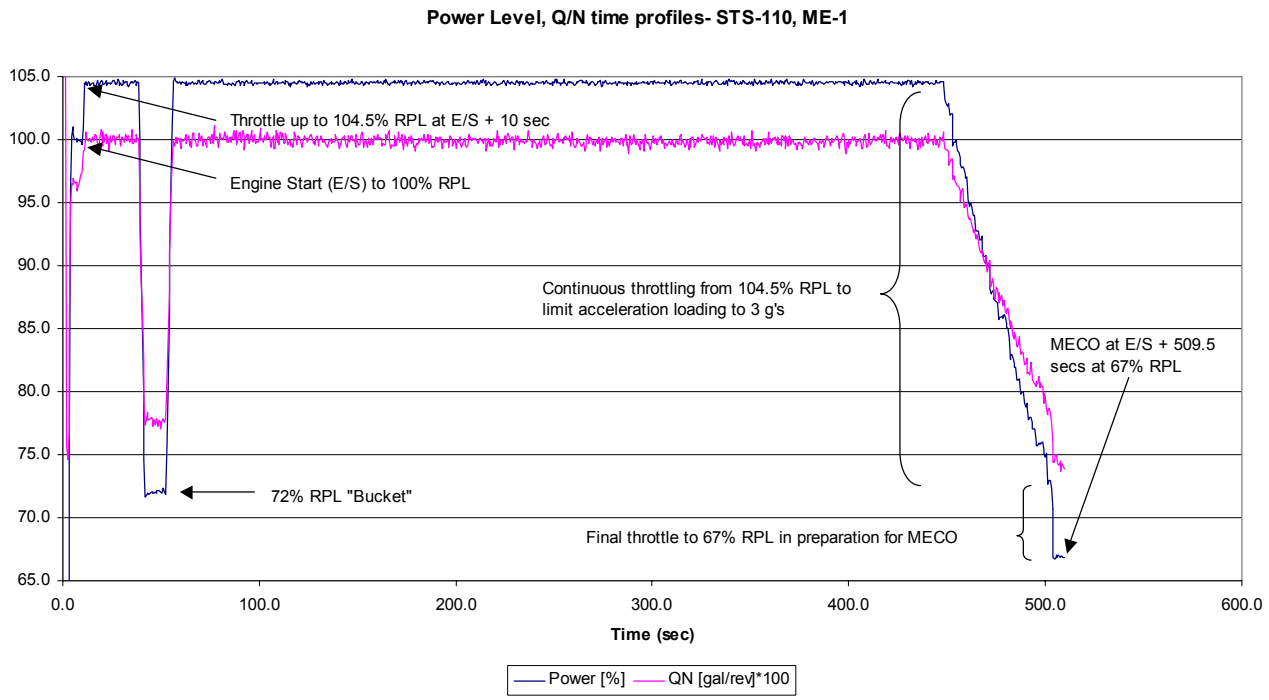

Figure 7.2-3. Power Level, Q/N time Profiles - STS-110, ME-1

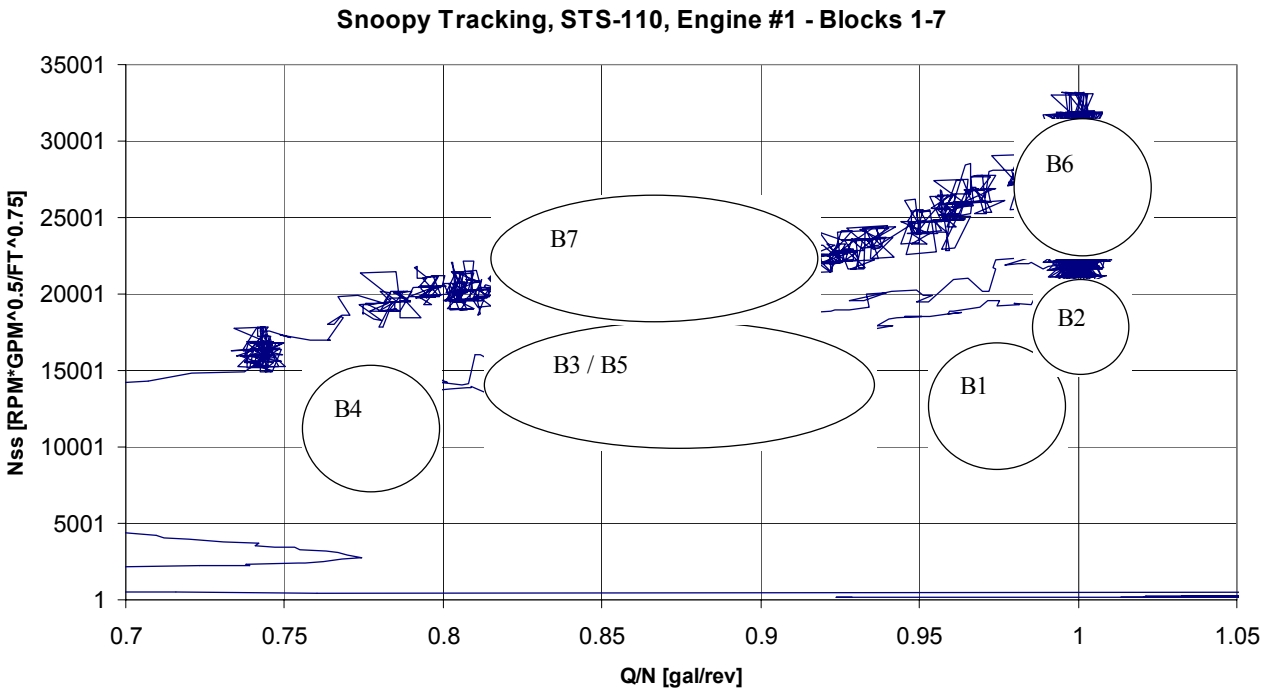

Figure 7.2-4. Snoopy Tracking, STS-110, Engine #1- Blocks 1-7

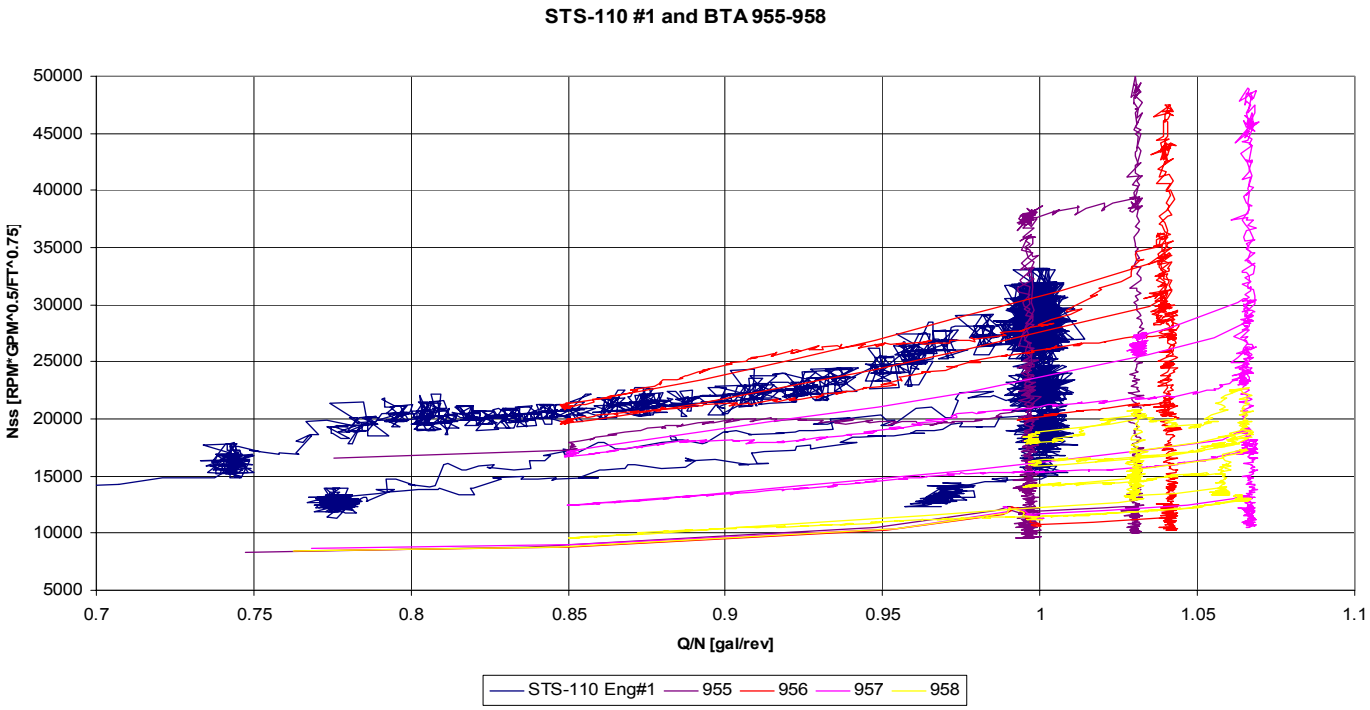

Figure 7.2-5. STS-110 #1 and BTA 955-958

Table 7.2-3. Flight and Test Time Intervals

Block #	Flight Event / BTA Run#	Start Time	End Time	Total Time
1	Lift Off to 104 %	0	12	**12**
	955	4	10.4	**6.4**
	956	4	10.4	**6.4**
	957	4	10.4	**6.4**
	958	4	10.4	**6.4**
2	104 % pre ramp down	12	38.5	**26.5**
	955	422.4	454.4	**32**
	956	122.4	162.4	**40**
	957	82.4	134.4	**52**
	958	122.4	138.4	**16**
3	ramp down	38.5	43.5	**5**
	956	518.4	580.4	**62**
	957	282.2	342.4	**60.2**
5	ramp up	52.5	59	**6.5**
	955	478.4	520.4	**42**
	957	334.4	346.4	**12**
6	accelerated	59	448.5	**389.5**
	955	260.4	290.4	**30**
	956	154.4	182.4	**28**
	957	222.4	274.4	**52**
	957'	362.4	394.4	**32**
	958	554.4	598.4	**44**
7	3G down	448.5	509.5	**61**
	956	202.4	262.4	**60**
	956'	314.4	374.4	**60**
	957	662.4	725.2	**62.8**
	958	642.4	725.2	**82.8**

Determination of Transfer Ratios

An independent technical assessment of the initial Boeing transfer ratios was performed. The "transfer ratio" is the strain ratio between a crack location and a measured strain gage location for a specific mode shape of interest. (The modes of interest are those included in the fatigue loading spectrum). Figure 7.2-6 is a sketch of part of a flowliner showing the crack sites of interest. The transfer ratios are approximate attempts to use strain gage measurements at mid-ligament locations to infer strain at the crack locations at the edges of the slots, called A, B, C and D. The measurements come from strain gages on either the BTA or the GTA. The strain gages were placed on the outside (OD) surface of the flowliners at the mid-ligament location between slots as illustrated in Figure 7.2-6.

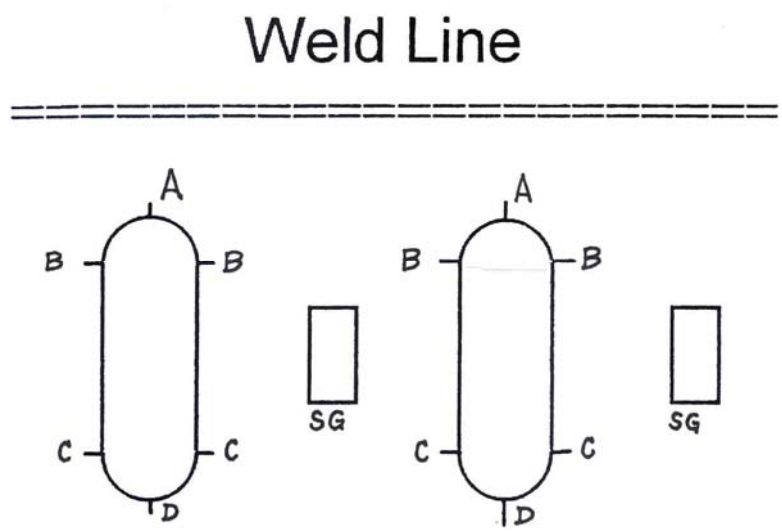

Figure 7.2-6. Two flowliner slots showing potential crack sites A B C and D and two strain gage locations used in tests <u>(not to scale)</u>

Transfer ratios are computed from the finite element models (FEM) originally assembled by Marshall Space Flight Center. However, the original finite element mesh has been changed to improve the accuracy of the NESC ITA transfer ratios. The model was enhanced by replacing the triangular elements at the slot edges with QUAD-4 elements and making coincident the nodes of the springs at the boundary between shell and weld. The latest models have been verified by the modal survey test, but still do not match the flowliner hardware exactly. (See Appendix D.2.4 for details). This is because (1) the model remains an approximation (despite

significant efforts), and (2) each flowliner in the STS Orbiter is slightly different. Figure 7.2-7 shows the Upstream Flowliner FEM.

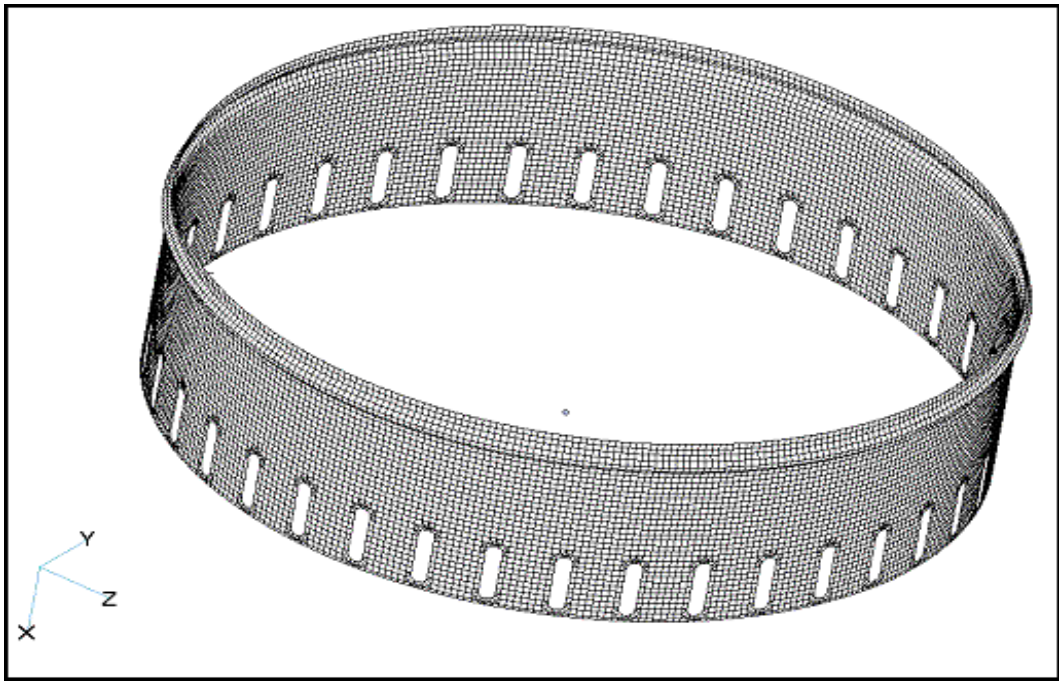

Figure 7.2-7. The Upstream Flowliner FEM

Transfer ratios are computed from the equations provided below.

The components of strain are defined as follows:

$\varepsilon_{SG,M,L}$ is the average strain over the assumed area covered by the strain gage

SG = strain gage
M = mode number
L = location (ligament 1-38)

$\varepsilon_{A,M,L,Edge}$ is the point strain tangential to the edge of the slot at a crack site

A = site (A, B, C or D)
Edge = inside (ID) or outside (OD) diameter

The transfer ratio is defined as:

$TR_{A,M,Edge}$= (Maximum of $\varepsilon_{A,M,L,Edge}$ over all L and both edges) /
(Maximum of $\varepsilon_{SG,M,L}$ over all L)

The bending and membrane components are then computed by the following relationships:

$$TR_{A,M,Bending} = 0.5\ (\ TR_{A,M,OD} - TR_{A,M,ID}\ )$$
$$TR_{A,M,Membrane} = 0.5\ (\ TR_{A,M,OD} + TR_{A,M,ID}\ )$$

The transfer ratio is determined from the maximum strain from all BTA gauges. Also, the crack site with the highest strain is the location used in the fracture mechanics analysis. However, these two locations (the site of maximum strain and the site of the crack of interest) do not usually occur at the same slot number of a flowliner.

The transfer ratios for the mode shapes of interest are compiled in Table 7.2-4. It is interesting to note the large membrane component for many of these factors. It is essential to define both the bending and membrane components because fracture mechanics analysis treats each one differently. Before the transfer ratios compiled in this table were computed, it was assumed that bending would dominate, and, in fact, was the only term used in the early analyses of crack growth. The results are compared to the existing Boeing data that have been used for initial fatigue analysis.

Table 7.2-5 shows that for all modes, the current factors are larger than the Boeing values. This increase is most likely due to three causes. First, the maximum strain is found over 38 slots, inside or outside diameter, and for B and C, two locations per slot. Second, the strain in the denominator is averaged over the area covered by a gauge. Third, the improved finite elements at the slot result in higher values of strain than the original FEM mesh.

Table 7.2-4. The Transfer Ratios for a Few Modes

FEM Nat. Freq. (Hz)	Mode Shape	Transfer Ratios: Bending / Membrane			
		Site A	Site B	Site C	Site D
Upstream Flowliner					
3136	C9 ND	-0.31 / 1.29	-1.91 / 1.58	1.43 / 1.65	1.79 / 0.89
3556	Shear	-0.54 / 7.53	-2.06 / 9.00	-0.87 / 9.77	-0.33 / 7.33
Downstream Flowliner					
1337	5 ND	-0.16 / 0.51	0.14 / 0.53	0.61 / 0.31	-0.03 / 1.17
2150	3 ND	-0.17 / 0.85	-0.03 / 1.35	0.50 / 0.96	-0.09 / 1.34
3283	C9 ND	-0.52 / 1.37	0.99 / 2.22	-1.80 / 1.89	-3.30 / 2.56
3514	C4 ND	-0.60 / 1.62	-0.91 / 2.50	1.65 / -1.64	0.98 / 3.01

Table 7.2-5. Comparison to the Boeing Data

TR_{MAX} = Maximum TR at either ID or OD

TR at OD = $TR_{BENDING} + TR_{MEMBRANE}$

TR at ID = $TR_{BENDING} - TR_{MEMBRANE}$

FEM Nat. Freq. (Hz)	Mode Shape	Max Transfer Ratio At Site B	
		By Swales	By Boeing [2]
Upstream Flowliner			
3136	C9 ND	3.49	2.90
Downstream Flowliner			
1337	5 ND	0.67	0.6
2150	3 ND	1.38	1.2
3514	C4 ND	3.41	2.4

Complete details on the determination of the transfer ratios are provided in Appendix D.2.3.

Development of Fatigue Loading Spectrum Using Rainflow Method

Several spectra, including Boeing's, have been assessed for various cases and have been used as inputs to fracture mechanics analyses performed by the ITA Team.

A preliminary look at the process that Boeing followed to generate loading spectra was determined to be conservative. For example, for the upstream liner, Boeing divided the entire flight into 8 time intervals (blocks), for each block the worst RMS strain gage response was obtained based on a 0.4 second interval. In this case, a total of 0.4*8 = 3.2 seconds of the worst responses was used to determine the loading spectra for the 500 seconds of flight. This means ~0.6 percent of the worst test responses to represent the full powered flight.

The validity of the assumption that the response of the liner is single modal was investigated through a frequency analysis of the strain gage data. While several flight blocks did record a single frequency dominated liner response (see Figure 7.2-8), which probably indicates a single modal response of the structure, several blocks included wide-band strain activity that is not indicative of a single modal response (see Figure 7.2-9). Because the Boeing-developed transfer ratios are based on the assumption of a single modal response, these results indicate that additional work analyzing the modal response characteristics of the flowliners was necessary. Such work is currently in progress.

The NESC ITA Team selected the rainflow method of cycle counting to develop the fatigue loading spectra. The rainflow method is a standard way to develop fatigue load spectra, has been used for over 20 years by almost all aerospace firms, and is applied here to the BTA/GTA test data. Though the results are termed the "load spectrum", it is in reality just the number of cycles, assumed to be fully reversible, at each strain level. There is no frequency definition either real or implied. An example of a Rainflow-generated loading spectrum is shown in Table 7.2-6. Each column of data represents a unique segment of the nominal flight profile that is defined by the conditions recorded during the test and expressed by the parameters Nss (cavitation), Q/N (flow rate) and RPL (relative power level). The nominal flight profile shown includes seven segments, or blocks, while the Boeing cases were comprised of eight blocks for the upstream liner and nine blocks for the downstream liner.

Rainflow-generated loading spectra was performed and delivered to the ITA for the following cases:

a) Upstream and Downstream Flowliners: 0.4 seconds (comparison with Boeing).
b) Upstream and Downstream Flowliners: 1.0, 4.0 seconds. This was a sensitivity study centered on the Boeing generated spectra.
c) Upstream and Downstream Flowliners: Nominal Flight for two strain gages per liner, described in the previous section.

Complete details of the development of the fatigue loading spectra are located in Appendix D.2.4.

Table 7.2-6. Nominal Profile Using The Rainflow Method for the Shuttle Upstream Flowliner

Percent of Maximum	Number of Fatigue Cycles						
	Block 1 (12 s)	Block 2 (26.5 s)	Block 3 (5 s)	Block 4 (9 s)	Block 5 (6.5 s)	Block 6 (389.5 s)	Block 7 (61 s)
100 %	0	0	0	0	0	7	0
90-100 %	0	3	0	0	0	7	0
80-90 %	0	22	0	0	0	150	0
70-80 %	0	117	0	0	0	1004	0
60-70 %	0	526	0	0	0	4562	0
50-60 %	0	2108	0	0	0	14808	0
40-50 %	24	6328	1	2	0	38253	0
30-40 %	452	15194	30	135	12	80462	0
20-30 %	4911	26574	768	3785	712	160144	419
10-20 %	19995	29971	6649	14936	8422	492306	33748
7 10 %	7781	6457	3887	2736	5525	249962	46517
5-7 %	4251	3018	2623	1512	3753	155073	47025
2-5 %	3943	2925	2845	2194	3943	158324	69316
0-2 %	1243	1056	839	1292	1102	50268	20481
Total	42600	94299	17642	26592	23469	1405330	217506

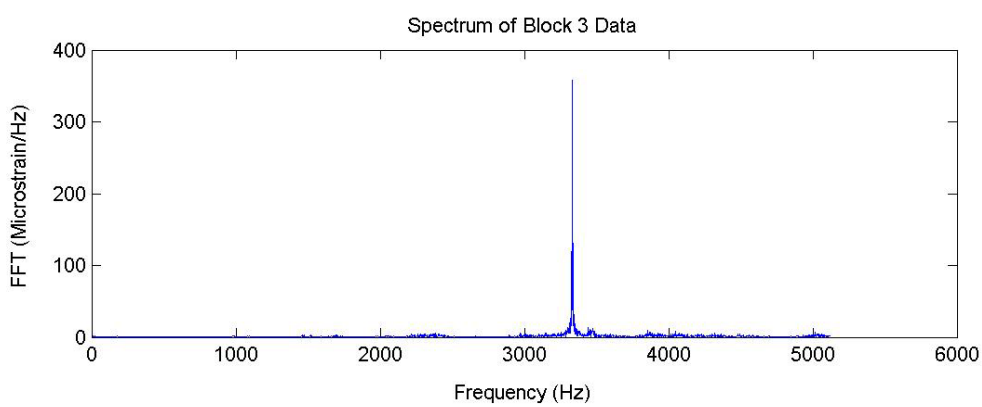

Figure 7.2-8. Frequency Response of Downstream Flowliner

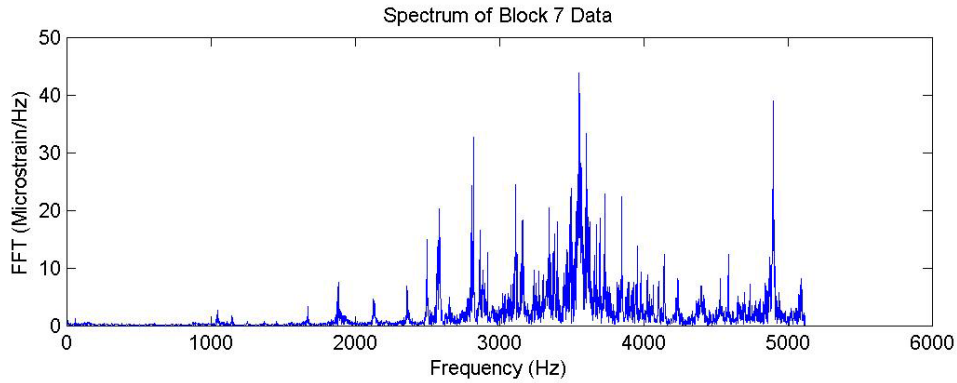

Figure 7.2-9. Frequency Response of Upstream Flowliner

7.3 Damage Tolerance (Fracture Mechanics) Analysis Methods and Results

Part I: Sensitivity Study based on the Transfer Ratio Approximation Method

The objectives of the NESC ITA fracture mechanics study were to use and develop as needed fracture mechanics tools to assess the effects of residual stresses, loading spectra, and crack detection threshold on the fatigue life of the liners and independently verify the Boeing and Marshall fracture mechanics analyses. This section describes the sensitivity analyses performed to identify the first order effects on residual fatigue life of the flowliners. Fracture mechanics analyses of the upstream and downstream flowliners were performed for the circumferential cracks at location B. (See Figure 7.2-6). The focus of the current study was on location B because all preliminary investigations indicated that this location was the crack location that controlled the fatigue life of the flowliners. The residual fatigue lives were evaluated for circumferential quarter-circle corner cracks using the NASGRO computer code. These corner cracks were assumed to have initial crack lengths of 0.075, 0.020, or 0.005 inches on the outside diameter (OD) side of the flowliner at slot location B. The stress-intensity factors from the literature for the corner crack and through crack configurations were blended to develop the stress-intensity factors for the crack configurations considered herein. Residual (mean) stresses of 70, 50, or 30 ksi were assumed at location B. Three material models for crack growth were used. These are the Baseline (using various R-ratios curves in the da/dN - ΔK data), Intermediate (using only R = 0.9 growth data), and Conservative (growth data obtained using ΔK threshold by extrapolating Paris regime lines to 10^{-9} in./cycle) material models. Inconel 718 crack growth rate data obtained from tests in liquid nitrogen (LN_2 @ -320° F) and liquid helium (LHe @ -423° F) were used. Results were calculated for three NESC spectra, previously discussed in Section 7.2, and were developed using the rainflow cycle counting method.

The engineering report presenting the complete details of the fracture mechanics analysis methods, sensitivity studies, and results is located in Appendix D.3.1. Only the results from the fracture mechanics analyses are presented in detail in this section.

Assumptions in the Current Analyses

The following assumptions are made in the analyses that are presented in this section:

1. Residual stresses are assumed to have a value of 70 ksi at location B, which is constant across the ligament between the slots. The residual stresses do not get relieved and have the same value of 70 ksi as the crack grows.
2. The alternating component of loading is fully reversed.
3. A single mode is predominant in each block of the loading; however, the predominant modes can vary from block to block.
4. In each block, modal interaction effects are not considered.
5. For each loading block, the peak stress is assumed to occur at the crack site.
6. Load cycles within each block of a spectrum are ordered from high to low. The load interaction effects are neglected.
7. Stresses at the edge of the slot in the liner model and at the edge of the slot in the flat plate fracture model are the same. That is, the effects of curvature are negligible.
8. The curved plate model subjected to remote tensile loading responds locally similar to the model subjected to remote dynamic loading.
9. All remote membrane and bending loading cases yield the same value of K_T at the edge of the slot. The value of K_T for flat and curved plates subjected to the same remote loading is the same.
10. The transfer ratio does not change as the crack grows.
11. Load ratio effects can be neglected; crack growth rate behavior is obtained from R = 0.9 data. (This is discussed in more detail later in this section).
12. Small crack effects are negligible for the crack lengths considered.
13. It is assumed that the initial crack size is detectable.
14. Cracks initiate as quarter-circle corner cracks and grow as quarter-circle corner cracks until the crack depth reaches the flowliner thickness. Subsequently, cracks grow like part-elliptic through cracks. The part-elliptic through cracks can be approximated to through cracks with straight crack fronts.
15. The transition from a corner crack to a through crack is instantaneous.
16. The stress-intensity factors for quarter-circle corner cracks (with crack-depth equal to crack-length) can be obtained using Newman-Raju equations with Zhao modifications.

17. Crack growth is governed by Mode I deformations. Mode II and Mode III contributions can be neglected.
18. Failure is assumed to occur when the ligament between the slots is completely cracked (i.e., c = 0.75 in.). The number of cycles to crack the ligament between slots is nearly the same as the number of cycles required to grow the crack from its initial size to a length of 0.6 in.

Loading Spectra used in the Fracture Mechanics Analysis:

Using the BTA/GTA strain gage database and a rainflow counting procedure, the NESC developed three spectra. The development of these loading spectra was previously described in Section 7.2. In this section, these spectra will be referred to as the *NESC Spectrum-1, NESC Spectrum-2,* and *NESC Spectrum-3*. NESC Spectrum-1 was developed from the Boeing loading history as described in Section 7.2.1. Two versions have been used in the fracture mechanics analysis. One version is the original Boeing spectra with only a bending transfer ratio and the second version, referred to as the NESC Spectrum-1, uses the rainflow cycle counting method and separates the transfer ratios into membrane and bending components. NESC Spectrum-2 and Spectrum-3 were developed by the NESC for a nominal flight (see Section 7.2.2, to compare to the original Boeing spectra). Spectra-2 and –3 also use the rainflow cycle counting method and separate the transfer ratios into membrane and bending components. The three spectra are qualitatively compared in the plots provided in Figure 7.3-1 (a) through (d). In these figures, the alternating components of the membrane and bending stress for the upstream and downstream flowliners are plotted as a function of the mission time.

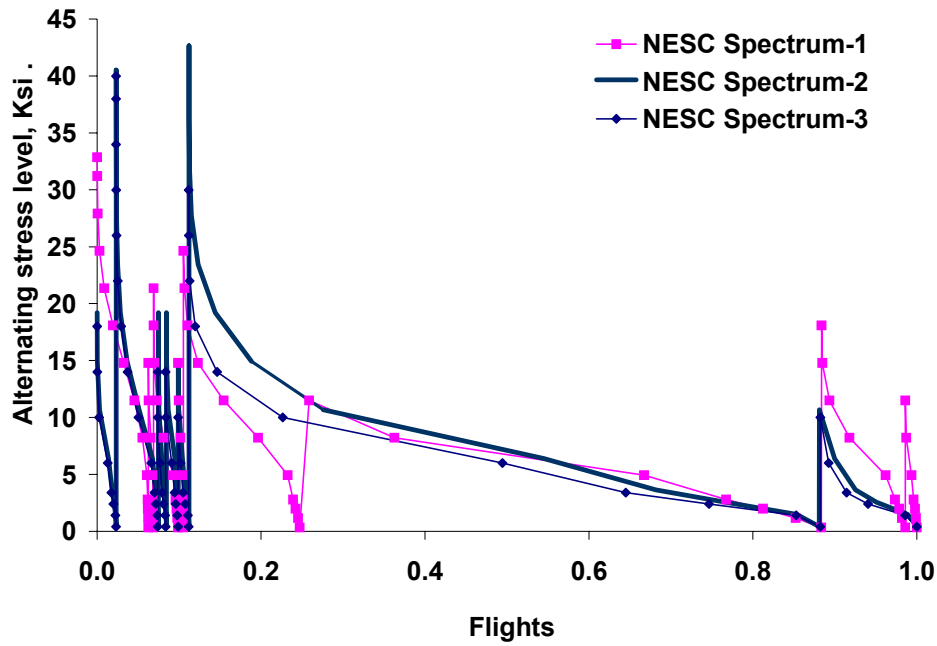

(a) Upstream Membrane

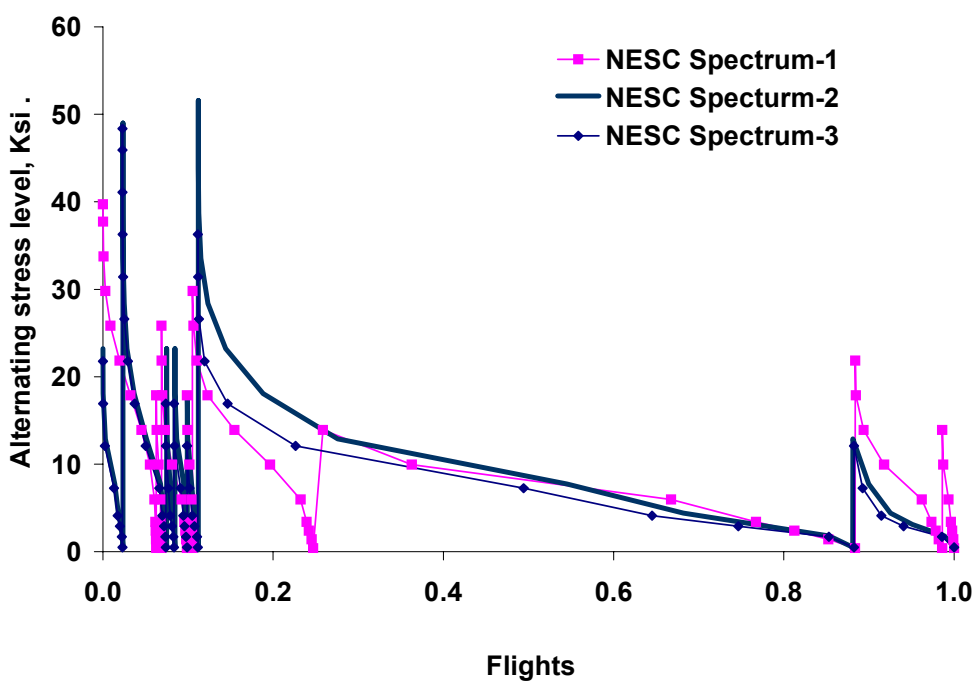

(b) Upstream Bending

Figure 7.3-1. (a and b) Comparison of NESC Spectra 1, 2, and 3

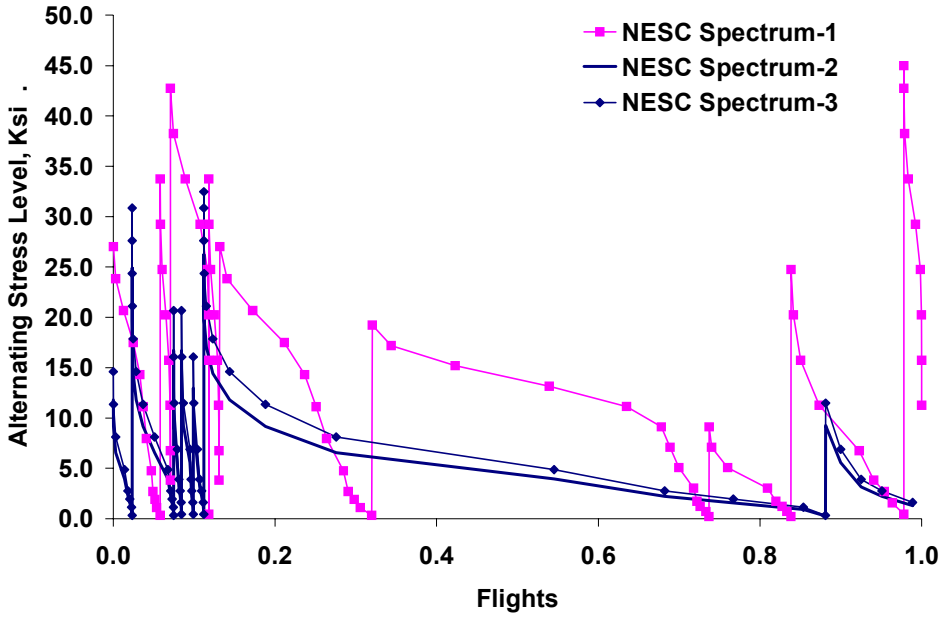

(c) Downstream Membrane

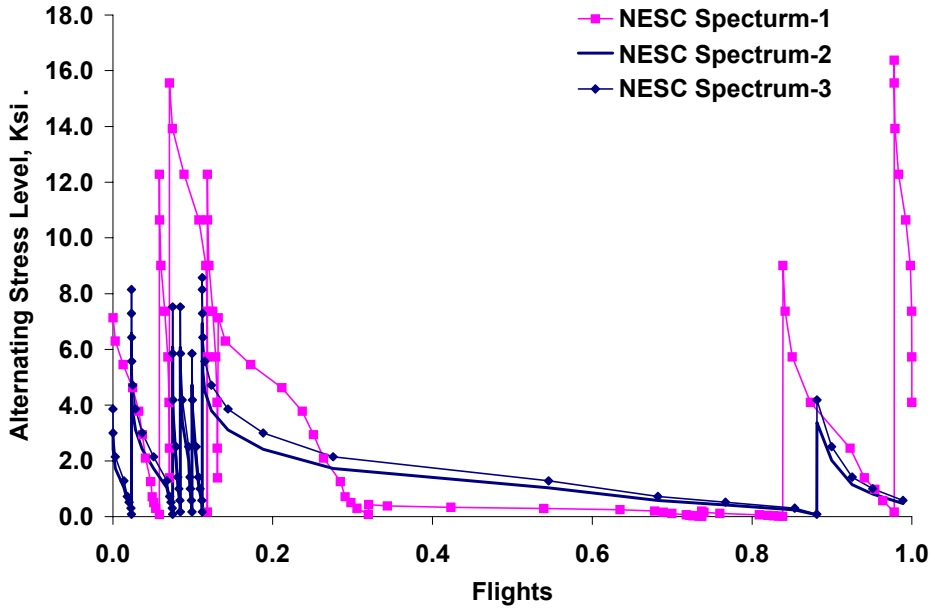

(d) Downstream Bending

Figure 7.3-1. (c and d) Comparison of NESC Spectra 1, 2, and 3

Crack Configuration Models

The only complete physical evidence of the crack shape is a crack from a MPTA downstream flowliner that was destructively broken open and characterized. The complete fractography of this crack is described in Appendix C.3. Figure 7.3-2 is a photomicrograph of this crack. The crack initiated at a scratch on the outer diameter (OD) of the slot near the location where the radius of the slot intersects the straight side. The beachmarks on the fracture surface (see Figure 7.3-2) indicate that the crack evolved as a near quarter circle corner crack, (i.e., with a/c = 1), then continued as an elliptic through-the-thickness crack.

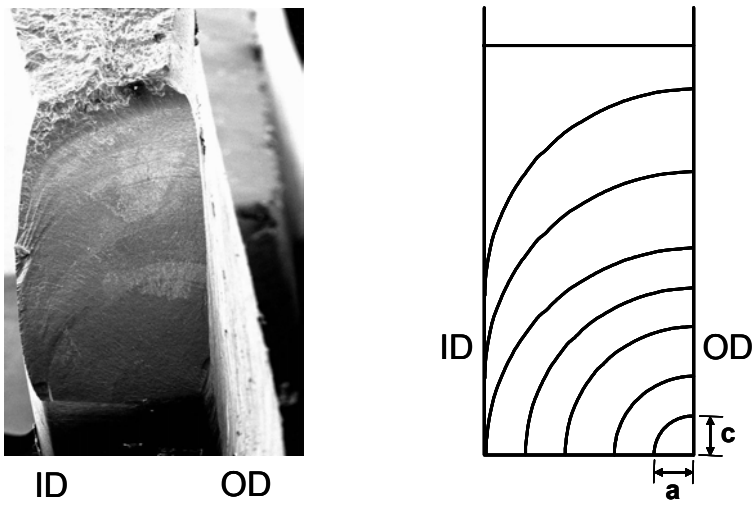

Figure 7.3-2. Photomicrograph of the MPTA Crack

Under pure bending loading, the inner diameter (ID) is under compressive loading and the crack shape will quickly evolve from a quarter-circle corner crack into a part-elliptic crack with a high aspect ratio. Under pure membrane loading, the crack will grow faster in the thickness and again will evolve into a non-uniform aspect ratio part-elliptic crack. The actual crack shape depends on the amount of membrane and bending components in the loading. The MPTA article shows that the crack grew as a quarter-circle corner crack and grew like a part-elliptic through crack at about c= 0.075 in. The MPTA crack shapes thus strongly suggest the existence of membrane loading in addition to the bending loads.

Three crack configurations are considered (Crack Configuration-1, Crack Configuration-2, and Crack Configuration-3), and are presented in Figures 7.3-3 through 7.3-5. Crack Configuration-

1 assumes an initial corner crack on the OD side with a = c = 0.005 in. as shown in Figure 7.3-3. The crack is assumed to grow like a quarter circle corner crack with a/c = 1 until it reaches the thickness and transition into a through-the-thickness crack with a crack length of c = 0.05 in. The crack is then assumed to grow like a through-the-thickness crack. This crack configuration is assumed in the NESC ITA analyses.

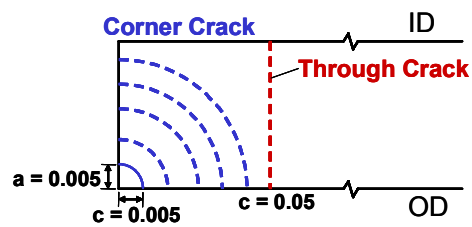

Figure 7.3-3. Crack Configuration-1

Crack Configuration-2 assumes an initial corner crack on the OD side with a = 0.045 in. and c = 0.02 in. as shown in Figure 7.3-4. This crack is then assumed to grow along the OD as an elliptic corner crack until the c length reaches 0.3 in. At c = 0.3 in., the crack is assumed to transition into a through crack and grow like a through-the-thickness crack. This crack configuration is used in the Marshall analyses [1].

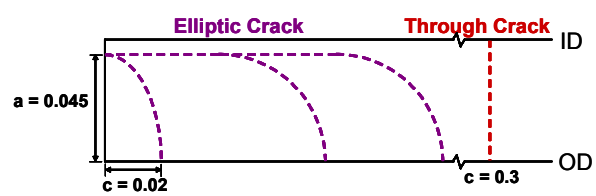

Figure 7.3-4. Crack Configuration-2

Crack Configuration-3 assumes an initial corner crack on the OD side with a = c = 0.005 in. as shown in Figure 7.3-5. The crack is assumed to grow like a quarter-circle corner crack with a/c = 1 until it reaches 90 percent of the thickness (i.e., until a = 0.045 in.). After this point, the crack is assumed to grow along the OD until a length of c = 0.3 in. At c = 0.3 in., the crack is assumed to transition into a through-the-thickness crack. This crack configuration was also used in the NESC ITA analyses.

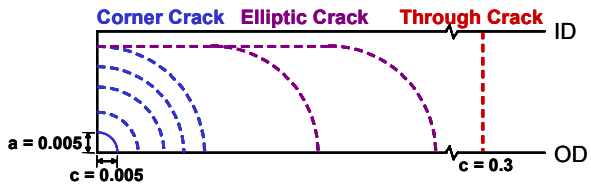

Figure 7.3-5. Crack Configuration-3

NASGRO Life Prediction Model

The life prediction code NASGRO Version 4.11 [2] is used for all crack growth predictions. The stress-intensity factors are entered using a 1-D data table (DT01) option. The user dimension, D, is 0.75 in. (the width between the slots). The spectra are entered as separate load cases for mean bending, alternating bending, and alternating membrane. The load cases are superimposed in NASGRO during the life calculations. All life calculations are performed using the NASGRO non-interaction model to ensure the most conservative life calculations. The non-interaction model performs linear accumulated damage crack growth and deactivates plasticity induced retardation models. Failure is defined as crack growth through the ligament. The difference in life between c = 0.6 in. and through the ligament is negligible.

Material Models (Fatigue crack growth rate data)

This section describes the material models used in the fracture mechanics analyses and the life calculations. The LH_2 flowliners operate at a temperature of -423° F. However, at the beginning of the ITA, Inconel 718 data only at LN_2 temperature of -320° F was available. Figure 7.3-6 is a plot of the Inconel crack growth rate vs. stress intensity factor (da/dN vs. ΔK) data at LN_2 (-320° F) and the NASGRO equation constants [2]. Personnel at NASA MSFC completed FCG testing of Inconel 718 at -423° F using a liquid helium testing process [3]. Figure 7.3-7 is a plot of the Inconel da/dN vs. ΔK data at -423° F and the NASGRO equation constants. The -423° F crack growth rate behavior is less severe than the -320° F data. The intrinsic threshold of the -423° F data (ΔK_{th} = 7 ksi $\sqrt{\text{in.}}$) is more than twice that of the original -320° F data (ΔK_{th} = 3 ksi $\sqrt{\text{in.}}$). The threshold shift will significantly increase the predicted life calculations by reducing the number of above-threshold (damaging) load cycles and reducing the amount of damage caused by the cycles that are above threshold. All life calculations were performed using IN 718 data at -320° F and at -423° F.

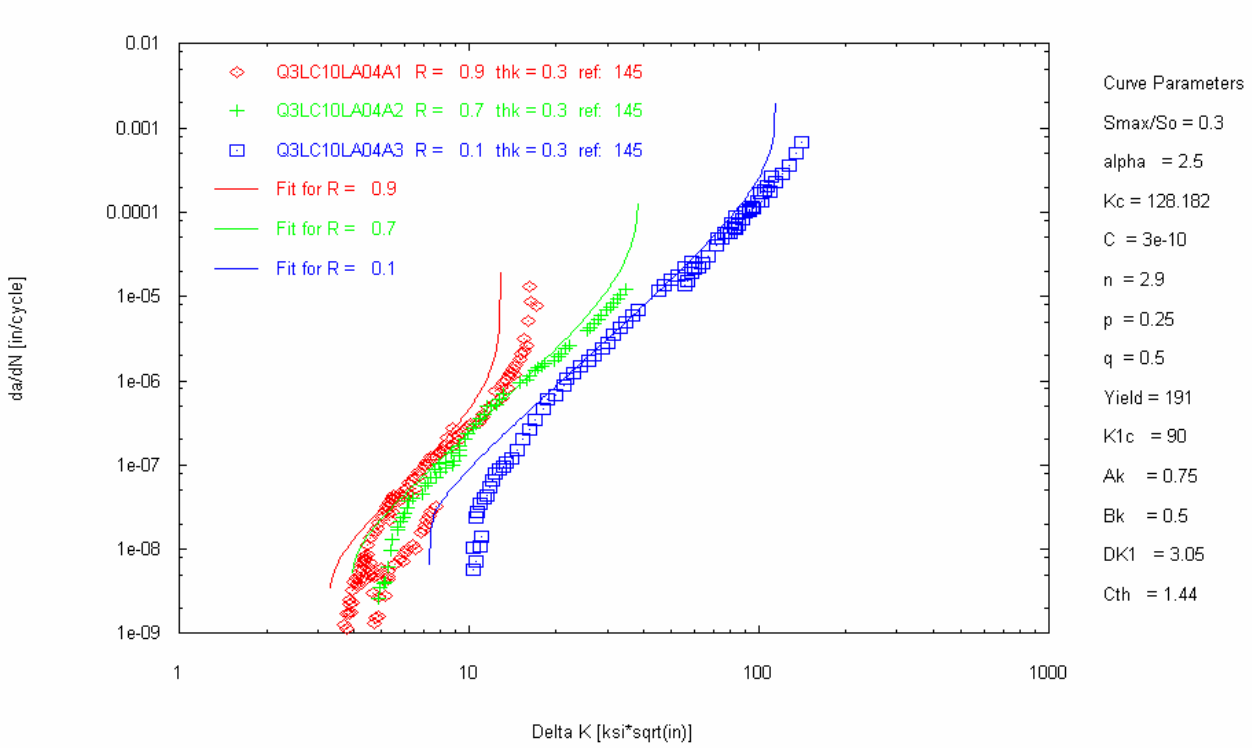

Figure 7.3-6. Inconel 718 da/dN vs. ΔK data at LN_2 (-320° F), Baseline Material Model

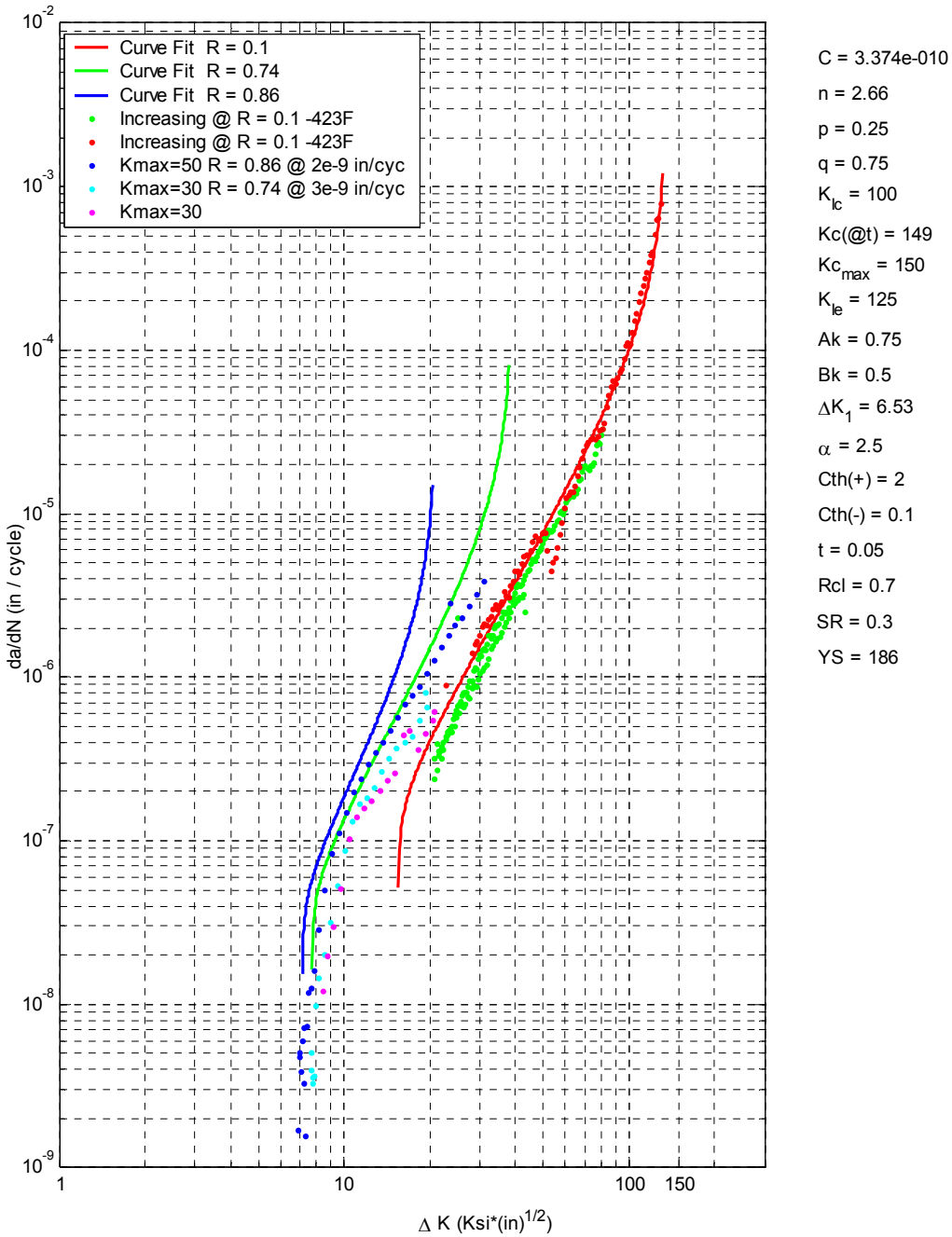

Figure 7.3-7. Inconel 718 da/dN vs. ΔK data at (-423° F)

Results and Discussion

Results are presented for the circumferential cracks at location B. Based on the physical evidence from the crack in the MPTA, Crack configuration-1 (see Figure 7.3-3) is chosen for the crack growth calculations. When the residual stresses are combined with the dynamics induced loading, the net stress at the ID side is always compressive. However, the MPTA article shows that the crack grew as a quarter-circle corner crack (with a/c = 1) and grew like a part-elliptic through crack at about c = 0.075 in. The MPTA crack shapes thus strongly suggest the existence of membrane loading in addition to the bending loads. With all the evidence that is available, the conservative choice for the crack configuration is Crack configuration-1 and hence is chosen in the present analysis.

Results for the Upstream Flowliner using the original Boeing Spectrum (the baseline)

The upstream liner was analyzed first for bending only, using the -320° F (Baseline) material model. First, the life calculations were performed using the Boeing loading spectrum and an initial crack length of 0.005 in., Crack configuration-1, and 70 Ksi mean stress. The calculated crack length-cycles curve for this configuration is presented in Figure 7.3-8. From this curve, the life of the flowliner was calculated using Boeing's assumptions (with the final crack length of 0.6 in. and a NDE threshold of 0.075 in. [4]) to be 0.8 missions. These calculations agree exactly with those in reference 4. While this type of life calculation is standard in damage tolerance analyses where the loading spectrum is repeated several times (like in a typical aircraft wing spectra), there appears to be no justification for evaluating the life of the liner in this fashion for a severe loading spectrum like the present Boeing spectrum. The crack length-cycle calculations were repeated assuming an initial crack length of 0.075 in., and the results are presented in Figure 7.3-9. The life is significantly lower, about 0.2 missions.

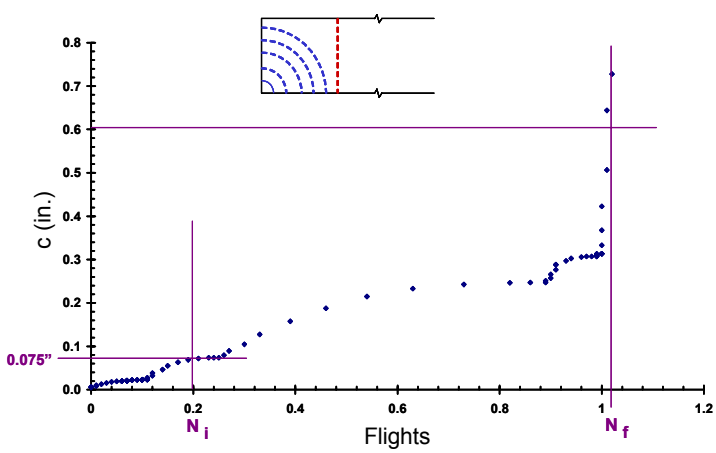

Figure 7.3-8. Crack Length – Cycles Curve vs. Flights for the Upstream Liners (Boeing Loading Spectrum, 70 ksi mean stress, with c_i = 0.005 in.)

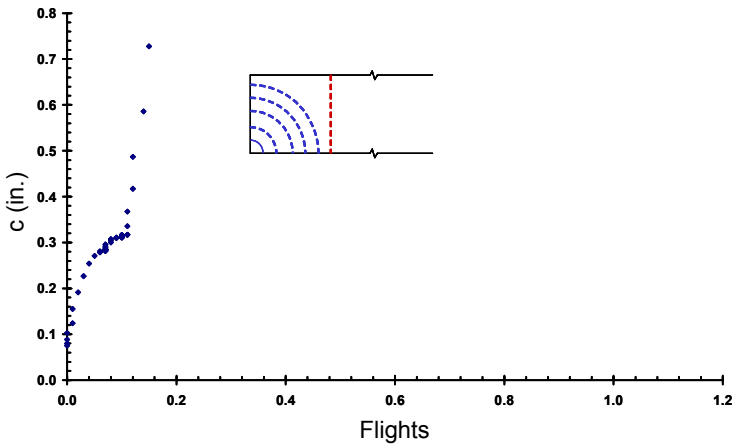

Figure 7.3-9. Crack Length – Cycles Curve vs. Flights for the Upstream Liners with c_i = 0.075 in.

The calculations were repeated with the Marshall-developed spectrum, Crack configuration-2, and 70 ksi mean stress. A life of 0.3 missions was computed and the results agree exactly with the calculations made by Rayburn [1]. In summary, the present analyses have reproduced both the Boeing and Marshall results with their respective loading spectra and assumptions.

Results of the Sensitivity Studies:

Life predictions were made using three different initial crack lengths (c_i = 0.075, 0.02, and 0.005 in.), the Boeing loading spectrum (bending loading), and the three NESC spectra. The effects of various parameters on the life of the upstream liner were studied for these three crack lengths. Throughout this report, the calculated lives are reported to two significant figures and are for comparison purposes only. The truncated integer part of the life number should be used.

Effect of Mean Stress: The first parameter studied is the effect of mean stress. Three mean stress values of 70, 50, and 30 ksi were considered, as shown in Table 7.3-1. The table shows that there was marginal effect as the mean stress was reduced from 70 ksi to 50 ksi and a significant improvement in life as the mean stress was reduced from 50 to 30 ksi.

Table 7.3-1. Life of the upstream liner: Boeing Loading Spectrum, Baseline material model, Crack configuration-3

Initial crack length, in. in.	Mean Stress, ksi		
	70 ksi Mean Stress	50 ksi Mean Stress	30 ksi Mean Stress
0.075	1.0	1.3	3.0
0.020	1.2	2.0	4.0
0.005	1.9	2.3	5.1

Effect of Material Models: The effect of material models on the life of the flowliner was considered. Table 7.3-2 presents the calculated life of the flowliner for the three material models considered. As seen from this table, the baseline material model predicts longer life than the Intermediate and Conservative models. As expected, the Conservative material gives the shortest lives because the ΔK threshold was lowest for this model. As mentioned previously, when the loads are well characterized, the baseline model produces unconservative results and hence hereafter, the intermediate material model is used.

Table 7.3-2. Life of the upstream liner: Boeing Loading Spectrum, 70 ksi mean stress, Crack configuration-3

Initial Crack Length, in. in.	Material Models		
	Baseline	Intermediate	Conservative
0.075	1.0	1.0	0.4
0.020	1.2	1.0	1.0
0.005	1.9	1.1	1.1

Effect of Loading Spectra: Next the NESC Spectrum-1 was used in the life calculations. Table 7.3-3 compares the results of the NESC Spectrum-1 with the Boeing spectrum. Note that the Boeing spectrum results were obtained with Crack configuration-3, while the NESC Spectrum results were obtained with Crack configuration-1. Also, note that the Boeing spectrum is based on the Rayleigh distribution while the NESC spectra are based on the rainflow counting procedures. Both calculations use 70 ksi mean stress and intermediate material models with LN_2 data.

Table 7.3-3. Comparison of calculated life with Boeing and NESC Spectra: Intermediate material model, 70 ksi mean stress

Initial crack length, in.	Boeing Spectrum	NESC Spectrum-1
0.075	1.0	0.9
0.020	1.0	1.1
0.005	1.1	2.0

As seen from this table, the NESC spectrum gave a longer life for an initial crack length of 0.005 in., while the lives were nearly the same (barely one mission) for the two longer initial crack lengths. Thus, the prediction of residual life is highly sensitive to small changes in peak stresses in the loading spectrum. Figure 7.3-10 presents the amount of damage in each of the loading blocks for the first flight of the spectrum for the 0.005 in. initial crack length, NESC Spectrum-1 case in Table 7.3-3. The highest damage was in block 5 followed by blocks 6 and 1. Most of the damage was caused in blocks 1, 5, 6, and 7; the contributions from the remaining blocks were insignificant.

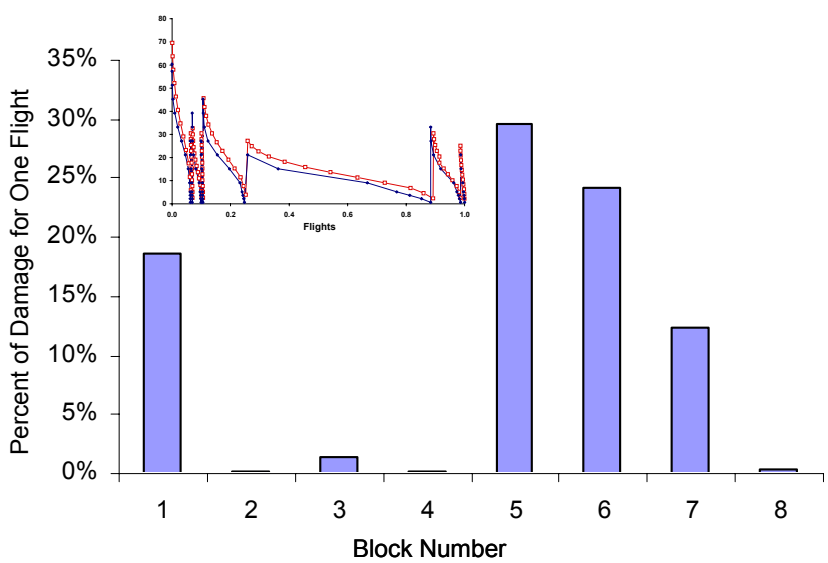

Figure 7.3-10. Damage Plot with Boeing and for NESC Spectra 1: Intermediate material model, 70 ksi mean stress

<u>Effect of LN_2 (-320° F) vs. LHe data (-423° F)</u>: The upstream liner case was analyzed with both LN_2 and LHe data utilizing the NESC Spectrum-1, and the computed lives are compared in Table 7.3-4. The LHe showed a $(\Delta K)_{th}$ of 7 ksi-in.$^{0.5}$ a considerable improvement from the LN_2

data threshold of about 3.5 ksi-in.$^{0.5}$. As expected, the life increased significantly when the LHe data was used and can be attributed to the increase in the $(\Delta K)_{th}$ with the LHe data.

Table 7.3-4. Calculated life for upstream liner; NESC Spectrum-1, Intermediate material Model, 70 ksi mean stress

Initial crack length, in.	Crack Growth Data	
	Crack Growth Data LN_2 (-320° F)	Crack Growth Data LHe (-423° F)
0.075	0.9	2.0
0.020	1.1	3.9
0.005	2.0	7.0

Summary of Results for the Upstream and Downstream Flowliners

Table 7.3-5 summarizes the results from all sensitivity studies discussed above for the upstream and downstream. It should be noted that the evidence is conclusive that both the upstream and downstream flowliners were excited by complex modes that include both membrane and bending loads. An initial crack length of 0.005 in. was also included in Tables 7.3-1 to 7.3-4 to study the effect of reducing the initial crack size. However, this crack size could be below the long crack threshold and may require a small crack analysis methodology. Therefore, the results summarized in Table 7.3-5 only include the longer crack lengths where small crack effects are not an issue. (See Appendices D.3.1 and D.3.2 for further discussion of small crack methodology).

Table 7.3-5. Summary of Life Calculations for Circumferential Crack B*
(Based on the transfer ratio approximation method)

Upstream Liner

	NESC Spectrum-1 (Boeing Loading History			NESC Spectrum-2 (Gage D47)	NESC Spectrum-3 (Gage D95)
	-320° F	-423° F	-423° F	-423° F	-423° F
Initial Crack Length, in	Bending	Bending	Bending + Membrane	Bending + Membrane	Bending + Membrane
0.075	0.9	2.0	0.1	0.0	0.2
0.02	1.1	3.9	0.3	0.1	1.0

Downstream Liner

	NESC Spectrum-1 (Boeing Loading History			NESC Spectrum-2 (Gage D47)	NESC Spectrum-3 (Gage D95)
	-320° F	-423° F	-423° F	-423° F	-423° F
Initial Crack Length, in	Bending	Bending	Bending + Membrane	Bending + Membrane	Bending + Membrane
0.075	0.6	2.0	0.1	5.2	2.2
0.02	1.1	3.6	0.2	10.0	4.2

The following observations/conclusions can be drawn from the results in Table 7.3-5:

1. The LHe data gives longer lives than the LN_2 data.
2. While longer life for the downstream liner is produced with NESC Spectra-2 and -3, the life of the upstream liner is significantly lower with Spectrum-2.
3. The lives of both the upstream and downstream flowliners are *significantly reduced* when both the membrane and bending loading are considered. Hence, *using only the bending loading rather than the combined membrane and bending loadings leads to erroneous and unconservative conclusions regarding lives*.
4. The calculated lives for the upstream flowliner shown in Table 7.3-5 are inconsistent with the fleet cracking data. However, the lives calculated for the downstream flowliner are somewhat consistent with the fleet cracking data. In general, smaller lives are predicted for the upstream liner compared to the downstream liner. The flight data shows five circumferential cracks (out of the total 11 cracks found), all in the downstream liner at location B. This suggests that the loading considered in the upstream flowliners is a conservative loading.

Alternate Modeling and Analysis Approach

Because the fatigue loading spectra are predominantly due to flow-induced vibration, the fracture mechanics analysis must be directly integrated with the structural dynamics analysis. In this section, a transfer ratio approach (an engineering approximation) is used to relate the mid-ligament strains measured in the BTA test to the crack initiation sites at the edge of the slots. A more rigorous alternate approach is to use a three-dimensional/shell finite element analysis that couples the crack growth kinetics directly to the structural dynamics. This approach, described in detail in the next section, does not require the use of transfer ratios.

Conclusions from the Sensitivity Study using the Transfer Ratio Approximation Method

Based on sensitivity analyses the following conclusions were reached.

1. Predicted values of residual fatigue life are sensitive to the small changes in the alternating component in the loading spectrum when bending loading is considered. For the same magnitude of the alternating stress component, the residual (mean bending) stress has to decrease to 30 ksi before significant change (by more than a factor of 2) in the residual life can be realized.

2. The degree of knowledge in the current loading spectra is insufficient to account for the crack closure effect. Hence, the use of intermediate material model with R=0.9 where $\Delta K = \Delta K_{Effective}$ is recommended.

3. The predicted life of the liners depends on the assumptions of the crack shape configuration. From the MPTA test article, fatigue cracks appear to initiate as corner cracks and grow nearly circular in shape to reach the thickness and grow subsequently as part through elliptic cracks. This crack growth configuration is conservatively modeled in the current analysis.

4. Inconel 718 exhibits an increase in ΔK threshold value with decreasing temperature. This effect is very beneficial to the life of the flowliner.

5. Decreasing the crack detection size will increase life. However, this effect is small for the severe loading spectra that are considered in this assessment. Decreasing the initial crack size below the current NDE limit of 0.075 in. to 0.02 in., or even to 0.005 in., does not yield significant increase in the life of the flowliners.

6. Membrane and bending components are operational in both upstream and downstream liners. The fracture mechanics analyses show that the predicted values of life are

significantly affected by the membrane component. Neglecting membrane component yields lives that are *highly unconservative*.

References

1. Rayburn, Jeff. "NESC Meeting Fracture Splinter Group Presentation at MSFC", PowerPoint Charts, NESC TIM, NASA Marshall Space Flight Center, February 26, 2001.

2. NASGRO Version 4.11 Manual, Southwest Research Institute, February 2004.

3. Wells, Doug. "Overview of Test Results for da/dN Evaluation for Inconel 718 at -423° F Supporting Flowliner Analytical Life Assessment", April 30, 2004.

4. Chart 26, Rigby & Warren, TIM, November 20, 2003.

7.4 Damage Tolerance (Fracture Mechanics) Analysis Methods and Results

Part II. Three-Dimensional Shell Analysis, Coupled Fracture Mechanics and Structural Dynamics

Approach for Stress-Intensity Factors

A transfer ratio approach for calculating stress-intensity factors is presented in Section 7.3. A more rigorous dynamics-based approach that is based on the full liner shell model is presented in this report. This approach will be hereinafter termed as the *shell-dynamics approach*. In this approach, a shell model of liner with a crack is used. Dynamic analysis of the shell is performed first. The representative mode of excitation in the shell is identified. For each particular shell mode, the strain energy release rates at the crack-tip are calculated. The stress-intensity factors are then evaluated from the strain energy release rates.

Shell-Dynamics Approach

In this approach, the stress-intensity factors at the crack-tip in the liner are directly evaluated using the deformed mode shapes that the liner experiences. Thus, this approach eliminates the transfer ratio and the associated assumptions and is more rigorous than the transfer ratio approach. The details of the shell-dynamics approach are described below.

A shell finite element model of the complete liner is developed first. A typical shell model is shown in Figure 7.4-1. Using this model, a modal analysis is performed to isolate the mode shapes for the upstream liner (C9ND mode shape) and the downstream liner (3ND, C4ND, and 5ND mode shapes).

Upstream Liner: Consider the upstream liner and the C9ND mode shape. The deformed shape of the upstream liner, based on the eigen-vector corresponding to this mode shape, is shown in Figure 7.4-2 along with a schematic of the locations of maximum mid-ligament and location B strain. Typical values of the normalized axial stress (i.e., Young's modulus (E) multiplied by the axial strain) at the mid-ligament locations are plotted in Figure 7.4-3 for all of the ligaments in the liner. As expected, the distribution shows a certain amount of cyclic symmetry for the C9ND mode shape. Similarly, the axial stresses at location B of all the slots are examined and the slot with the highest stress at location B is isolated. (There may be more than one slot with the same peak stress. In such a case, any one of those slots is chosen). In Figure 7.4-3, the slot with the highest axial stress is at $\varphi = 340°$. A circumferential crack of length (c) is introduced at this slot. A new shell finite element model with the crack is developed and re-analyzed.

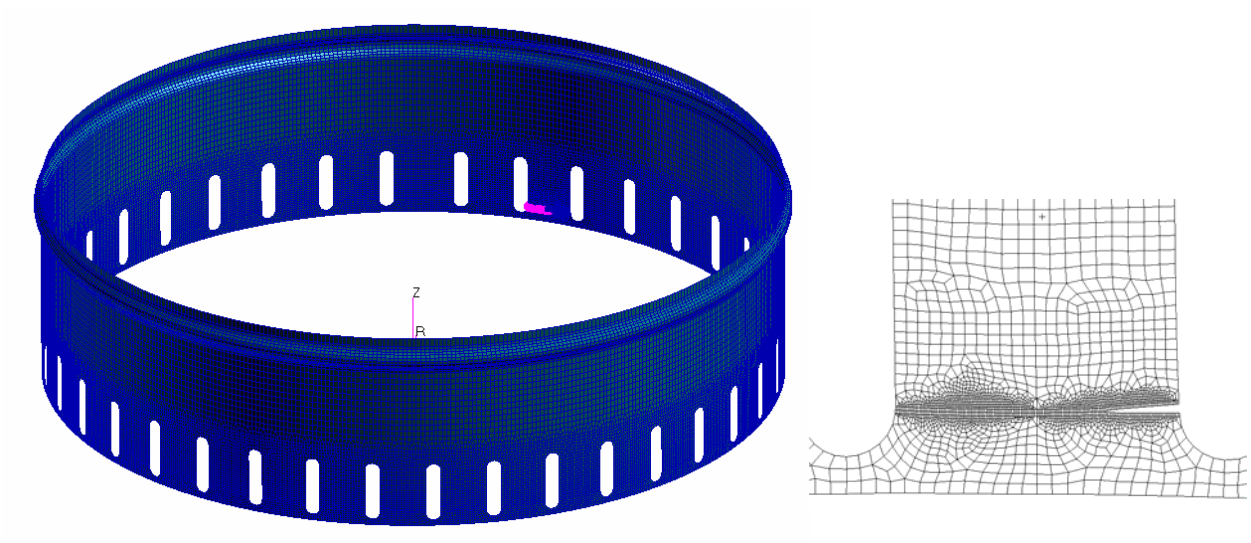

(a) Typical full liner model (b) Typical refined mesh near the crack

Figure 7.4-1. Typical Shell Finite Element Model

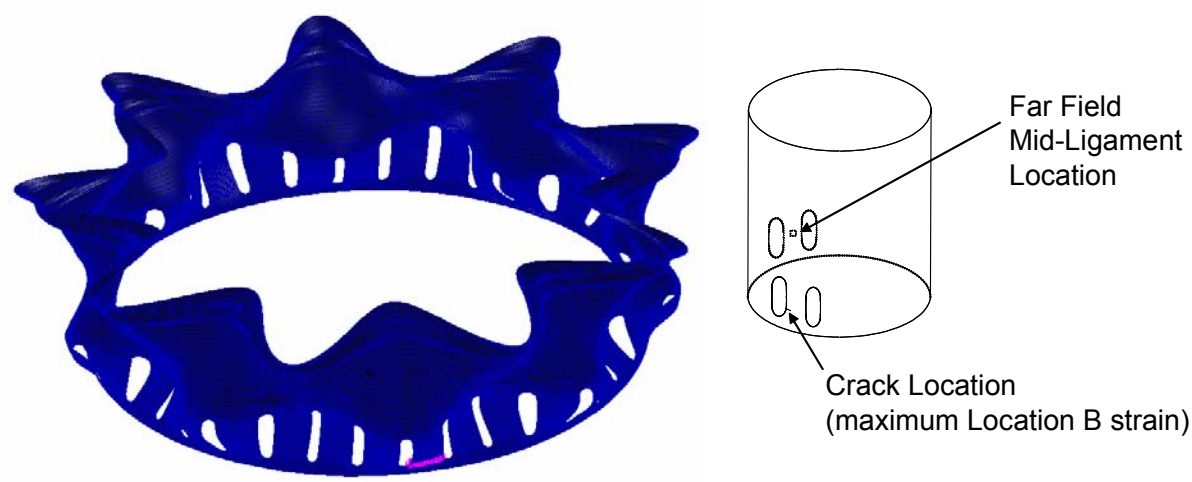

Figure 7.4-2. Far Field Ligament for Scaling the Eigen-Value Results

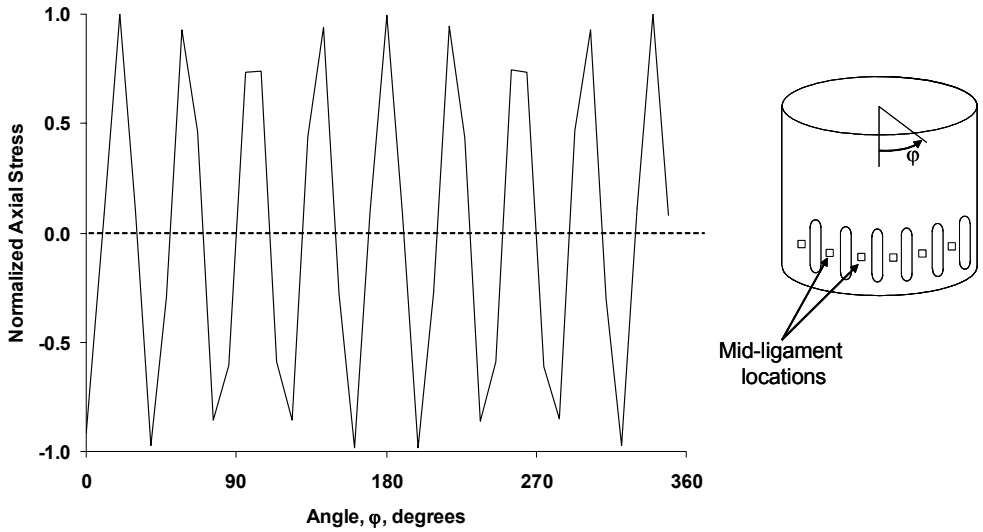

Figure 7.4-3. Typical Normalized Axial Mid-Ligament Stress for the C9ND Mode Shape

Again, the C9ND mode shape is isolated. The eigen-vector corresponding to this mode shape is scaled at the mid-ligament location to quantify the deformations in the shell. This scaling process requires a far field mid-ligament location to be identified. As mentioned above, the crack was inserted at the slot with the highest axial stress at location B ($\varphi = 340°$). Three mid-ligament locations had nearly the same peak value, so the scaling is based on the peak mid-ligament that is farthest ($\varphi = 180°$) from the slot with the crack. This location is used to scale all deformations and forces for each crack length analyzed.

Stress-intensity Factors

The stress-intensity factors are calculated from the strain energy release rates using virtual crack closure techniques as shown in Figure 7.4-4 [1, 2]. In this figure, F_x, F_y, and F_z are the respective forces at the crack-tip node in x, y, and z directions; M_x, M_y, and M_z are the respective moments about x-, y-, and z-directions; u_x, u_y, and u_z are the respective displacements at a node behind the crack-tip along the x-, y-, and z- directions; and θ_x, θ_y, and θ_z are the respective rotations at a node behind the crack about the x-, y-, and z- directions. B is the thickness of the shell and Δc is the length of the element behind the crack tip. The finite element models had a fine mesh in the crack region with same size of the elements behind and ahead of the crack tip (element size Δc = 0.005 in, as shown in Figure 7.4-4).

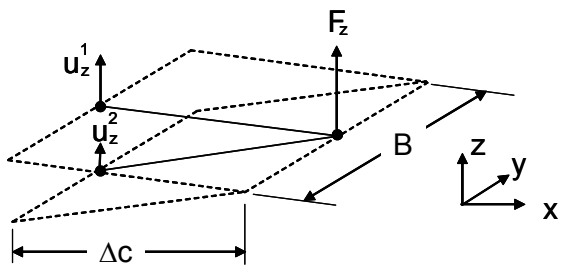

$$G_I = \frac{1}{2\,\Delta c\,B}\left[F_z\,(u_z^1 - u_z^2) + M_y(\theta_y^1 - \theta_y^2) + M_x(\theta_x^1 - \theta_x^2)\right]$$

$$G_{II} = \frac{1}{2\,\Delta c\,B}\left[F_x\,(u_x^1 - u_x^2)\right]$$

$$G_{III} = \frac{1}{2\,\Delta c\,B}\left[F_y\,(u_y^1 - u_y^2) + M_z(\theta_z^1 - \theta_z^2)\right]$$

Figure 7.4-4. Schematic showing crack tip coordinate system and energy release rate equations [2]

The stress-intensity factors are calculated from the energy release rates as shown in Equation 7.4-1, a-c, where E is Young's modulus.

$$K_I = \sqrt{EG_I} \qquad \text{(EQ. 7.4-1a)}$$

$$K_{II} = \sqrt{EG_{II}} \qquad \text{(EQ. 7.4-1b)}$$

$$K_{III} = \sqrt{EG_{III}} \qquad \text{(EQ. 7.4-1c)}$$

In addition, a total stress-intensity factor is calculated from the total energy release rate as shown in Equation 7.4-2.

$$K_{TOTAL} = \sqrt{EG_I + E\gamma\left[G_{II} + G_{III}\right]} \qquad \text{(EQ. 7.4-2)}$$

This approach (EQ. 7.4-2) to calculating an equivalent total stress-intensity factor based on the total energy release rate was proposed by Potyondy et. al. [3] for a shell analysis, and they suggest that a value of $\gamma = 1$ yields conservative K-values. Hence, $\gamma = 1$ is adopted here.

Figure 7.4-5 is a plot of stress-intensity factor versus crack length calculated for the upstream liner. For each crack length, the C9ND mode shape is isolated and the stress-intensity factors are calculated from the energy release rates. The values presented in this figure are scaled to a unit value of far field mid-ligament stress. For crack lengths in the range of $0 < c \leq 0.3$ in., Mode I is nearly constant and is dominant. The Mode III contributions increase with increasing crack length. For crack lengths $c > 0.3$ in., the Mode III component increases and is about equal to the Mode I component. The Mode II component is insignificant.

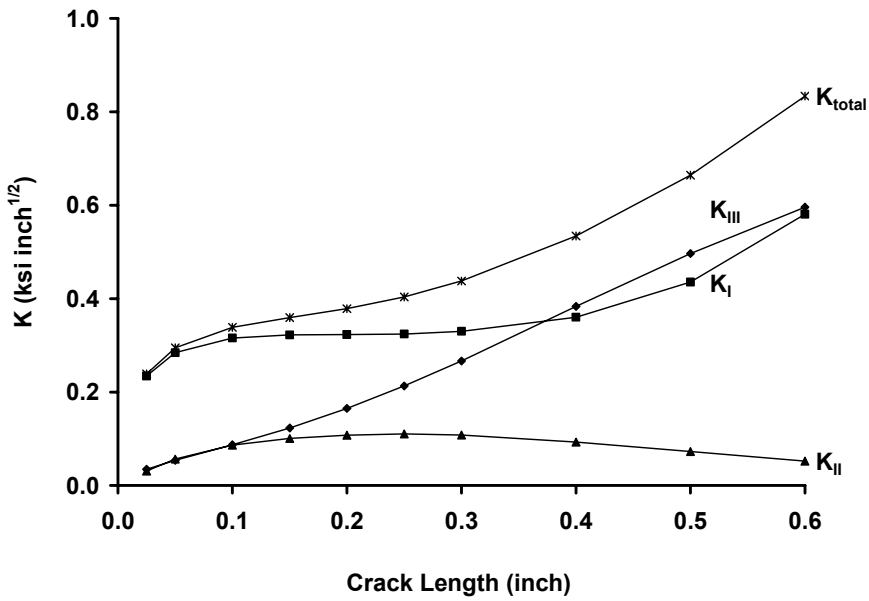

Figure 7.4-5. Stress-intensity Factors for the Shell-Dynamics Model for the C9ND mode

The stress-intensity factors from the shell-dynamic analysis (Figure 7.4-5) are compared in Figure 7.4-6 to those obtained using the transfer ratio approach. The shell-dynamics K_{total} curve is the same as in Figure 7.4-5, and the transfer ratio values are also computed using a mid-ligament stress of unity and use the transfer ratio values consistent with the updated shell-dynamics model. The stress-intensity factors from the shell-dynamic analyses are significantly lower than those obtained from the transfer ratio approach, suggesting that the transfer ratio approach is overly conservative. As expected, the values from the two approaches converge as the crack length decreases. The largest crack length considered in the shell-dynamic analysis for this comparison and for the life predictions was 0.3 inch because longer crack lengths exhibited a considerable Mode III component of the stress-intensity factor. The material data used to characterize crack growth behavior was derived from Mode I crack growth rate tests and would not necessarily be appropriate for Mode III dominate crack growth. Most of the life is consumed while the crack is a corner crack (or short through-the-thickness crack) so stopping the life prediction at 0.3 inches is conservative, yet makes little difference to the overall life.

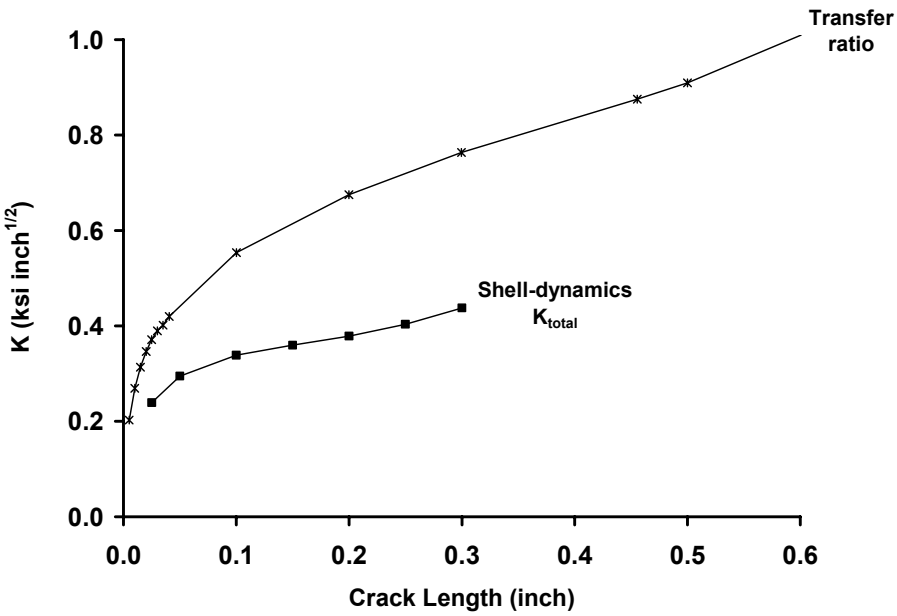

Figure 7.4-6. Comparison of Shell-Dynamics and Transfer Ratio Stress-intensity Factors for the C9ND Mode with Unit Stress Loading at the Far Field Mid-ligament

Both the transfer ratio and shell-dynamics approaches will converge to the same values as the crack size decreases. The smallest crack size considered for the shell-dynamics approach is 0.025 inch (filled square symbols in Figure 7.4-6). Thus, the shell-dynamics K_{total} stress-intensity factor was extrapolated to blend in with the transfer ratio curve at a crack length of 0.005 inch.

Several factors appear to be contributing to the difference in the stress-intensity factors in Figure 7.4-6. Recall that a flat and a cylindrical plate model (with the same curvature as the liner) with seven slots was analyzed and reported in Section 7.3. The plates were assumed to be fixed on y = 0 and have symmetric boundary conditions on x = $\pm$3.5 in. and along straight edges in the curved models. The plates were subjected to remote axial loading (see Appendix D.3.1, Figure D.3.1-11). The stress-intensity factors for various crack lengths from the two models are marginally different (less than one percent). This suggested that the effect of curvature of the shell is insignificant for remote tensile loading. A similar argument can also be made for remote bending loading. In the shell-dynamics approach, modal deformations (3 displacement and 3 rotations) at each node (of the FE model) of the shell are prescribed. **These deformations are significantly different from the deformations of a curved cylindrical shell subjected to remote tension and bending loads**. This prescription of modal deformations at each node is likely stiffening the shell and this stiffening is not reflected in the models used with the transfer ratio approach. The stiffening of the shell is reflected in lowering of the stress-intensity factors.

Downstream Liner: The analysis presented in the foregoing for the upstream liner is repeated for the downstream liner. Recall that in the downstream liner there are three modes, 3ND, C4ND, and 5ND, that are active. The stress-intensity factors are calculated for various crack lengths using the shell-dynamics approach for the three modes and are presented in Figures 7.4-7 through 7.4-12. As in the upstream liner, the calculations are performed only up to a crack length of 0.3 in. In these figures, the contributions (K_I, K_{II}, and K_{III}) to the K_{total} are shown along with the stress-intensity factors obtained using the transfer ratio. For all three modes, the shell-dynamics approach yielded stress-intensity factors lower than those calculated using the transfer ratio approach. The difference between the shell-dynamics approach and the transfer ratio approach is more pronounced for the 3ND and C4ND modes than for the 5ND mode.

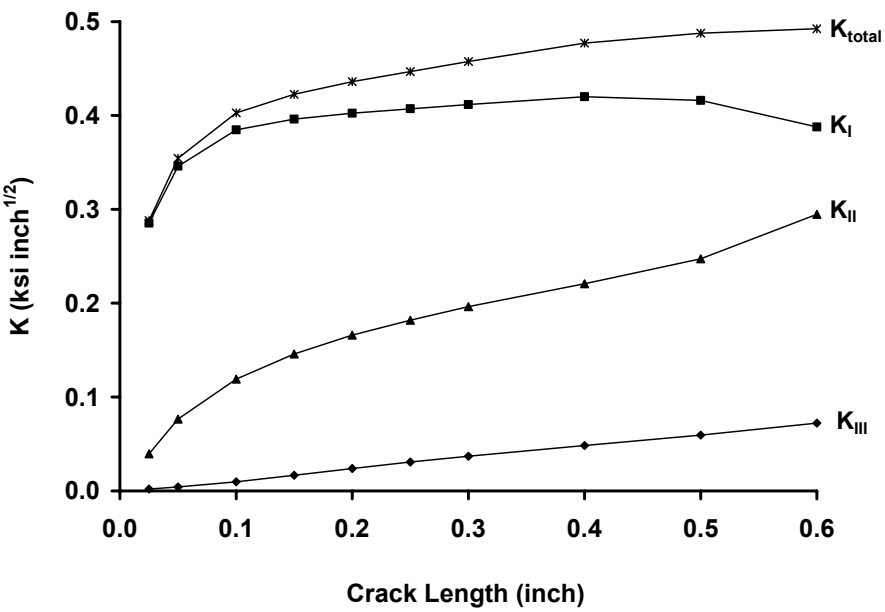

Figure 7.4-7. Stress-intensity Factors for the Shell-Dynamics Model for the 3ND Mode

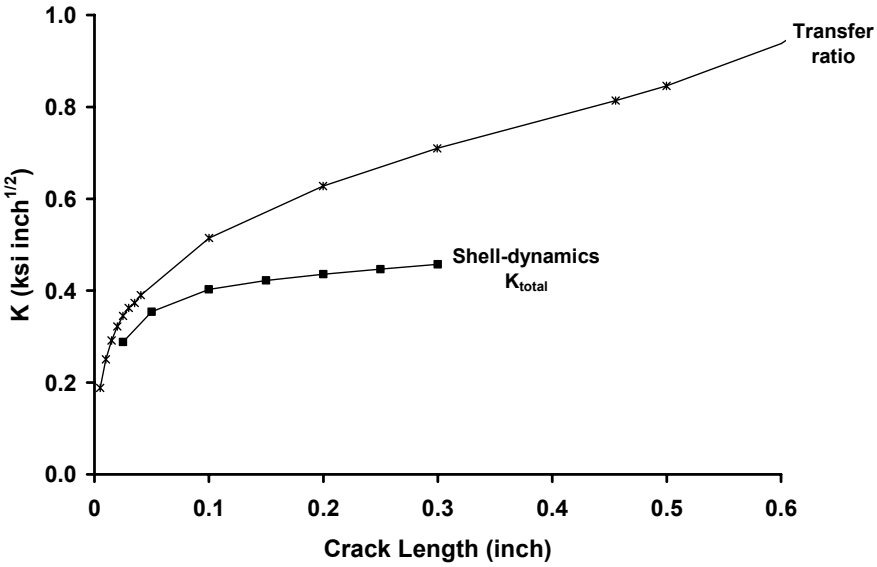

Figure 7.4-8. Comparison of Shell-Dynamics and Transfer Ratio Stress-intensity Factors for the 3ND Mode with Unit Stress Loading at the Far Field Mid-ligament

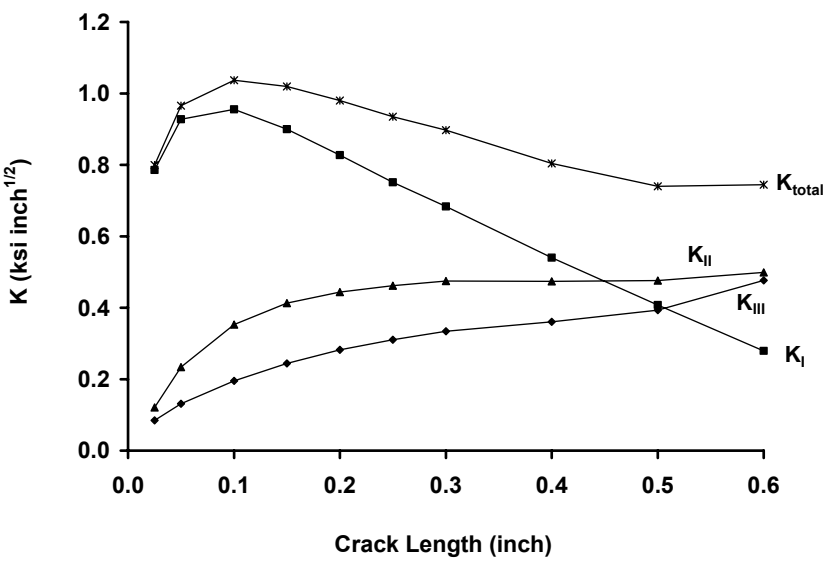

Figure 7.4-9. Stress-intensity Factors for the Shell-Dynamics Model for the C4ND Mode

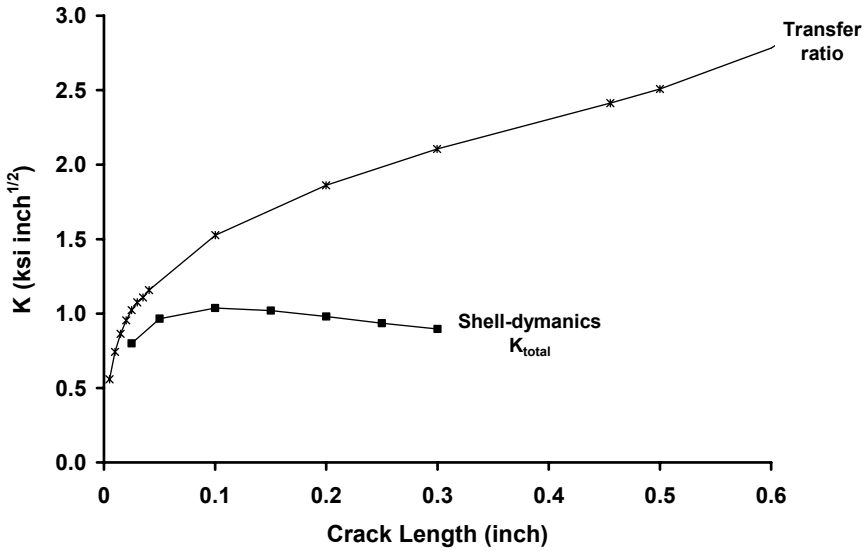

Figure 7.4-10. Comparison of Shell-Dynamics and Transfer Ratio Stress-intensity Factors for the C4ND Mode with Unit Stress Loading at the Far Field Mid-ligament

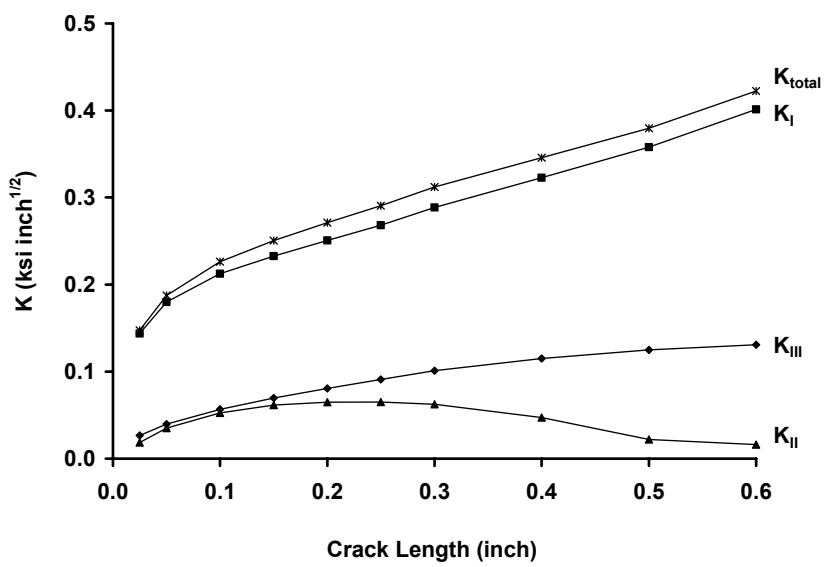

Figure 7.4-11. Stress-intensity Factors for the Shell-Dynamics Model for the 5ND mode

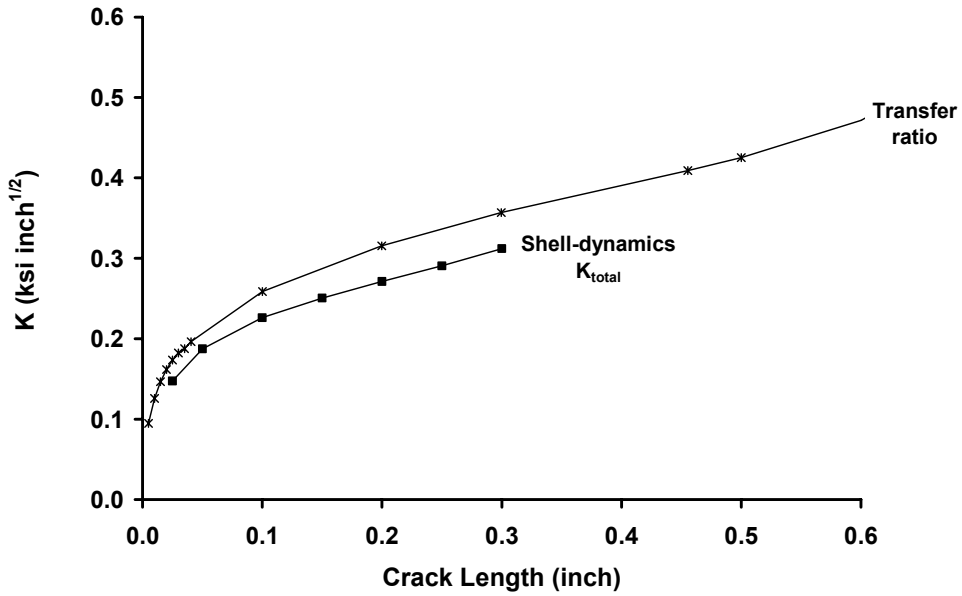

Figure 7.4-12. Comparison of Shell-Dynamics and Transfer Ratio Stress-intensity Factors for the 5ND Mode with Unit Stress Loading at the Far Field Mid-ligament

Results

The shell-dynamics K_{total} stress-intensity factor was input into NASGRO. In addition, the loading spectra were recalculated as mid-ligament stresses rather than crack site stresses. These new results were then used to calculate fatigue lives for the both liners at location B. Tables 7.4-1 and 7.4-2 summarize the fatigue crack growth analyses run using the shell-dynamics stress-intensity factors. All of results use the intermediate material model at -423° F. The transfer ratio results from Appendix D.3.1 are included in the tables for comparison. As expected, significant improvement in lives is obtained with the new shell-dynamics approach. Note that the smallest crack size considered is c = 0.02 inch.

Table 7.4-1. Predicted Number of Flights Using the Shell-Dynamics Stress-Intensity Factors for the Upstream Liner at Location B

	NESC Spectrum-1 (Boeing Loading History)		NESC Spectrum-2 (NESC Loading History)		NESC Spectrum-3 (NESC Loading History)	
c_i (inch)	Transfer Factor Approach (flights)	Shell-dynamics (flights)	Transfer Factor Approach (flights)	Shell-dynamics (flights)	Transfer Factor Approach (flights)	Shell-dynamics (flights)
0.075	0.1	21	0.0	11	0.2	35
0.020	0.3	39	0.1	21	1	72

*Intermediate Material Model at -423° F

Table 7.4-2. Predicted Number of Flights Using the Shell-Dynamics Stress-Intensity Factors for the Downstream Liner at Location B

	NESC Spectrum-1 (Boeing Loading History)		NESC Spectrum-2 (NESC Loading History)		NESC Spectrum-3 (NESC Loading History)	
c_i (inch)	Transfer Factor Approach (flights)	Shell-dynamics (flights)	Transfer Factor Approach (flights)	Shell-dynamics (flights)	Transfer Factor Approach (flights)	Shell-dynamics (flights)
0.075	0.1	0.2	5	10	2	4
0.020	0.2	1	10	27	4	10

*Intermediate Material Model at -423° F

References

[1] Rybicki, E.F. and Kanninen, M.F. *"A Finite Element Calculation of Stress Intensity Factors by a Modified Crack Closure Integral"*, Eng. Fracture Mech., Vol. 9, pp. 931-938, 1977.

[2] Wang, J.T., Raju, I.S., Davila, G., and Sleight, D. *"Computation of Strain Energy Release Rates for Skin-Stiffener Debonds Modeled with Plate Elements"*, 34th AIAA SDM Conference, La Jolla, California (April 19-21, 1993).

[3] Potyondy, D. Wawrzynek, P., and Ingraffea, A. *"Discrete Crack Growth Analysis Methodology for Through Cracks in Pressurized Fuselage Structures"*, International Journal for Numerical Methods in Engineering, Vol. 38, pp. 1611-1633, 1995.

[4] Elliot, K., Appendix D.2.1.

7.5 Fatigue Life to Crack Initiation Analysis Methods and Results

Crack Initiation Life Model

A Monte Carlo simulation of the crack initiation behavior in the space shuttle fuel feedline, gimbal joint, flowliners has been devised. It is assumed that fluid/structure interactions subject the liners to high cycle fatigue loading. It is also assumed that each slot is equally likely to experience the maximum strain amplitude from the given vibration mode present in each flight regime (modes "clock" around).

To predict the life of crack initiation fatigue damage is accumulated according to a linear damage rule (LDR), often referred to as Miner's rule. The LDR is based on assumption that there is no interaction between damage accumulated at various load levels and therefore no effect of loading history on subsequent damage accumulation. The form of the LDR is shown in Eq. 7.5-1:

$$D = \frac{n_1}{N_1} + \frac{n_2}{N_2} + \Lambda \frac{n_m}{N_m} \qquad \text{Eq. (7.5-1)}$$

where n_x is the number of cycles imposed at a given load level and N_x is the expected fatigue life at the given load level with the cycles counted and binned into arbitrary load levels. When the accumulated damage, D, reaches 1.0, the crack is said to have initiated. Crack initiation is typically defined as a detectable crack on the order of 0.02 to 0.03 inches. Potentially more accurate damage interaction rules (such as the damage curve approach) require accurate knowledge of the loading history and data derived from sequential loading experiments, neither of which exists for this application and material.

In order to use fatigue data, which is often performed under fully reversed ($R = \sigma_{min}/\sigma_{max} = -1$) uniaxial loading, to predict fatigue damage caused by an alternating load with a different mean stress, a correction to the alternating stress is typically applied. Several mean stress correction approaches (Goodman, Soderberg, Morrow and Gerber) were examined in the process of developing the fatigue life tools used. The Soderberg approach was selected because it seemed to fit the limited available data, and it provided the most conservative life predictions for high mean stress conditions. Equation 7.5-2 is the form for the Soderberg mean stress correction:

$$\sigma_{So} = \frac{\sigma_{alt}}{\left[1 - \frac{\sigma_{mean}}{\sigma_y}\right]} \qquad \text{Eq. (7.5-2)}$$

The yield stress, σ_y, of IN178 at -423° F is 180 ksi.

Results

Deterministic and probabilistic calculations of the crack initiation life of the fuel feedline, gimbal joint, and flowliners were performed. Referring to the results summarized in Table 7.5-1, deterministic calculations for circumferential crack locations, using the BTA/GTA derived loading spectra provided by Boeing (Section 7.2.1) at the time of this report, fewer than 10 missions to crack initiation were predicted using mean fatigue properties. Results are also presented in Table 7.5-1 for the two spectra generated by the NESC ITA Team.

Table 7.5-1. Results of Deterministic Crack Initiation Life Calculations for the Circumferential Crack Location

Spectra	Crack initiation life [missions]
NESC Spectrum-1 (Boeing) upstream	4
NESC Spectrum-2 (gage D47) upstream	10
NESC Spectrum-3 (gage D95) upstream	41
NESC Spectrum-1 (Boeing) downstream	8
NESC Spectrum-2 (gage B132) downstream	2817
NESC Spectrum-3 (gage B161) downstream	139

A probabilistic crack initiation simulation of the upstream and downstream flowliners using the NESC Spectrum-1 applied over 25 missions resulted in many more cracks than observed in the shuttle fleet (an average of 87 simulated cracks per upstream liner and 49 simulated cracks per downstream liner, where the IN718 liners had an average of less than one crack per liner). In order to approximate the distribution of cracks in the shuttle flowliners, the amplitudes of the stresses in the simulation must be significantly reduced. By applying scaling factors of 0.25 and 0.3 to the upstream and downstream Boeing spectra, the crack distributions shown in Figures 7.5-1 and 7.5-2 for the upstream and downstream flowliners, respectively, are calculated. This sizeable reduction in the overall loading spectra gives a more approximate level of cracking consistent with that observed in the fleet.

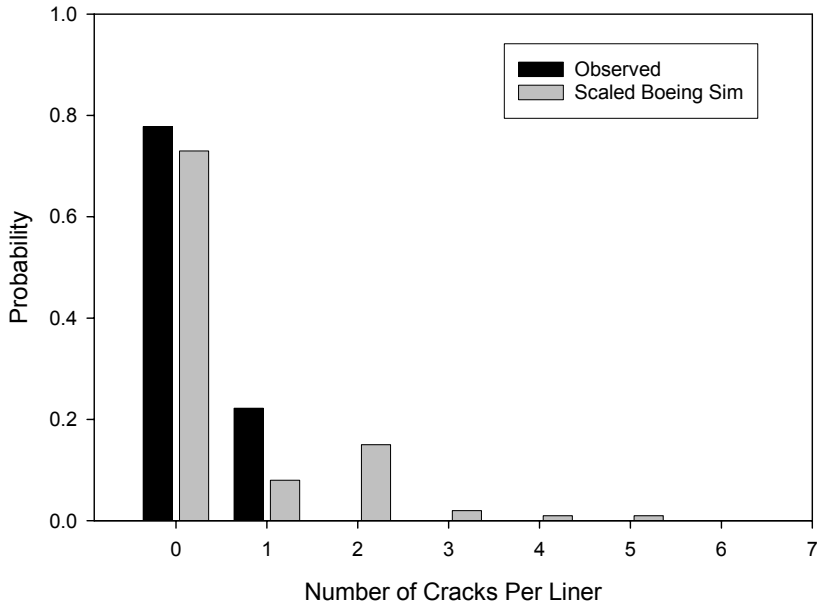

Figure 7.5-1. Comparison of the number of cracks per *upstream* IN718 flowliner in the fleet and the scaled Boeing spectra simulation

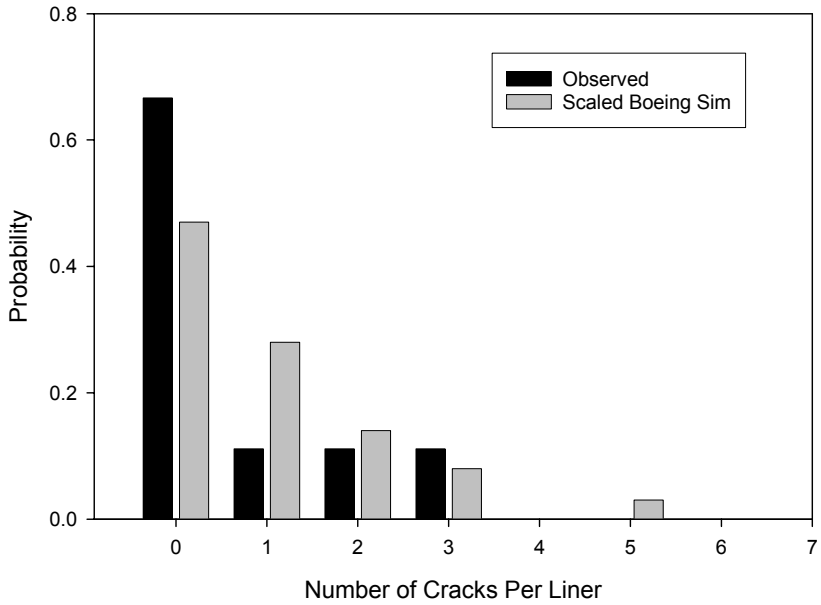

Figure 7.5-2. Comparison of the number of cracks per *downstream* IN718 flowliner in the fleet and the scaled Boeing spectra simulation

7.6 Edge Replication Examination Method

Background

Fracture mechanics based predictions have shown that flowliner high cycle fatigue cracking will propagate from extremely small surface cracks. To ensure acceptable damage tolerant behavior, life predictions will likely require the detection of extremely small surface cracks. Based on recent predictions, acceptable pre-existing crack size could be smaller than the crack detection threshold of traditional nondestructive examination methods (NDE). As a result of these findings, a feasibility study is being conducted to evaluate a non-traditional NDE method, the surface replica method, for detecting small surface fatigue cracks contained in the Orbiter main engine flowliners. The replica method is an established laboratory method that has been used by the fatigue and fracture community and for nearly three decades at NASA Langley Research Center for fatigue crack growth studies of micron sized surface cracks in aircraft structural alloys. Reported herein are initial findings that discuss the replica method resolution for surface cracks contained in polished Inconel 718 slots similar to that contained in Orbiter flowliners.

Procedure

Fatigue tests were conducted using notched Inconel 718 specimens shown in Figure 7.6-1. The notch reproduces the stress state of the flowliner slot under Mode I loading. The specimens were fabricated at MSFC; the notch was formed using a punching process similar to flowliner slot fabrication followed by a polishing process that was developed by MSFC. All fleet flowliners have been polished by the MSFC process. During the fatigue tests, replica inspections were conducted to detect the onset of fatigue crack nucleation. (Appendix D.5.2 provides a detailed description of the replication procedure). Figure 7.6-1(b) shows an acetate tape positioned in the specimen slot while replicating the slot surface. Acetate tape replicas were taken every 2000 to 3000 load cycle intervals; at which point, the fatigue test was stopped, the specimen was unloaded, and the edge replicas were taken. (To simulate replica inspection of the flowliner, zero-load was used to ensure the crack was fully closed as it would be during flowliner inspection).

Results

The series of SEM micrographs shown in Figure 7.6-2 demonstrates the resolution of the replica method for detecting small/short surface cracks contained in polished Inconel 718 slots. Shown are acetate tape replicas taken from the same test specimen slot after (a) 215,000, (b) 235,000, (c) 240,000, (d) 255,000, and (e) 270, 000 load cycles. The replicas reveal the change in surface crack length of the single fatigue crack contained in a polished test specimen slot. See Table 7.6-1. **These data (micrographs) demonstrate acetate tape replica method resolution for small surface cracks at zero-load.** Additional work is currently being conducted to demonstrate the feasibility of using acetate tape and a new replica material (Repliset®) for inspecting flowliner slots for small surface cracks.

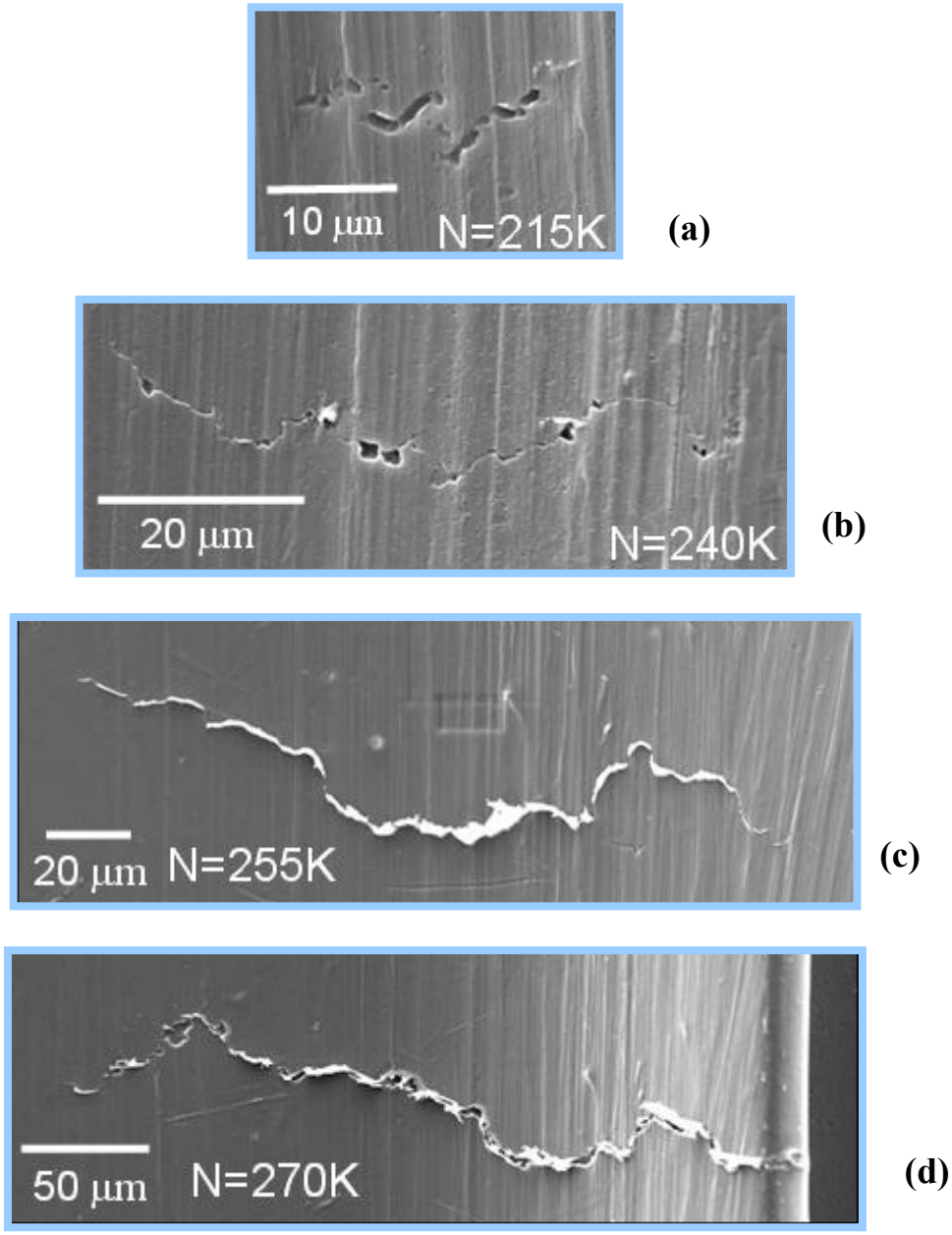

Figure 7.6-2. Shown are acetate tape SEM micrographs of the same surface crack at: (a) 215,000 load cycles, (b) 240,000 load cycles, (c) 255,000 load cycles, and (d) 270,000 load cycles

Table 7.6-1. Surface Crack Lengths (Replica Method)

Micrograph (Figure No.)	Fatigue Load Cycle (N)	Surface Crack Length* Inch (μm)
7.6-2a	215,000	2a = 0.0008 (21)
7.6-2b	240,000	2a = 0.0024 (60)
7.6-2c	255,000	2a = 0.0072 (183)
7.6-2d	270,000	C = 0.0110 (282)

*Refer to Figure 7.6-2 for surface crack notation

Discussion

The micrographs shown in Figure 7.6-2 reveal that the polished notch exhibits a surface more conducive to the surface replica method compared to the as-punched surface shown in Appendix D.5.2. The relatively smooth surface produced by the MSFC flowliner slot polishing method clearly exhibits shallow scratches that are normal to the fatigue crack plane and therefore does not interfere with fatigue surface crack detection. Figure 7.6-2 (a) shows that the replica method has the resolution to detect a fatigue crack having a surface dimension (2a) of ≤0.001 inches and is able to accurately track crack propagation as it evolves into a corner crack of surface dimension (Figure 7.6-2 (c)) approximately 0.011 inch (Figure 7.6-2 (d)). The replica base results for polished Inconel 718 slots shown in Table 7.6-1 demonstrate that the acetate tape method exhibits the resolution to detect fatigue cracks of surface dimension ≤0.001 inch.

Conclusions

1. The replica method exhibits the capability for detecting fatigue cracks of surface dimension ≤0.001 inches contained in polished notches having the same configuration as the Orbiter flowliner slots.

2. The MSFC flowliner polishing produces a smooth surface containing shallow scratches that are normal to the fatigue crack plane and therefore does not interfere with fatigue surface crack detection by the replica method.

7.7 Nondestructive Evaluation Methods for In-service Inspection

In the establishment of the Flowliner Independent Technical Assessment Plan, two NDE-related tasks were defined. One was to assess the efficacy of nondestructive methods to measure the as-assembled residual stress field in the test articles and the Orbiter flowliners. The second task was to assess the efficacy of improved/refined nondestructive examination methods to reduce the inspection threshold for crack detection below the current threshold of 0.075 inch. Although the residual stress task is important and work is progressing on that topic, it is not being covered in this report. A more detailed version of this report is contained in Appendix D.5.1.

The recommendations and observations in this report were derived in part from a review of the NDE effort at KSC on March 10, 2004. A team of seven NDE experts with extensive backgrounds in NDE was selected from a pool of NDE experts who are members of the NESC's NDE Super Problem Resolution Team (SPRT). The team was interested in (1) assessing the current NDE techniques and capabilities on the flowliner and the weld repairs; (2) reviewing the plans for performing NDE on the BSTRA flowliners; and (3) estimating the potential increased inspection capabilities that could be realized with improvements in NDE to find smaller cracks. In addition, the NESC review included the added focus of trying to identify what else could be done to enhance flowliner safety.

The ability to find smaller cracks than 0.075 in. has been demonstrated by industry many times over. The 0.075 in. limit is a limit that is considered readily attainable by many technologies such as eddy current, ultrasound, and dye penetrant. NASA document MSFC-STD-1249, "Standard NDE Guidelines and Requirements for Fracture Control Programs" (Sept. 11, 1985) (located in Appendix D.5.1) outlines the standard detection limits for which it is assumed that one can obtain a detection limit of 90/95 (90 percent probability of finding a flaw with 95 percent confidence). Based on that document, finding cracks of 0.075 in. would be considered standard and would not require the extra work of performing a POD study. In the original effort by USA to find cracks in flowliners, this would be a standard limit for USA technicians and engineers to work towards given the program constraints.

There are review studies that show the ability to attain lower detection limits. These studies usually are built on standard samples with well manufactured real flaws. A request of the DoD's NTIAC's office (Nondestructive Testing Information Analysis Center) produced two studies highlighting the accuracy of eddy current methods. One study by Robert Lord of McDonnell Douglas Corp. (located in Appendix D.5.1) assessed the ability of dye penetrant and eddy current methods to find small cracks in F-15 spars (Material – Ti-6Al-4V). The study shows the ability of both dye penetrant and eddy current methods to reliably detect cracks smaller than 0.020 in. Another report by Forsyth and Fahr of the Institute of Aerospace Research of the National Research Council of Canadian (located in Appendix D.5.1) shows the ability of automated eddy

current technique to detect cracks in the range of 0.020 in. in engine disks, while manual eddy current methods were less accurate.

Based on these reports, the NESC NDE team reached the following conclusion (finding):

Crack sizes smaller than 0.075 in. should be detectable and, with automation and care, one should approach the 0.020 in. limit. The NESC NDE team also had several recommendations that are relevant to this report and which are highlighted in the NESC Review of Shuttle Flowliner Nondestructive Evaluation Report (attached in Appendix D.5.1). Those recommendations dealt with (1) the execution of a proper POD study, with the fact that all the crack sizes found by USA were larger than 0.100 in. and none were found less than 0.100 in., and (2) a need to assess the surface condition of the slots after they had been polished.

7.8 Probabilistic Risk Assessment

Structure of the Analysis

This PRA is structured in the form of event sequence diagrams (ESD). The diagrams follow the path of pivotal events necessary to go from an initiating event to the failure condition of interest. For this study, the failure event has been defined as SSME failure due to debris released into the fuel line. Comparing the risk of this failure to SSME catastrophic risk is conservative, since debris release might not cause catastrophic failure. Because of the small size and simple structure of the ESDs needed for this problem, they are modeled in Excel and quantified using a Monte Carlo simulation add-on package called Crystal Ball. The ESDs have also been input into QRAS, and this tool could be used in later analyses.

The ESDs are shown in Figures 7.8-1 and 7.8-2 for the circumferential and axial cracks, respectively. Six initiating events are defined, with three for circumferential cracks and three for axial. Axial cracks toward and away from the weld are combined because of a lack of detailed data that would differentiate them. When more detailed analysis results become available, the axial directions can be separated into six events. Similarly, the upstream and downstream liner data are combined. Separating the liners would double the number of initiating events.

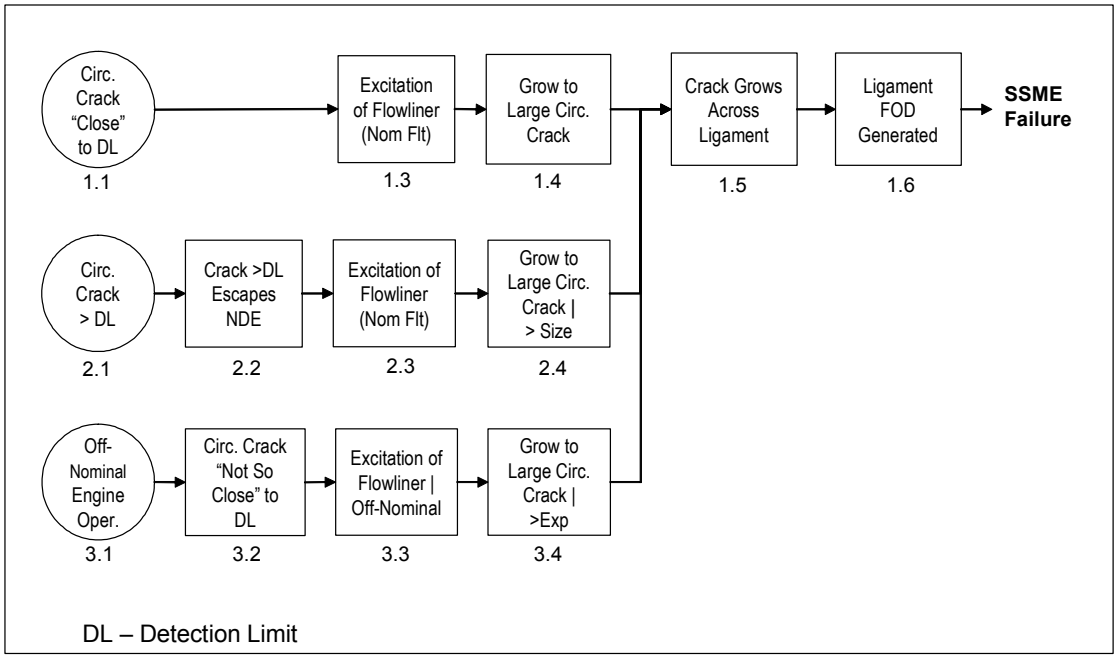

Figure 7.8-1. Event Sequence Diagram For Circumferential Cracks

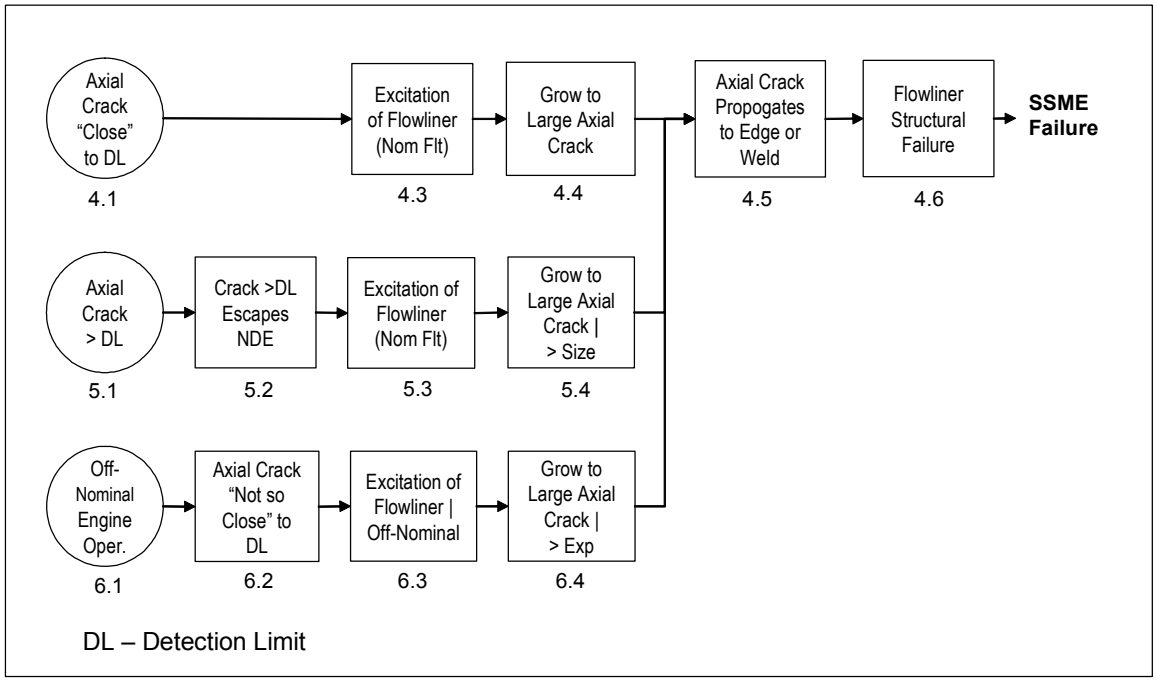

Figure 7.8-2. Event Sequence Diagram For Axial Cracks

Event Quantifications

The following paragraphs provide information on how each initiating and pivotal event in the analysis is quantified. Background information and data used are provided for each event. Assumptions and approximations made are stated. Finally, the exact distribution used in the analysis is also provided. To avoid repetition, similar events are organized together with common assumptions listed once. Events that are identical are grouped together with one event definition.

Crack Initiation Events (1.1, 2.1, 3.2, 4.1, 5.1, 6.2)

These events all deal with the initiation of cracks in the flowliner. Defining exactly when a crack "initiates" is somewhat problematic since incipient cracks can be assumed to be very small at the start of a flowliner's life. The PRA deals with this by using the historical crack rate data that has been observed to date. Crack initiation is then looked upon as a rate of occurrence or "birth process" that is somewhat independent of an exact threshold for crack size. Structural analyses of crack initiation have not yet given results that are suitable for use in the PRA. A screening efficiency of 50 percent for the current inspection technique is assumed. (The current analysis relies on the earlier POD studies that qualified inspection procedures with a 0.075 inch 90/95

detection limit). The NDE escape event sequence deals with the possibility of missing a crack from the 50 percent that would ideally be screened. Additionally, no credit has been given for the slot polishing conducted in 2002. For the case of off-nominal engine operation, it is assumed that increased exposure of the flowliner to flow-induced excitation will occur. The screening efficiency factor is removed for the crack initiation events on these paths to account for the possible growth of smaller cracks to failure.

Table 7.8-1. Flowliner Crack History in the Current Fleet

Orbiter Vehicle	Flights	Circumferential Cracks	Axial Cracks	Total Cracks
103	30	0	3	3
104	26	2	1	3
105	19	0	2	2
Total	75	2	6	8

All crack initiation events are quantified based on the historical observation of cracks in the current fleet of Orbiters with Inconel 718 liners. Table 7.8-1 summarizes the flowliner crack history. Bayesian updating of a non-informative prior is used to find the 50 percent and 95 percent confidence bounds for circumferential and axial crack occurrence per flight. The event quantifications use a Lognormal fit to these two percentiles to facilitate application of the screening factor where it is used. The Lognormal has a similar shape to the Beta for these cases, so this approximation is minor. The uncertainty from the Bayesian updating process results in error factors of 2.3 for the circumferential crack events and 1.7 for the axial. The error factor is defined as the ratio of the 95th percentile over the 50th percentile. The crack initiation event quantifications are shown in Table 7.8-2.

Table 7.8-2. Crack Initiation Event Quantifications

Event Number	Event Name	50 Percent	95 Percent
1.1	Circumferential Crack Close to DL	0.0175	0.0403
2.1	Circumferential Crack Greater Than DL	0.0175	0.0403
3.2	Circumferential Crack Not So Close to DL	0.0350	0.0805
4.1	Axial Crack Close to DL	0.0437	0.0749
5.1	Axial Crack Greater Than DL	0.0437	0.0749
6.2	Axial Crack Not So Close to DL	0.0874	0.1499

Off-Nominal Engine Operation Events (3.1, 6.1)

A variety of off-nominal conditions have been raised as possible risks for exposure of the flowliners to extended excitation. Some preliminary risk estimates have been made for these conditions, all ranging below the estimated SSME shutdown risk of 1 in 255. For the current analysis, the assumption has been made that the 95 percent uncertainty bound is approximately equal to the SSME shutdown risk, rounded to 1 in 250 (0.004). In order to maintain a relatively high median risk, an error factor of 2 is assumed. Because they are quantifying the same event, the two off-nominal events are tied together in the ESD quantification so they always have the same value. Events 3.1 and 6.1 have the same value drawn from a Lognormal uncertainty with 50 percent = 0.02 and 95 percent = 0.04.

Flowliner Excitation Events (1.2, 2.3, 3.3, 4.2, 5.3, 6.3)

These events are included in the ESD to account for the variable nature of flowliner excitation. Because the crack initiation events are based on the total flight history, these events are all currently set to 1.0. If any changes are made to reduce the likelihood of flowliner excitation, the improvement will be reflected in these events. Additionally, if the fatigue life analysis uses a loading spectrum that has a specific likelihood, that likelihood can be reflected in these events. Events 1.2, 2.3, 3.3, 4.2, 5.3, 6.3 are all set to a value of 1.0.

NDE Escape Events (2.2, 5.2)

A POD study has not been conducted for the current inspection method. Qualitative statements that the inspection is capable of finding flaws below the detection limit support it being fairly reliable. A B-basis capability is assumed for this analysis, which is a 95 percent confidence that 90 percent of flaws at the detection limit are detected. An error factor of three is assumed for the uncertainty. This yields escape probabilities of 0.0333 at 50 percent and 0.10 at 95 percent. The two percentiles are fit to a Lognormal uncertainty distribution. The full 50 percent of cracks that are considered screened out from event 1.1 are assumed to be above the detection limit for this branch of the ESD. This is a conservative assumption that is made due to the lack of information on the distribution of crack sizes. The likelihood of cracks larger than the detection limit can be examined in an updated analysis. Because the axial and circumferential cracks have no fundamental difference, events 2.2 and 5.2 are tied together in the ESD quantification so they always have the same value. Events 2.2 and 5.2 have the same value drawn from a Lognormal uncertainty with 50 percent = 0.0333 and 95 percent = 0.10.

Fatigue Life Crack Growth Events (1.4, 2.4, 3.4, 4.4, 5.4, 6.4)

All initiated cracks are assumed to be "close" to the detection limit and therefore have the same fatigue life as a crack at the detection limit. For this current analysis, results of the "Forward Fracture Analysis" (FFA) that was conducted by the program prior to the ITA study are used. This should be updated as new fracture mechanics analysis results become available. The fracture life analyses define failure as a large crack, which has had several definitions. No specific size is explicitly assumed in the PRA analysis. The FFA found a minimum fracture life of 0.8 flights for one circumferential crack location. This analysis assumes that all circumferential locations have the same life. The FFA is by intention a conservative bound on fracture life and contains multiple conservative assumptions, including material properties, loading spectrum, and residual stress. To account for these conservatisms, this analysis assumes that the FFA results correspond to an A-Basis tolerance bound, which is a 95 percent confidence limit on the 1st percentile of a population. The 0.8 life is converted to a failure rate and expanded to one flight assuming an Exponential distribution. This yields a 95th percentile failure rate of 1 in 80 (0.0125). An error factor of three is assumed for the uncertainty and yields a 50th percentile of 1 in 240 (0.0042). Assuming a higher uncertainty would reduce the median failure rate. The 50th and 95th percentiles are used to define a Lognormal uncertainty distribution for the crack growth event. For the axial crack case, the same procedure is performed assuming a fracture life of two flights. This assumption should be updated in later analyses if new information becomes available.

No fracture life analysis is available for either the inspection escape or off-nominal performance ESD branches. An inspection escape crack should not be considerably larger than the detection limit, but could have significantly shorter life. The off-nominal performance case could cause extended excitation of the flowliner. For both of these cases, an increase by a factor of five is

assumed. The inspection escape case has a factor of five increase on failure rate, and the off-nominal case has a factor of five increase on duration. These assumptions should be updated in later analyses if new information becomes available. All fatigue life crack growth event quantifications are shown in Table 7.8-3.

Table 7.8-3. Crack Fatigue Life Events

Event Number	Event Name	50 Percent	95 Percent
1.4	Grow to Large Circumferential Crack	0.0042	0.0125
2.4	Grow to Large Circumferential Crack Given Larger Size	0.0203	0.0609
3.4	Grow to Large Circumferential Crack Given Larger Exposure	0.0203	0.0609
4.4	Grow to Large Axial Crack	0.0017	0.0050
5.4	Grow to Large Axial Crack Given Larger Size	0.0083	0.0248
6.4	Grow to Large Axial Crack Given Larger Exposure	0.0083	0.0248

Crack Propagation Events (1.5, 4.5)

For the case of circumferential cracks, this is growth across the ligament, leaving a "tab" that is secured at one end. For axial cracks, the growth would be to the flowliner attachment weld or to the free edge. The eight cracks observed in the Inconel liners were all fairly small. The two circumferential cracks were both roughly 0.3 inches and the six axial cracks ranges from 0.1 to 0.23 inches. This would indicate that either all the cracks are very new, or that they either grow slowly or tend to arrest. (Analysis and testing is underway that will answer the question of whether the cracks arrest). In order to quantify the circumferential crack growth event for Phase I, the total fleet history of five cracks is used. This adds three circumferential cracks from the 102 CRES liners, which had a smaller ligament distance between the slots. One of these three cracks grew across the ligament. Bayesian updating of a non-informative prior yields a Beta distribution with parameters (2,5). For the axial cracks, six cracks have been observed with zero growing to a large size. Bayesian updating is also used for this event, yielding a Beta(1,7) uncertainty. Event 1.5 has a Beta(2,5) uncertainty and event 4.5 has Beta(1,7).

Failure Propagation Events (1.6, 4.6)

The two failure propagation events are different but have a similar lack of data. Some preliminary analyses have been done for both, but results have not been verified. The analysis can be updated if better information becomes available. For the circumferential crack across the ligament, preliminary analysis has been done to show that the tab would have a much higher natural frequency than the driving loads. There is also the one case where the crack grew across and the ligament was not lost. It is not known how many flights the one observed tab endured. For the axial cracks, analysis has indicated that the cracks should arrest due to leaving the areas of highest residual stress and loading. It is also not clear how rapidly a large axial crack in either direction could propagate to failure. Growth of a crack all the way to the weld or to the free edge would not necessarily cause a rapid failure. Both of these events have been called unlikely by the experts. For the current analysis, this has been conservatively assumed to be a mean value of 1 in 10. The analysts also appear fairly confident that there is not a very high risk, so a Beta(5,45) is assumed. This Beta has a 50 percent of 0.095 and 95 percent of 0.177. Since the two events are different, they are not tied together in the simulation. Events 1.6 and 4.6 each have a Beta(5,45) uncertainty.

Results

The results of the current analysis show that that flowliner cracking is not predicted to be a significant contributor to SSME risk. While the uncertainty of the risk estimate is rather large, the upper bounds on that uncertainty are in the range of 2.0E-5, or 1 in 50,000. Figure 7.8-3 shows the distribution of resulting SSME Failure risk estimates for a 40,000 trial simulation.

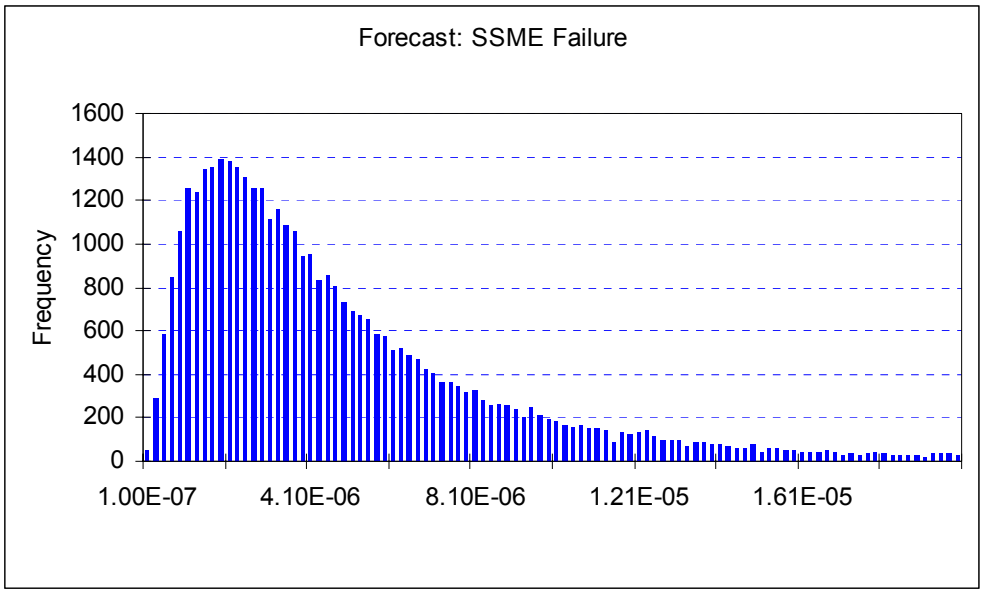

Figure 7.8-3. Distribution of SSME failure risk

Summary

Results from the PRA show the risk of SSME damage due to cracks in the flowliner is an insignificant contributor to the overall SSME catastrophic risk, assuming inspection after every flight. While the PRA results currently have a very wide uncertainty band, large changes in multiple inputs would be required to increase the risk to a level where it is a significant contributor to the overall SSME catastrophic risk. The median (50 percent) and 95 percent upper bound of the risk estimate are expected to be reduced by results from on-going tests and analyses and the elimination of overly conservative assumptions made in earlier analyses. The PRA models the risk from flowliner cracks in a logic model called an event sequence diagram (ESD). The ESD contains six initiating events and 20 pivotal events linked in sequences that lead to failure. Uncertainty distributions are defined for the risk of occurrence for each of the 26 events. Monte Carlo simulation is used to propagate the risk uncertainties through the ESD into a total risk estimate.

8.0 ROOT CAUSES, OBSERVATIONS AND FINDINGS, PROPOSED FLIGHT RATIONALE

In this chapter, the findings from the Root Causes investigation is presented along with the supporting facts. Next, the significant conclusions reached from the technical assessment described in Chapter 7 is stated in the form of Observations and Findings. Using the results of the root causes investigation and findings as a foundation, a strategy to achieve a Flight Rationale is proposed. Recommendations for developing the flight rationale are detailed in Section 9.0.

8.1 Root Causes Investigation

There are four potential mechanisms at low temperatures for initiating cracks. These mechanisms include low cycle fatigue, high cycle fatigue, overloads, and stress corrosion cracking. **There is strong evidence suggesting that high cycle fatigue is the mechanism that initiated the cracks.** However, for one axial crack location, low cycle fatigue could also be a contributing cause. There is no evidence to suggest that the cracks found in the fleet were produced by an overload or stress corrosion cracking. Low cycle fatigue and high cycle fatigue are discussed in more detail below.

The high cycle fatigue regime is characterized by elastic material response for which crack initiation is highly sensitive to discontinuities such as manufacturing defects. The scatter in fatigue life is quite large in this regime and variations of an order of magnitude in life above and below the median life is an accepted norm. To appreciate how this applies to the flowliner, consider the fatigue and statistical data plotted in Figure 8.1-1. These data were compiled for an aluminium alloy subjected to constant amplitude cyclic loadings in a rotating bend specimen [ref. S. Webber and J.C. Levy, 1958]. Notice that for low cycle fatigue at an alternating stress of 50,000 lbs/in^2, the mean life is about $5x10^4$ cycles and the data scatter in life is about a factor of two. Then, for high cycle fatigue at the alternating stress of 35,000 lbs/in^2, the mean life is about $1.5x10^7$ cycles but the data scatter in life is about two orders of magnitude. This is typical of high cycle fatigue behavior exhibited by all structural metals. On close examination of failed laboratory specimens, the cracks that form in specimens exhibiting short/early fatigue lives typically initiate at some local stress concentration feature such as a scratch, gouge, or surface pit. In contrast, specimens exhibiting longer lives typically experience cracks initiating at microstructural defects in the materials such as inclusion particles. Extending this behavior to a typical structure, such as the flowliner, subjected to high cycle fatigue, a single “dominant crack” typically controls the fatigue life. This is especially the case when high cycle fatigue is exacerbated by contributing factors such as global stress concentrations due to geometry, local stress concentrations due to surface roughness and/or metallurgical features, and tensile mean stress. This “dominant crack” scenario is consistent with the cracking behavior observed in the fleet where only 11 cracks nucleated and grew to a detectable size in the 24 flowliners (2

flowliners at the gimbal joint of each LH_2 feedline), each with numerous potential crack initiation sites.

Intermediate cycle fatigue implies predominately elastic behavior, but with small amounts of plasticity. Likewise, low cycle fatigue typically exhibits considerable plasticity. Whether intermediate or low cycle fatigue, this plasticity can cause the stress concentration influence of manufacturing defects to be relieved or diminished. This reduces the number of preferred sites where a crack might initiate. As the cyclic stress increases, the degree of local plasticity increases. This promotes the initiation of numerous cracks initiating at about the same life, and results in both the mean life and data scatter decreasing. In fact, if the cyclic stresses are too high, there could be multiple low cycle fatigue cracks emanating from the same general site (crack-tip branching). This is not the behavior exhibited by the flowliner cracks in the fleet.

Two distinctly different (root causes) scenarios are required to describe the crack behavior exhibited by the flowliners. Root cause Finding 1 addresses the behavior of all circumferential cracks initiating along the straight sides of the drainage slots and extending across the ligament between slots and the axial cracks initiating at the radius of drainage slots and extending toward the free end of the flowliner. Root cause Finding 2 addresses the behavior of the axial crack initiating at the radius of the drainage slot and extending toward the assembly weld attaching the flowliner to the gimbal joint flange. These two root cause findings are fully documented in the following sections.

Reference

Webber, S. and Levy, J.C.: Cumulative Damage in Fatigue with Reference to the Scatter of Results, S&T Memo. No. 15/58, Technical Information and Library Services, Ministry of Supply, August 1958. (Work carried out at the Northampton College of Advanced Technology, London, U.K., Contract No. 7/GEN/1748/PR3).

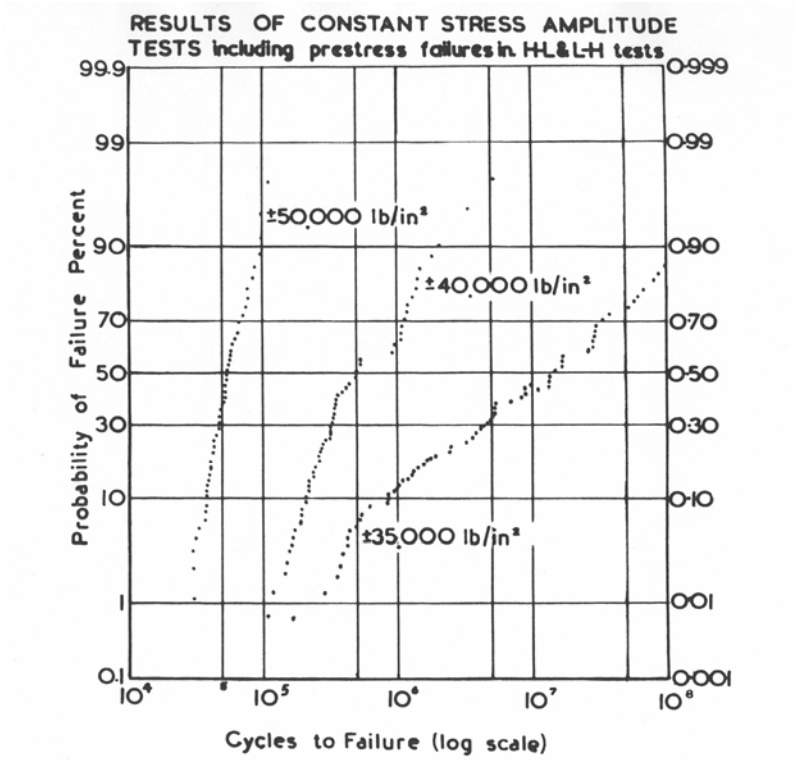

Figure 8.1-1. Statistical distribution of high cycle fatigue data (rotating bending) for wrought D.T.D 683 high-strength aluminium alloy (ref.: Webber and Levy, 1958)

8.1.1 All Circumferential Cracks and Axial Cracks at the Slot End Opposite the Assembly Weld

Root Cause Finding 1: The most likely cause of the circumferential cracks initiating along the sides of the drainage slot and extending across the ligament between slots and the axial cracks initiating at the radius of the drainage slot and extending toward the free end of the flowliner (end opposite the assembly weld) observed in the fleet is **high cycle fatigue assisted by geometric and local (surface roughness) stress concentrations**.

Supporting Facts:

1. Only 11 cracks were found in the fleet. (If this were low cycle fatigue, one would expect many more cracks with approximately 6,000 potential crack initiation sites).

2. All Orbiters saw between 19 and 30 flights (2 cracks in OV-105 in 19 flights; 3 cracks in OV-104 in 26 flights; 3 cracks in OV-102 in 28 flights; and 3 cracks in OV-103 in 30 flights).

3. In the CRES 321 flowliners in OV-102, one circumferential crack grew completely across the 0.25-inch ligament. In the Inconel 718 flowliners in the other Orbiters, no circumferential cracks grew completely across the 0.75 inch ligament. In addition, most cracks in the Inconel 718 were essentially the same length.

4. There are four potential mechanisms at low temperatures for initiating cracks. All but high cycle fatigue can be ruled out. (There is no evidence of stress corrosion cracking, cracks from overloads, or low cycle fatigue for these crack locations).

5. High frequency (greater than 1,000 Hz) flow induced cyclic loading sources are known to exist.

6. The natural frequencies (greater than 1,000 Hz) of the flowliner fall within the range of the known excitation sources.

7. The slot punching process results in rough surfaces with scratch-like and gouge-like defects. Pit-like defects were found in the MPTA CRES 321 flowliner but not in the recently fabricated Inconel 718 flowliner test article. (Photographs taken on the Orbiter slots in 2002 also show scratches and gouge-like defects).

8. High cycle fatigue data of metallic materials exhibits significant data scatter (an order of magnitude or greater under controlled laboratory conditions).

9. The slot geometry has high stress concentration factors in excess of 4.0 in some locations (Section 7.3).

   For a simple tensile load, the stress concentration at the slot is only about 1.6. However, the stress concentration factor is considerably higher for the high frequency modes considered to be excited by the flow-induced loading mechanisms. For the nine-node (9ND) mode shape of the upstream flowliner, the stress concentration factors (transfer ratios) are 3.5 and 2.7 for the circumferential crack location and the axial crack at the free end away from the weld, respectively. In the downstream liner for the C4ND mode, the stress concentration factors (transfer ratios) are 3.3 and 4.0 for the circumferential crack location and the axial crack at the free end away from the weld, respectively.

10. The cracks found in OV-104 exhibit the following characteristics of fatigue: features similar to striation marks, tear ridges indicative of cyclic loading, and no evidence of plasticity (Appendix C.2).

    Edge replicas were taken of the circumferential crack between slots 42-43 in OV-104 and the axial crack at slot 9 extending toward the free end of the flowliner in OV-104 [Ref.: viewgraphs provided by Raymond Patin]. The two crack faces were slightly displaced, so only a small part of the crack surface was captured on the replica. A metallurgical failure analysis of the replicas was conducted by NASA JSC to determine the likely cause of the cracks. The circumferential crack was described as exhibiting a fracture surface indicative of fatigue. Tear ridges perpendicular to the crack edge indicate a simple or reversed <u>bending</u> loading mechanism. Some crack branching, well into the crack propagation stage, was also observed. The axial crack was also described as exhibiting a fracture surface indicative of fatigue. Tear ridges parallel to the crack edge indicate a <u>tensile</u> loading mechanism. No crack branching was observed. Both cracks exhibited markings that resembled striation marks.

11. The crack found in the MPTA E1 flowliner exhibits the following characteristics of fatigue: crack initiated at a surface defect on the OD corner of the slot, smooth crescent-shaped fracture footprint, 16 beachmarks, and striation-like banding, and no evidence of plasticity (Appendix C.3).

    Based on an examination by the edge replication method of the slots in the MPTA CRES 321 flowliners, no additional fatigue cracks greater than 0.030 inches were found. One fatigue crack greater than 0.030 inches was previously found in 2002. This was a circumferential crack initiating from a gouge-like defect at the OD corner of the slot. A metallurgical failure analysis was conducted by Boeing to determine the likely cause of this crack [Reference: Boeing Lab Report No. M&PE-2-1327, January 3, 2003]. The results of the analysis are summarized as follows: "Fracture traces indicated that

cracking initiated from a grinding mark on the "backside" (i.e., OD side) of the flowliner near the edge of the punched inspection/drain hole. Failure initiated at the flowliner OD and traveled across the part thickness, suggesting fatigue might have been influenced by bending loads. The base material had no visible necking (ductile deformation) adjacent to the fracture and exhibited the relatively smooth, crescent-shaped fracture "footprint" typical of classical fatigue. Approximately 16 beachmarks (typically associated with random, varying, or intermittent loads) were observed representing successive positions of the advancing crack front. High magnification (4000x to 8000x) analysis found fracture features which displayed striation-like banding, however, no extended or clearly defined striations were found."

12. The flowliners in the orbiter fleet do <u>not</u> exhibit the characteristics of widespread fatigue damage (Appendix C.1).

    Each flowliner has numerous slot locations of approximately the same peak alternating stress. For example, the nine-node (9ND) mode shape has nine hot spots where the peak stresses are similar. In addition, there are several locations around each slot where high stress concentrations exist. Therefore, numerous cracks of various lengths would be expected if the structure experienced low cycle fatigue. This behavior is often referred to as widespread fatigue damage or multi-site fatigue damage. An example of widespread fatigue damage is the failure of the CRES 321 flowliners in the LOX feedlines during the qualification tests conducted in 1977-78 [Federal-Mogul Arrowhead Products, report MPS-QTR-13542-302, B, G-2, August 20, 1981]. Fourteen ligaments between the slots in the downstream flowliners and 8 ligaments in the upstream flowliner were cracked. A metallurgical failure analysis was conducted by Rockwell [Rockwell International, Internal Letter, 282-204-081-185, August 24, 1981]. The results were summarized as follows: "A scanning electron microscope examination revealed that cracking had propagated by fatigue with final failure due to overload. No evidence suggestive of the fracture initiation site could be found. No material or processing defects were apparent. It appears that failure was the result of the overtest environment to which the flowliner had been exposed". This fatigue behavior is in stark contrast to the cracking behavior exhibited by the MPTA flowliner and the flowliners in the orbiter fleet.

8.1.2 Axial Crack at the Slot End Nearest the Assembly Weld

Root Cause Finding 2: The most likely cause of the axial crack initiating at the radius of the drainage slot and extending toward the assembly weld is **a combination of low cycle and high cycle fatigue assisted by geometric and local (surface roughness) stress concentrations.**

Supporting Facts:

1. High fidelity examination by the edge replication method of the MPTA CRES 321 flowliner revealed the existence of numerous micro-cracks initiating from pit-like surface flaws (0.001 to 0.005 inches) in the axial location of the slot near the weld side. These micro-cracks exhibited high plastic strain (blunting and crack branching). This suggests *low cycle* fatigue as a possible mechanism for axial cracks growing toward the weld. The most likely low cycle loading condition is the thermal shock resulting from the numerous LH_2 feedline fill. (Refer to Appendix D.5.2).

2. The slot punching process results in rough surfaces with scratch-like and gouge-like defects. Pit-like defects were found in the MPTA CRES 321 flowliner but not in the recently fabricated Inconel 718 flowliner test article. (Photographs taken on the Orbiter slots in 2002 also show scratches and gouge-like defects).

3. Only one axial crack at the weld end of the slot in the upstream flowliner was found in the fleet (OV-103 with 30 flights). There were no axial cracks at this location found in the other Orbiters (OV-105 with 19 flights; OV-104 with 26 flights; and OV-102 with 28 flights).

4. High frequency (greater than 1,000 Hz) flow induced cyclic loading sources are known to exist.

5. The natural frequencies (greater than 1,000 Hz) of the flowliner fall within the range of the known excitation sources.

6. This location is nearest the assembly weld and has a high level of residual stresses (Appendix D.3.3). In addition, this location also has high stresses from the thermal shock due to the LH_2 fill. The combination of the weld residual stresses and the thermal shock results in a local stress at the slot in excess of yield in CRES 321. Likewise, the stress approaches yield in Inconel 718 and would exceed yield at any local stress concentration such as a defect produced by the punching process. Therefore, local yielding could occur on the first LH_2 fill and would likely "shake down" to nominally elastic behavior thereafter. This is consistent with the characteristics of the micro-cracks found in the

MPTA flowliners (small cracks exhibiting evidence of plastic deformation but with little crack propagation).

7. At the point of the slot nearest the assembly weld location, for the nine-node (9ND) mode, the stress concentration factor (transfer ratio) is about 1.6 for the upstream liner and about 2.2 for the downstream liner.

8. Supporting Facts 1 and 2 may be unique to OV-102, the only Orbiter with the CRES 321 flowliners, because Inconel 718 has a significantly higher yield stress than CRES 321. However, all the other facts are directly applicable to the Inconel 718 flowliners.

8.1.3 Conclusions from Root Causes Investigation

Several important conclusions are drawn from the root causes investigation. The initiation and growth of only a few cracks in the orbiter fleet can be attributed to the combined influence of geometric stress concentrations due to the drainage slots, local stress concentrations due to surface roughness produced by the manufacturing process, residual stresses from the flowliner forming process and welding to the feedline flange, low cycle fatigue due to thermal stresses from the LH_2 fill, and high cycle fatigue due to flow-induced loads. Of these contributing factors, only the local stress concentration due to surface roughness can be corrected in the fleet without redesigning the flowliners. The original slot punching process was crude and resulted in a high degree of surface imperfections. Removing these defects as potential crack initiation sites will significantly increase the fatigue life to crack initiation. If all pre-existing fatigue cracks are repaired, removing the surface defects by polishing effectively (for all practical purposes) eliminates the original source of the cracking problem. Returning the orbiters to flight, therefore, depends on monitoring (by in-service inspections) future crack initiation and growth to ensure that all fatigue cracks are found and repaired before they grow to the critical crack size. In fact, the slots were polished in 2002 to improve the slot surface quality and a procedure to inspect the flowliners after every flight was implemented.

8.2 Observations and Findings

8.2.1 General Findings

F-1. The past flight history and the root causes investigation leads to the conclusion that the actions taken in 2002 to repair the LH_2 gimbal joint flowliners render the Orbiter safe to fly[a]. This is provided the flowliners are inspected[b] before return-to-flight to ensure that all surface flaws were removed[c] by polishing and all fatigue cracks are repaired. The flowliners must also be inspected after every flight and all fatigue cracks repaired.

Notes:

a. This does not address off nominal conditions.

b. Inspections will require a high fidelity verification of slot surface quality and the absence of fatigue cracks.

c. If the original polishing was not effective, then additional polishing will be required.

F-2. Results from the PRA performed in Phase I show the risk of SSME damage due to cracks in the flowliner is an insignificant contributor to the overall SSME catastrophic risk, assuming inspection after every flight (Section 7.8).

8.2.2 Specific Technical Observations and Findings

Methods for determining residual fatigue life, critical crack sizes, and crack detection (inspection).

<u>Observations</u>:

O-1. Since the fatigue crack growth rate varies exponentially with the alternating stress intensity factor, $da/dN = c(dK)^n$, predictions of residual fatigue life are highly sensitive to small changes in the peak stresses in the loading spectrum. Therefore, the fatigue life predictions are highly sensitive to the engineering approximations used in developing the load spectrum (Section 7.3).

O-2. The mean stress effect is primarily a crack closure effect. Because crack closure is highly dependent on crack-tip plasticity, crack closure effects can only be predicted on a cycle-by-cycle basis which requires precise knowledge of the loading sequence in the spectrum. The knowledge of the flowliner loading spectrum required to predict crack closure cannot be specified. Changing the R-ratio from one loading block to another in the spectrum without accounting for crack closure is inaccurate and non-conservative.

Therefore, it is more conservative to base the crack growth predictions on the data for R= 0.9, where no closure effects are present in the crack growth rates (Section 7.3).

O-3. Based on the fracture morphology exhibited by the crack in the MPTA flowliner, fatigue cracks appear to initiate as a corner crack and grow in a self-similar manner before transitioning to a through-crack. Therefore, it is both reasonable and conservative to assume that the crack initiates as a quarter-circular crack, grows with an aspect ratio of a/c=1, then transitions to a through-crack when a=c=0.050" (Section 7.3).

O-4. Structural metals have been shown to exhibit an increase in the fatigue crack growth threshold with decreasing temperature [Ref.: P.K. Liaw and W.A. Logsdon, Engineering Fracture Mechanics, Vol. 22, No. 4, pp. 585-594]. This behavior is directly related to temperature-dependent microstructural effects that can be explained from a materials science viewpoint. This is the trend exhibited by Inconel 718. Therefore, it is appropriate to use the crack growth rate data recently obtained at -423° F even though the NASGRO data at -320° F is more conservative (Section 7.3).

O-5. The stress intensity factor is a function of crack length and applied load. Also, the crack growth rate is an exponential function of the alternating stress intensity factor. Therefore, decreasing the crack detection size below the current value of 0.075 in. will exponentially increase the residual life. However, the fracture mechanics results show the effect to be small for more severe loading spectra (Section 7.3).

O-6. The finite element modal analysis of the dominant frequencies being excited during the BTA test confirms the existence of both membrane and bending components of strain at the crack initiation sites. Therefore, transfer ratios for the membrane component and bending component have been developed and the fracture mechanics analysis has been modified accordingly. The predicted values of residual fatigue life are significantly affected by the membrane component. The results show that the approximation of assuming only a bending component of strain is highly non-conservative and is not supported by the structural dynamics analysis (Section 7.3).

O-7. Because the fatigue loading spectrum is predominantly due to flow-induced vibration, the fracture mechanics analysis must be directly integrated with the structural dynamics analysis. The structural dynamics analysis uses a transfer ratio approximation to relate the mid-ligament strains measured in the BTA test to the crack initiation sites at the edge of the slots. All fracture mechanics sensitivity studies were conducted for the transfer ratio method (Section 7.3). As a further refinement of the fracture mechanics methodology, a fully three-dimensional finite element analysis method was developed that rigorously combines the fracture mechanics and the structural dynamics. This approach does not require the use of transfer ratios (Section 7.4). Comparing the results from the two methods, it is obvious that the transfer ratio approximation method is overly conservative.

Findings:

F-3. For the Boeing load history derived from the BTA/GTA test data and the NESC-derived loading spectra, the critical circumferential crack size is 0.020 inch for a residual fatigue life greater than four flights for the upstream liner and greater than one flight for the downstream liner. (Section 7.4).

F-4. The prediction of the residual fatigue life using fracture mechanics must include both the membrane and bending components for both the upstream and downstream flowliners (Section 7.3).

F-5. The conservative fracture mechanics crack growth predictions, based on the Boeing spectrum, are not consistent with the observed fleet cracking behavior (many more cracks and all circumferential cracks completely across the ligament) (Section 7.3).

F-6. The fatigue life to crack initiation predictions, based on the Boeing fatigue spectrum, result in many more cracks than are observed in the fleet. Using a conservative correction for the mean stress, the fatigue life is 4 missions for the upstream flowliner and 8 missions for the downstream flowliner. (To match the cracking pattern observed in the fleet in a crack initiation simulation requires the Boeing spectra to be scaled by a factor of less than one half) (Section 7.5).

F-7. Analytical results show that LPB is a surface enhancement treatment that can extend flowliner high cycle fatigue life (Appendix D.6).

F-8. Based on an examination by the edge replication method of the slots in the MPTA CRES 321 flowliners, no additional fatigue cracks greater than 0.030 inches were found. (One fatigue crack greater than 0.030 inches was previously found in 2002. This was a circumferential crack initiating from a gouge-like defect at the OD corner of the slot), (Appendix D.5.2).

F-9. In addition, the high fidelity examination by the edge replication method of the slots in the MPTA CRES 321 flowliners revealed the existence of numerous micro-cracks ranging from 0.001 to 0.005 inches. The micro-cracks were oriented in the axial direction facing the assembly weld and initiated from pit-like surface flaws. These micro-cracks exhibited evidence of plastic strain in the form of crack-tip blunting and crack branching. (The pit-like surface flaws were not found in the recently fabricated Inconel 718 flowliner test article) (Appendix D.5.2).

F-10. Previous POD studies of edge cracks have established 0.020 inches as the detection limit (90-95 percent confidence level) for conventional, automated eddy current and dye penetrant methods (Section 7.7).

F-11. Based on laboratory examinations of fatigue test coupons, the edge replication methods (acetate tape and RepliSet®) detected surface fatigue cracks as small as 0.001 inches under zero load. (Further work is required to establish POD data and the final inspection limit) (Section 7.6).

Flight Environment and Loading Spectra

Observations:

O-9. The acoustic environment of the bellows cavity is extremely complex. Fluid flow over geometric edges such as the trailing or leading edges of the flowliner slots can create "edge tones" if the fluid conditions couple to the local geometry. One possibility is the cavity formed by the bellows and flowliner(s) is an acoustic resonance. While acoustic resonance can be excited by "edge tones" many other physical conditions can also excite cavity resonance. General flow turbulence, pumping of flow through the slots from the duct, and excitation due to cavitation can all lead to resonance. Air flow tests can provide insight into the flow character around the slot and the acoustic character of the bellows cavity (Section 7.1).

O-10. CFD results confirmed that there is a backflow caused by the LPFP inducer. The reverse flow near the inducer blade tip is caused by the pressure difference between the pressure side (facing downstream into the pump) and suction side (facing upstream) of the inducer blade. The region of reverse flow extends far enough upstream to interfere with both the downstream and upstream flowliners at the gimbal joint. It also causes swirl to occur in the flow approaching the inducer. Thus the local flow will cross the flowliner slots at an oblique angle instead of along the axis of the feedline. Based on the computed CFD results, the swirl velocity in the cavity is about 10 percent of the inducer tip velocity. Reverse flow in the duct also interacts with the flow in the bellows cavity through the gap formed by the overlap between the upstream and downstream flowliners. A strong jet flow, with velocities of about 15 percent of the inducer tip speed, penetrates directly into the bellows cavity resulting in strong unsteady recirculation regions in the cavity (Section 7.1).

O-11. A comparison of the CFD results from both the Program Team and the ITA Team, with test data from the pressure measurements obtained in the "straight duct" test on the A1 test stand prior to the BTA and GTA tests, led to the following observations (Section 7.1):

a. There is a fundamental similarity in the pressure time-history calculated by the Program Team and the ITA Team. Both CFD results show a dominant 4N (four times rotational speed) unsteadiness in the pressure at a fixed location. Both CFD results show variations between the amplitudes of the four pressure peaks that occur during each revolution, even though the geometry, the initial conditions, and the boundary conditions are identical for the four quadrants of the computational domain.

b. There is a significant difference in the amplitude of the unsteady pressures calculated by the Program Team and the ITA Team. The range between the maximum and minimum pressure during one revolution was ~60 percent higher in the Program Team's CFD results, as compared to the ITA Team's CFD results. The ITA Team's CFD results were about 25 percent higher than the measurements from the hot fire test.

c. Significant differences are also seen between the gradients of pressure in the two CFD results. The Program Team's CFD results show sharper spatial and temporal gradients in pressure than are seen in the ITA Team's CFD results. This difference will be quantified when the ITA Team's CFD runs are converged to periodicity.

O-11. Factors affecting the similitude between the test article(s) and the Orbiter gimbal joint include the following:

1. The BTA flowliner backing (bellows) cavity was enclosed with a rigid, thick, and cylindrical shell instead of the flight hardware's flexible bellows. Therefore, the internal geometry of the backing cavity was different from the flight hardware (Appendix D.1.1).

2. The BTAs/GTAs used BX-250 foam for insulation instead of a flight hardware vacuum jacket. The calculated heat transfer of the test article is much higher than what would be expected in flight and most likely caused some vaporization of the LH_2 in the backing cavity. A two-phase flow environment would lead to significant changes in the local speed-of-sound, consequently altering the resonant frequency characteristics and interactions in the backing cavity, relative to the flight hardware (Section 7.1.1 and Appendix D.1.1).

3. Due to the different upstream geometries (internal components and feedline configuration), the A1 test stand velocity profile (for both the BTA and GTA tests) of the flow approaching the test article was different from the flow field profiles in the Orbiter feedlines. Thus, the approaching flow's interaction with the inducer's reverse flow may be significantly different from the flight vehicle (Section 7.1.2).

4. Because of the different internal geometry and configurations, the A1 test stand feedline acoustic modes (for the BTA and GTA tests) are likely to be different from the Orbiter feedline acoustic modes (Sections 7.1 and 7.1.2).

5. The test stand feedline mounting bracket (for the BTA and GTA tests) was of different material and configuration (both interface and dimensions) resulting in increased heat transfer into the test article relative to flight. Also, the different coefficients of thermal expansion between the material of the test hardware and the Orbiter hardware would result in different thermal stresses in the gimbal joint flange and could affect the inducer tip clearance (Section 7.1.1).

6. The gimbal joint weld bead in the BTA was machined smooth unlike those in the Orbiter and the GTA. Thus, the wall boundary layer in the BTA test will not experience the local separation that occurs in the flight vehicles and GTA test (Section 7.1).

Findings:

F-12. There are no direct measurements of the flowliner loads in flight. The Boeing load spectrum is semi-empirically derived and based on a series of conservative engineering assumptions in an attempt to ensure that a 'worst-case' nominal flight is enveloped by the spectrum (Section 7.2).

F-13. Excessive heat transfer into the BTA results in a lack of similitude with the flight environment in the flowliner cavity. This finding is based on the temperature measurements in the "bellows" cavity during the BTA test. The heat transfer was 8 times the value that occurs during flight, resulting in significant hydrogen vapor in the "bellows" cavity. The vapor concentration was higher in the upstream end of the cavity than in the downstream end, based on the thermal response of the bellows cavity wall (Section 7.1).

F-14. A significant load component in the BTA/GTA flowliners is due to a high frequency excitation. This has been attributed to an edge tone and/or cavity resonance. This supposition has not been conclusively shown to be part of the flight environment (Section 7.1).

F-15. CFD results for the straight duct hot fire test configuration have been verified by correlation with unsteady pressure measurements (Section 7.1).

F-16. (General Finding) The similitude between the BTA/GTA ground tests environment and the Orbiter flight environment could not be established. Therefore, there are uncertainties in the fatigue loading spectra developed from the BTA/GTA test data. Unverified scale factors have been applied to the loads in the fatigue loading spectra in an attempt to account for these uncertainties. Because of these uncertainties, there will be risks associated with any loading spectrum used to develop the flight rationale derived from the BTA/GTA experiment. These concerns notwithstanding, we have concluded that the ground test data can be a suitable database to establish the certification spectra provided conservative scale factors based on appropriate engineering judgment are used to account for the uncertainties.

8.3 Proposed Flight Rationale

A strategy for developing a flight rationale is proposed below. The proposed flight rationale is built on the following three approaches: Part I - Damage Tolerance Approach, Part II - Fatigue Life Approach (to crack initiation), and Part III - Risk Assessment. In the design process, the fatigue life to crack initiation approach and the damage tolerance approach are complementary. Fatigue analysis and testing is used to determine the service life until cracks emerge (i.e., nucleate or initiate) at the hot spots of the structure. (The fatigue life to crack initiation is sometimes referred to as *structural durability*). Thereafter, the damage tolerance approach based on fracture mechanics is used to determine the critical crack size and the required in-service inspection intervals and methods. If the critical crack size cannot be found by inspection, then the structure will be life limited. Furthermore, if the structure has been found to be susceptible to fatigue cracks during its service lifetime, then the damage tolerance approach is conservatively applied to ensure that a rogue flaw or undiscovered hot spot does not result in a catastrophic failure. Because of the uncertainty in the flight loads acting on the flowliners and the sensitivity of the fracture mechanics results to these loads, the development of the flight rationale might be difficult to achieve by only the damage tolerance approach. Therefore, the flight rationale may depend on results from both Parts I and II. Part III is a complement to both Parts I and II.

Part I. Damage Tolerance Approach

A damage-tolerant part is one that possesses the ability to resist failure due to the *presence of cracks* during its service life. A damage tolerance analysis *assumes the existence of a crack* in the most critical orientation and location of the structure. The size of the assumed crack is based on the method of inspection. A stress analysis of the structure is performed to determine the peak stress locations where fatigue cracks initiate. A crack of size equal to the inspection limit is assumed to exist in these peak stress locations. The service life loading spectrum is then applied to the peak stress regions where these cracks are located. A fracture mechanics analysis is used to predict the service life required for the assumed crack to grow to the critical crack size, usually defined as catastrophic failure. Material property data is determined from laboratory tests where da/dN, change in crack length versus change in cycles, is measured as a function of ΔK in a standard test coupon containing a prescribed, pre-existing crack. (See Figure 8.3-1). ΔK is the alternating stress intensity factor, which is a function of both the crack size and loading. It should be noted that fatigue crack growth rate data exhibit an apparent ΔK threshold below which small cracks are not observed to grow. [Ref.: General Fracture Control Requirements for Manned Spacecraft Systems, NASA-STD-5007].

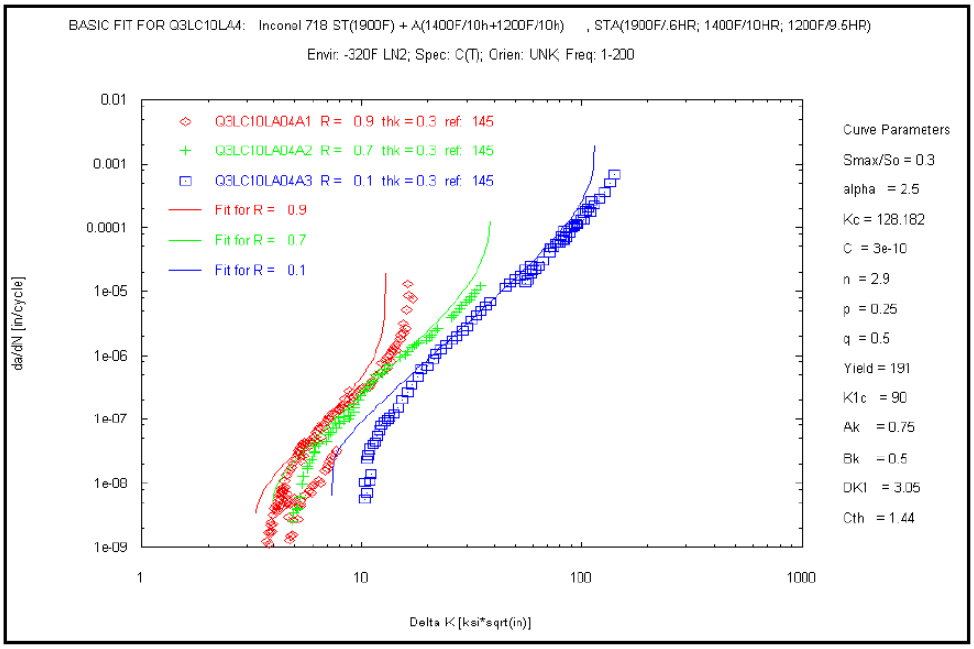

Figure 8.3-1. Crack Growth Rate Data for Inconel 718 (ref.: NASGRO database)

a. The NESC ITA damage tolerance analysis is based on loading spectra for a nominal flight conservatively developed using the BTA hot engine fire test series data. If new loading spectra are developed for the certification cases, the damage tolerance analyses must be updated. **[Findings F-12, F-13, and F-14]**

b. The current NESC ITA results from the conservative, deterministic fracture mechanics analyses for the circumferential crack show a critical crack size of 0.020 inches for a residual fatigue life greater than four for the upstream liner and greater than one for the downstream liners. This result for the downstream liner does not satisfy the requirement of a scatter factor of 4 on the service life factor as required by NASA-STD-5007. **[Findings F-3, F-4, and F-5]**

c. The fracture mechanics results also require an inspection of the flowliners after every flight. Based on the current, conservative fracture mechanics results, the inspection requirement is 0.020 inches. Traditional NDE methods with a 0.020-inch goal and nontraditional methods such as edge replication with a 0.005-inch goal are being evaluated. **[Findings F-1, F-3, F-10, and F-11]**

F-17. (General Finding): Based on the NESC loading spectra for the nominal flight condition generated from the BTA test data, the conservative NESC ITA damage tolerance analysis requires inspection after every flight to detect a critical crack size of 0.020 inches.

Part II. Fatigue Life Approach (to Crack Initiation)

Fatigue may be defined as the cumulative damage incurred in materials caused by cyclic application of stresses and environments resulting in degradation of load carrying capability. The fatigue service life includes all significant loading cycles or events during the period *beginning with manufacture of a component* and ending with completion of its specified use. Unlike the damage tolerance approach, the fatigue life approach does not assume the pre-existence of cracks governed by fracture mechanics. The fatigue life approach addresses the service life to crack initiation, i.e., the service life required to nucleate a crack and grow it to the size that must be addressed by the damage tolerance approach. A stress analysis of the structure is performed to determine the peak stress locations where fatigue cracks initiate. The service life loading spectrum is applied to the peak stress regions of the structure. The fatigue life is determined using fatigue data and a failure rule such as linear cumulative damage. Material property (fatigue) data is determined from laboratory coupons where alternating stress, S, is measured as a function of cycles to failure, N. See Figure 8.3-2. The test failure is defined as a crack of detectable length in a standard test coupon that did not originally contain a prescribed crack but may contain typical manufacturing defects. **In order to use the fatigue life approach for return-to-flight certification of the flowliner, it is essential to assure that the structure has been screened from all significant pre-existing fatigue cracks. Otherwise, the damage tolerance approach must apply.** [Ref.: Structural Design and Test Factors of Safety for Spacecraft Hardware, NASA-STD-5001].

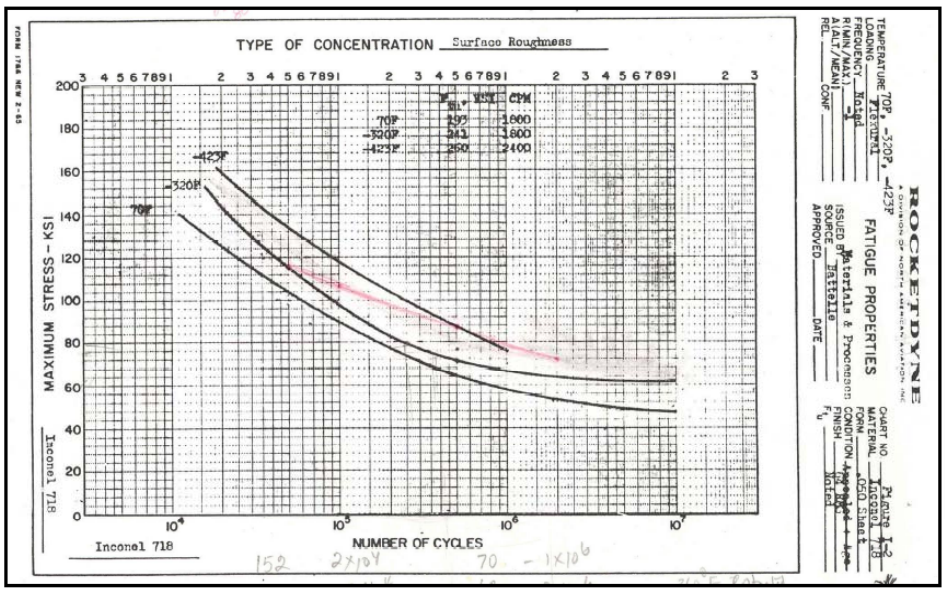

Figure 8.3-2. Fatigue Data for Inconel 718 (Ref.: Rocketdyne)

d. A high fidelity method such as edge replication must be used to inspect the slots to confirm that no manufacturing defects exist that will initiate new cracks. The slots may need additional polishing if the slot surface quality is not acceptable. In addition, the inspection must confirm that no significant fatigue cracks, not detected in 2002, exist that result in a ΔK above the fatigue crack growth threshold where fracture mechanics applies. Even though the edge replication method has been demonstrated in the laboratory to be a high fidelity method capable of detecting cracks to 0.001 inches and below, it may be difficult to find a pre-existing fatigue crack that was polished over in 2002. This is because the polishing procedure may blend material into the opening of the crack thus closing the crack at the slot surface. However, for the two orbiters (OV-104 and OV-105) that returned to flight in 2002, it is highly likely that the flight loads re-opened any existing fatigue crack, which would then be detectable by edge replication. Conventional inspection methods such as the eddy current method must also be used to supplement the edge replication method. Based on previously conducted POD studies, the expected inspection threshold is about 0.020 inches. This discrepancy between the conventional inspection method and the edge replication method is an inspection gap that introduces some degree of uncertainty. The degree of uncertainty is greater for OV-103 which has not returned to flight since the slots were polished in 2002. **[Findings F-1, F-6, F-7, F-8, F-9, F-10, and F-11]**

e. Using the current fatigue loading spectra based on the BTA test data, and using a conservative model for mean stress effects, the NESC ITA fatigue life to crack initiation results for the circumferential crack show a positive margin on fatigue life. However, the fatigue life is 4 missions for the upstream flowliner and 8 missions for the downstream flowliner. If new loading spectra are developed for the certification cases, the fatigue life analyses must be updated. **[Findings F-12, F-13, and F-14]**

f. A fatigue scatter factor of 4 or greater does not provide a fatigue life (safe life limit) sufficient to cover the remaining anticipated operational life of each orbiter. (NASA-STD-5001 specifies a *minimum* service life factor of 4. However, a scatter factor of 10 is typical for high cycle fatigue data). **[Finding F-6]**

g. Surface enhancement treatments offer a potential method to extend the safe life limit of the flowliners to beyond the anticipated operational life of the orbiters. The NESC ITA is assessing the LPB method as a practical surface enhancement treatment that may be effective in delaying crack initiation and retarding crack growth. The results from laboratory tests suggest a benefit in life of an order of magnitude or greater may be achieved by this method.

F-18. (General Finding): Based on the NESC loading spectra generated from the BTA test data, the conservative NESC ITA fatigue life analysis shows a positive margin of safety for one flight, but is not sufficient to cover the remaining anticipated operational life of each orbiter.

Part III. Risk Assessment

PRA is a comprehensive, structured, and logical analysis method aimed at identifying and assessing risks in complex technological systems for the purpose of cost-effectively improving their safety and performance. NASA has adopted Bayesian statistics as the basis for quantitatively assessing risk and uses QRAS or Saphire software codes to perform the analysis. A PRA model for all currently identified flowliner/SSME failure modes of the Orbiter propulsion system has been developed. These failure modes include FOD generated by the flowliner and flowliner structural failure. Both nominal and off-nominal SSME operations will be considered. The event sequence diagram is shown in Figure 8.3-3. [Ref.: Probabilistic Risk Assessment Procedures Guide for NASA Managers and Practitioners, Version 1.1, prepared for the Office of Safety and Mission Assurance, NASA Headquarters, Washington, D.C., M. Stamatelatos, G. Apostolakis, H. Dezfuli, C. Everline, S. Guarro, A. Mosleh, T. Paulos, R. Youngblood, August 2002].

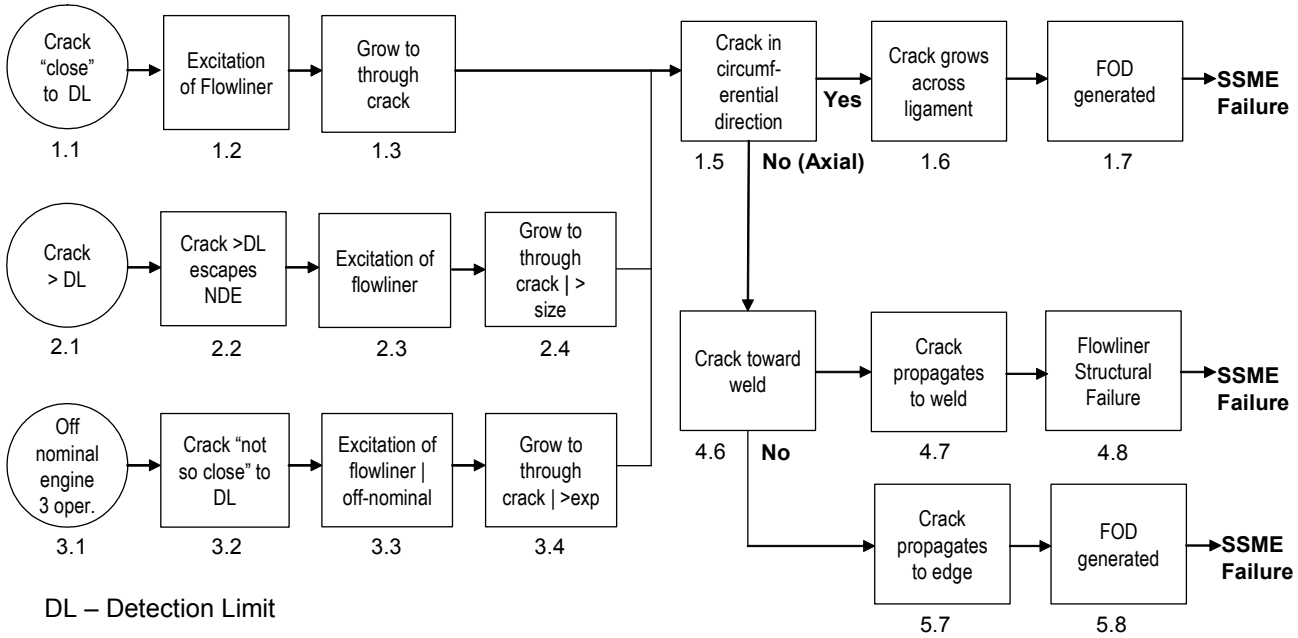

Figure 8.3-3. Event Sequence Diagram for the Flowliner PRA

h. The PRA shows that the risk of flowliner failure is much lower than the current risk of SSME failure. Or stated differently, the risk of a flowliner failure does not increase the risk of an SSME failure by a meaningful amount. If new loading spectra are developed for the certification cases, the PRA must be updated. **[Finding F-2]**

9.0 CONCLUSIONS AND RECOMMENDATIONS

Conclusions:

The conclusions stated below are based on the five General Findings previously reported in Chapter 8. It is essential to note that these findings are based on the independent analyses conducted by the NESC for only the nominal flight condition. The development of the flight rationale must be based on a complete assessment of the program-sanctioned loading spectra for all nominal and off-nominal flight conditions for which the orbiter must be certified before returning to flight.

1. Based on the past flight history and the root causes investigation, the actions taken in 2002 to repair the LH_2 gimbal joint flowliners render the Orbiter safe to fly. This is provided the flowliners are inspected before the next flight to ensure that all surface flaws were removed by polishing and all fatigue cracks were repaired. In addition, an assessment of the certification loading spectra for the nominal and off-nominal flight conditions will be necessary to determine the post-flight inspection requirements.

2. Based on a probabilistic risk assessment, the risk of SSME damage due to cracks in the flowliner is an insignificant contributor to the overall SSME catastrophic risk, assuming inspection after every flight.

3. The similitude between the BTA/GTA ground tests environment and the Orbiter flight environment could not be established. Therefore, there are uncertainties in the fatigue loading spectra developed from the BTA/GTA test data. Unverified scale factors have been applied to the loads in the fatigue loading spectra in an attempt to account for these uncertainties. Because of these uncertainties, there will be risks associated with any loading spectrum used to develop the flight rationale derived from the BTA/GTA experiment. These concerns notwithstanding, we have concluded that the ground test data can be a suitable database to establish the certification spectra provided conservative scale factors based on appropriate engineering judgment are used to account for the uncertainties.

4. Based on the NESC loading spectra for nominal flight conditions generated from the BTA/GTA test data, the conservative NESC ITA damage tolerance analysis for the circumferential crack locations requires inspection after every flight to detect a critical crack size of 0.020 inches and repair of any cracks found during the inspection. Since these results were not generated for the official certification spectra, post-flight inspection

requirements must be determined from an assessment of the certification loading spectra for the nominal and off-nominal flight conditions.

5. Based on the NESC loading spectra for nominal flight conditions generated from the BTA/GTA test data, the conservative NESC ITA fatigue life analysis shows a positive margin of safety for one flight, but is not sufficient to cover the remaining anticipated operational life of each orbiter.

Based on the five General Findings stated above, the NESC ITA has concluded that the Orbiters are safe to return to flight provided the specific recommendations listed below are implemented:

Recommendations:

1. Establish the surface quality of the slots by using a high fidelity inspection method such as edge replication. Assess the effectiveness of the original polishing done in 2002 to determine if all manufacturing defects have been removed. Re-polish the slots as required to remove all significant surface defects. Also, repair any fatigue cracks found during this inspection.

2. Perform a damage tolerance analysis for all certification conditions to establish the critical crack size, the required inspection method to detect the critical crack size, and the required inspection interval.

3. Conduct a POD study and develop the inspection procedure that must be used to meet the requirements of the damage tolerance analysis.

4. Change the orbiter operational procedures to implement the inspection requirements established by Recommendation 2.

5. Perform a fatigue analysis for all certification conditions to estimate the fatigue life to crack initiation. This establishes the safe life limit on the flowliners. These results may be used in lieu of the damage tolerance approach (Recommendation 2) provided the results satisfy the requirements of NASA Standard 5001 and the NASA Fracture Control Board grants a waiver of the NASA Standard 5007.

10.0 LESSONS LEARNED

LESSON LEARNED 1: Formal, archival documentation of the original investigation and the subsequent tests and analyses conducted to resolve the problem were substantially incomplete. The discipline of preparing and peer reviewing formal engineering reports leads to a high degree of accuracy and technical rigor.

It has been two years since the cracks were originally discovered in the flowliners at the gimbal joint of the LH_2 feedlines. In that time, numerous important observations, analyses, and tests have been accomplished. The ITA Team found extensive documentation archived on a web site (SSPWEB) maintained by the Program Office. However, the preponderance of documentation is in the form of briefing charts prepared for oral presentations. Also, the team found extensive technical information available from individual engineers working on the problem resolution team. Unfortunately, much of this information was not properly documented in formal engineering reports. Also, there is no evidence that critical findings were formally peer reviewed. While numerous examples of incomplete documentation could be sited, two specific examples are discussed below to illustrate the potential implications of the lack of technical rigor that might occur when formal documentation is not required and the results are not independently verified through peer review.

The location, orientation, and length of cracks originally found in the fleet in 2002 could not be determined from the original documentation given to the ITA Team. In fact, the numerous problem summary briefings given by engineers and senior team leaders, dating from August 2002 to January 2004, contained conflicting data on both the number of cracks found in each orbiter and the length of these cracks. To resolve these discrepancies, an extensive effort was required to re-analyze the original inspection data obtained in 2002. During this effort to establish accurate crack information, it was discovered that several cracks were kinked rather than extending in a self-similar crack growth direction as was implied by the sketches and analyses reported in the briefing charts. This is a significant finding because kinked cracks like those found in the orbiters, typically exhibit bifurcation behavior and change crack growth direction due to complexities in the global stress field. This is critical information in determining the root causes of the cracks observed in the fleet. In fact, incorrect conclusions regarding the problem resolution could have resulted from this omission of critical evidence.

As part of the investigation, two engine hot fire test series were conducted at Stennis Space Center. The purpose of these tests was to better understand the feedline flow physics and the associated forcing functions, which define the spectrum loadings on the flowliner. The first test series used a BTA with a fixed joint and without a flexible bellow. The second test series used a GTA with a gimbaled joint and flexible bellow. Not only did NASA invest considerable resources to conduct these tests, the interpretation of the test results has led to an escalation in

concern over the structural integrity of the flowliners and an additional expenditure of tens of millions of dollars in an attempt to develop a new flight rationale. Yet, there is no formal test report that documents the calibration of instrumentation, test procedures, sequence of test events, test data acquisition, and post-test data reduction. Furthermore, there is no formal documentation of the engineering details regarding how the data was used to develop a loading spectrum and the associated prediction of the residual fatigue lives of the flowliners.

Recommendation 1: Require formal reports to be generated for orbiter hardware inspections and for the results of testing.

Recommendation 2: Institute a system whereby all documentation associated with the SSP be available in a single location. This information should include, but not be limited to, all plans and drawings, all qualification test plans and results, all flight data, and all subsequent testing plans and results.

LESSON LEARNED 2: Ground testing should be conducted in as close to flight configuration as possible. Where differences between ground and flight configurations or environments are necessary, every effort to correlate the ground test data to actual flight situations must be made. One of the most difficult obstacles to overcome in the flowliner investigation has been the disparity of the propellant feed systems between the ground-based test facility and the flight vehicle.

NASA does not have a Flight-Configured Main Propulsion System (MPS) Ground Test Facility that accurately simulates the flight environment. Differences between the ground-based test facility and the flight vehicle can singularly and collectively degrade the fidelity of ground-based hot fire tests in characterizing the flight environment. Examples encountered during the course of this investigation include the following:

- Differences in the feedline weld bead in feedline between flowliners and SSME interface;
- Differences in thermal insulation (i.e., vacuum jacket vs. BX-250 SOFI) on the feedlines;
- Differences in feedline layout (i.e., line lengths, bends, flex joints, valves, flow meters); and
- Differences in sensors and sensor locations.

The inability to accurately replicate the flight conditions of the MPS in a ground test has been a persistent difficulty in determining the fundamental root cause of the flowliner issue. Significant resources and schedule time have been expended to overcome the need for a test facility that replicates the collective environment (e.g., flow, structural, dynamic, thermal, etc.) of the actual flight vehicle. A facility dedicated to subjecting the engine and supporting feed system to a

high-fidelity flight environment could be used for acceptance tests, green run tests, and fleet leader extension tests.

The MPTA was useful in certifying the MPS for the shuttle, but was retired early in the program. It would not be necessary to configure the system to accommodate all the engines used in the MPS, but to replicate the fluid environment that one engine would be exposed to, with the flexibility of expanding the resolution of the system environment to include as many engines as needed. With regard to the MPS environment of subsequent vehicle programs, the instrumentation suite incorporated into the ground facility could be integrated into the propellant system without significant affect to the characterization of the system environment.

11.0 DEFINITION OF TERMS AND ACRONYMS

Definition of Terms

Finding
A conclusion based on facts established during the assessment/inspection by the investigating authority.

Lessons Learned
Knowledge or understanding gained by experience. The experience may be positive, as in a successful test or mission, or negative, as in a mishap or failure. A lesson must be significant in that it has real or assumed impact on operations; valid in that it is factually and technically correct; and applicable in that it identifies a specific design, process, or decision that reduces or limits the potential for failures and mishaps, or reinforces a positive result.

Observation
A factor, event, or circumstance identified during the assessment/inspection that did not contribute to the problem, but if left uncorrected has the potential to cause a mishap, injury, or increase the severity should a mishap occur.

Problem
The subject of the independent technical assessment/inspection.

Recommendation
An action developed by the assessment/inspection team to correct the cause or a deficiency identified during the investigation.

Root Cause
Along a chain of events leading to a mishap or close call, the first causal action or failure to act that could have been controlled systemically either by policy/practice/procedure or individual adherence to policy/practice/procedure.

Acronyms

BSTRA	Ball Strut Tie Rod Assembly
BTA	Battleship Test Article
CC	Corner Crack
CFD	Computational Fluid Dynamics
DOF	Degree of Freedom
DS	Downstream
ESD	Event Sequence Diagram
ET	External Tank
FCG	Fatigue Crack Growth
FEM	Finite Element Model
FFA	Forward Fracture Analysis
FPL	Flight Power Level
FOD	Foreign Object Debris
GSFC	Goddard Space Flight Center
GTA	Gimbal Test Article
ID	Inner Diameter
ITA	Independent Technical Assessment
JSC	Johnson Space Center
K	Heat Transfer Coef. (btu/hr-ft-^{o}R)
L	Length (ft)
LDR	Linear Damage Rule
LH_2	Liquid Hydrogen
LHe	Liquid Helium
LO_2	Liquid Oxygen
LPB	Low Plasticity Burnishing
LPFP	Low Pressure Fuel Turbopump
MLP	Multi-Level Parallelizm
MPS	Main Propulsion System
MPTA	Main Propulsion Test Article
MSFC	Marshall Space Flight Center
N	Pump Rotation Rate (rev./min.)
NDE	Nondestructive Evaluation
NESC	NASA Engineering and Safety Center
NPSP	Net Positive Suction Pressure (psi)
NRB	NESC Review Board
OD	Outer Diameter
OP	Orbiter Program
OV	Orbiter Vehicle
P_o	Total pressure

POD	Probability of Detection
P_{oi}	Total Pressure at the Pump Inlet (psi)
PRA	Probabilistic Risk Assessment
P_{vi}	Hydrogen Vapor Pressure (psi)
q	Heat Transfer (btu/hr.)
Q	Pump Flow Rate (gal./min.)
r_i	Inner Radius (ft)
r_o	Outer Radius (ft)
RPL	Relative Power Level
S&MA	Safety & Mission Assurance
SG	Strain Gage
SOFI	Spray On Foam Insulation
SPRT	Super Problem Resolution Team
SSME	Space Shuttle Main Engine
TC	Through Crack
TR	Transfer Ratio
T_i	Temperature at Inner Radius (^oR)
TIM	Technical Interchange Meeting
T_o	Temperature at Outer Radius (^oR)
UP	Upstream
V	Velocity (ft/s)
ρ	Density (lbm/ft^3)

Volume II: Appendices

A. ITA/I Request Form (NESC-PR-003-FM-01
B. Original NESC Flowliner ITA Plan
C. Reference Materials
   C.1 LO_2 Type II Engine 1 Feedline Qualification and Test History
   C.2 MPS Flowliner Replication Team Status Report
   C.3 Investigation of Shuttle MPTA LH_2 Flowliner Crack. Huntington Beach/Seal Beach Site Host Engineering Function Material & Process Engineering Laboratory Report; Lab Report No. M&PE-2-1327
   C.4 Original LO_2 Qualification Test Report Summary: Crack Summary. Document Number MPS-QTR-13542-302. Appelman, H., 1979
   C.5 Compilation of the Crack Inspection Data
D. Engineering Reports of Tests and Analyses
   D.1 The Loading Environment (As described By Flow Physics)
   D.2 Development Of The Fatigue Loading Spectrum
   D.3 Damage Tolerance (Fracture Mechanics) Analysis Methods And Results
   D.4 Fatigue Life To Crack Initiation Analysis Methods And Results
   D.5 Examination and Inspection Methods
   D.6 Crack Initiation and Surface Enhancement
E. Tasks and Schedule for Phase II
F. Contractors
G. Core Team Bios

Document Approval and Revision History

Approved:	Original signature on file	7/28/04
	NESC Director	Date

Version	Description of Revision	Office of Primary Responsibility	Effective Date
1.0	Final Report	C.E. Harris	07/20/04